POLITECNICO DI TORINO

Master's Degree in Energy and Nuclear Engineering

INSTITUT POLYTECHNIQUE DE GRENOBLE

Master's Degree in Reactor Physics and Nuclear Engineering Specialty

Master's Degree Thesis

Atomistic simulations of fission gas bubbles in nuclear fuels

Supervisors

Dr. Johann BOUCHET

Prof. Monica FERRARIS

Prof. Alexis NUTTIN

Candidate

Matteo CANDUCCI

February 2023 - August 2023

CEA Cadarache 13108 St Paul lez Durance Cedex

Atomistic simulation of fission gas bubbles in nuclear fuels

Abstract in English

This master thesis investigates the role of nano-bubbles porosity on some of the main thermo-physical properties of the (U,Pu)O_2 nuclear fuel using atomistic simulations. In the last years the role of mixed oxides fuels became increasingly relevant for current and fourth generation reactors, and better understanding the properties of the compound is crucial, especially the consequences of its irradiation. The goal of this work is thus to calculate, using molecular dynamics simulations, the specific heat, the linear thermal expansion coefficient, the elastic coefficients and the thermal conductivity of porous (U,Pu)O_2, covering a wide range of plutonium contents, temperatures and bubbles characteristics. The effect of the nano-bubbles is presented for every simulation and a general law is proposed for each property by fitting the results obtained. The newly proposed laws are suitable to be implemented in the fuel performance codes, which study the materials' behaviour at a larger scale.

Simulazioni atomistiche di bolle di gas di fissione in combustibili nucleari

Abstract in lingua italiana

Questa tesi di laurea indaga il ruolo della porosità delle nanobolle su alcune delle principali proprietà termofisiche del combustibile nucleare (U,Pu)O_2, utilizzando simulazioni atomistiche. Negli ultimi anni il ruolo dei combustibili a ossidi misti è diventato sempre più rilevante per i reattori attuali e di quarta generazione, e una migliore comprensione delle proprietà del composto è fondamentale, in particolare le conseguenze della sua irradiazione. L'obiettivo di questo lavoro è quindi quello di calcolare, utilizzando simulazioni di dinamica molecolare, il calore specifico, il coefficiente di dilatazione termica lineare, i coefficienti elastici e la conducibilità termica di (U,Pu)O_2 con pori, coprendo un'ampia gamma di contenuti di plutonio, temperature e caratteristiche delle bolle. L'effetto delle nanobolle viene presentato per ogni simulazione e viene proposta una legge generale per ogni proprietà adattando i risultati ottenuti. Le nuove leggi proposte sono idonee ad essere implementate nei fuel performance codes, che studiano il comportamento dei materiali su scala più ampia.

Contents

List of Tables

List of Figures

Chapter 1

Introduction

1.1 A wider prospective

This work aligns with the wider context of climate change, the world's energy crisis and the path to a more sustainable world.
One of the most urgent global concerns of our day is climate change, which is almost entirely caused by human activities. Its repercussions are being felt globally, from escalating temperatures and severe weather to melting glaciers and increasing sea levels and again from the disruption of ecosystems and biodiversity loss to agriculture and food endangerment, water scarcity and climate-related migrations. To mitigate this ongoing process and avoid its irreversibility on our world for future generations, climate change requires swift and coordinated actions. We can work to create a more resilient, egalitarian, and sustainable world by acknowledging the gravity of this issue, applying sustainability practices, switching to clean energy, and encouraging international cooperation. Every person, community, and country has a responsibility to address the urgency of climate change, and the time to act is now.
In 2020 around 75% of the greenhouse gases were generated for energy production, of which 43% were due to electricity and heat production and 21% to transportation [1]. The good news is that most of this sector might be the easiest to convert into one that is carbon neutral, the technological advancement of low emission power production sources, such as renewable and nuclear plants, has never been so rapid, and the same thing can be said for the energy industries indispensable for a better energy management, such as the electrical mobility, the hydrogen supply chains, the bio-fuels and the stocking capacity.
It is generally accepted that nuclear power plays a significant role in a secure global pathway to net zero [2], doubling its energy production from 413 GW in early 2022 to 812 GW in 2050 in the net zero emission (NZE) scenario. The lack of nuclear

energy production in the pathway to NZE would cost USD 500 billion of additional investments.

1.2 Thesis's objectives and structure

Fuel performance codes are used to simulate the performance of the nuclear fuel by solving the equations for the heat transfer, the evolution of the produced isotopes, the behaviour of the main fission products in the fuel rod and the stresses and strains in the fuel and the cladding. With the increasing computational power availability in the research field during the last few years, the fuel performance codes gained more and more importance, and are now a key part of the process for the study and design of nuclear fuels.
This thesis focuses on the study of the effect of nano-porosities and fission gas nano-bubbles on some of the key properties of the mixed oxide (MOX) nuclear fuels, in order to deepen the understanding of the fuel and to propose new porosity-dependent laws to be implemented in the fuel performance codes. The properties studied are the specific heat, the linear thermal expansion coefficient, the elastic coefficients and the thermal conductivity. The thesis aims at expand and aid the work carried out by Giulia Porto in her Ph.D., her work is focused on the study of defects present in MOX fuels and their effect on the macroscopic thermophysical properties in hypo-stoichiometric conditions by using atomistic simulations. Beside the work of Giulia Porto, the results produced by Théo Beigbeder during his Ph.D. work have been the foundation for all the advancements currently presented. Both Giulia Porto and Théo Beigbeder worked for their Ph.D. in the same laboratory in which this document was produced.
The document starts detailing the methods, algorithms and assumptions that were used. By carefully applying the same methods anyone can verify the outcomes and obtain the same results. These concepts are present in the second and third chapters.
In the fourth chapter all the major results are presented, including the desired properties and the lattice parameters. In the same chapter, side by side with the results, it is present their discussion, to expand on their implication and interpretation.
In the fifth chapter a general conclusion of the work is done, together with a few suggestions for future works that aim at expanding these results.
The major tools used in this work are:

1. Large-scale Atomic/Molecular Massively Parallel Simulator (LAMMPS) [3], a molecular dynamics (MD) classical simulation code developed at Sandia National Laboratories. In this work it was used to carry out all MD simulations.

2. Open Visualisation Tool (OVITO) [4], a graphical inspection tool originally

born as a research project at the Materials Science Department of Technische Universität Darmstadt in Germany. In this work it was used to inspect the structures and their evolution during the simulations.

3. Python, Bash and other programming languages were used to manage the data, study it and post process it. They were also integrated with the LAMMPS simulation code to increase its efficiency.

4. Access to Irene (ex Joliot–Curie), a high performance computer (HPC) hosted by the Centre de Calcul Recherche et Technologie (CCRT), one of CEA supercomputers centers, situated at Bruyères-le-Châtel in Essonne, France.

1.3 The role of CEA Cadarache in this work

The Commissariat à l'énergie atomique et aux énergies alternatives (CEA) is a French research organisation which focuses on the innovation and development in the fields of low carbon energy, digital and medical technology, defense and national security.
The CEA center in Cadarache is the biggest research center ever built for the study of low carbon energy production in Europe. CEA Cadarache is located in Provence-Alpes-Côte d'Azur, close to the village Saint-Paul-lès-Durance. The Institut de REcherche sur les Systèmes Nucléaires pour la production d'Energie bas carbone (IRESNE) is the CEA institute located in Cadarache.
IRESNE is divided in three departments, each focused on different aspects of the nuclear and renewable energies development: the Département d'études des réacteurs (DER), the Département de technologie nucléaire (DTN) and the Département d'études des combustibles (DEC). In the DEC three services focus on different aspects of the study of the nuclear fuel, in particular the Service d'études et de simulation du comportement des combustibles (SESC) uses a modelling approach for the study of the fuel, and it is divided in turn in several laboratories. It is in this context that this work is written, in particular in the Laboratoire de modélisation du comportement des combustibles (LM2C), which approaches the simulations of the fuel from an atomistic level in order to develop ever so precise models for the more common materials used in the nuclear industry.

Chapter 2

Theoretical background

2.1 Nuclear fuels

2.1.1 Contextualization of the nuclear fuels

Nuclear fuels are the materials used for the production of energy via nuclear fission plants. There exists a wide range of nuclear fuels, from metals to oxides and from liquids to carbides, but the most common one in modern reactors used for energy production is the uranium dioxide.
The uranium dioxide, also referred to as UO_2, or urania, is a ceramic fuel commonly used in light water reactors (LWRs) and heavy water reactors (HWRs). The fissile isotope used to sustain the reaction with low energy neutrons is ^{235}U, its natural concentration in uranium deposits is about 0.7%, with the rest composed by the largest part of ^{238}U, which is only fissile in a fast neutron spectrum but it is fertile for thermal neutrons. Further details are given in section (2.3).
In modern thermal reactors the amount of ^{235}U needed to sustain the reaction ranges from 3.5% and 4.5%, with the important exception of the high-power channel-type (RBMK), the Uranium Naturel Graphite Gaz (UNGG) and the Canada Deuterium Uranium (CANDU) reactors, which can operate with a natural uranium concentration. A process to enrich the uranium is thus used for the remaining types of reactors, usually either via gaseous diffusion or gas centrifugation.
In the french fleet the plutonium is also used together with uranium, in MOX fuels, whose chemical formula is $(U_{1-y},Pu_y)O_2$, where the subscript y refers to the plutonium enrichment and thus ranges from zero to one. The concentration of plutonium usually ranges from 1.5% to 30% and it is chosen based on the type of reactor and its design.
Since MOX fuels are oxides, their thermal conductivity is low compared to other materials, especially metals. This is a major drawback for their use, as the capability of the fuel to transfer the heat produced to the coolant is one of the most important

factors considered when a fuel is chosen to be used in a reactor. The MOX fuels are also brittle, and tend to crack after severe power ramps or due to thermal gradients inside the rod. Nevertheless, MOX fuels also have some important positive aspects, such as the high melting point and yield stress, the capability to sustain high burn-up conditions and to trap the fission products efficiently.
A few alternatives to urania and MOX fuels will be used in the future in generation IV reactors, *e.g.*, molten salts, but for the most part these types of fuel will remain in the operating reactors for a considerable time, especially considering that MOX fuels can be adapted to be used in fast neutron reactors (FNRs), which will be important for the closure of the fuel cycle. For this reason the use of MOX fuels is destined to increase in the future.

2.1.2 The Bredig transition

Many experimental studies have been carried out on urania samples in the last decades [5, 6, 7], but only a few of them were conducted at high temperatures [8, 9, 10, 11, 12]. Some of these works [13] have reported a peak in the heat capacity around $T_B \sim 0.8T_m$, where T_m is the melting point and T_B is the so called Bredig temperature. The peak is associated to the Bredig transition [14], sometimes also called Faraday transition or Λ-transition, and it is observed for many ionic materials.
The reason behind the Bredig transition is sometimes explained by an increase in lattice and electronic defects, and in particular by Frenkel pairs [9, 15]. An other guess is attributed to the pre-melting of the anions sub-lattice [16, 17, 18, 19, 20]. The latter interpretation seems to be gaining more support in the last few years and it is supposed to be the best explanation despite the lack of a definitive experimental confirmation.
In the case of PuO_2, the Bredig temperature is supposed to be inferior to UO_2, due to the lower melting point. This is observed in atomistic studies, but due to the extreme difficulty of performing experiments with plutonium at high temperatures the experimental data is again meager.

2.1.3 Fuel degradation

During any reactor's operation the fuel goes through drastic changes, both at the microscopic and at the macroscopic level, due to the change in the structure and to the creation of a variety of new defects in the lattice. The neutron irradiation, the decay of irradiated atoms and the formation of fission products, form a variety of new imperfections in the micro-structure, such as point defects, dislocations, change in the grain size and fission gas bubbles. The high temperatures of the typical reactors decrease the quantity of most of these defects by recombination,

but the structural change remains drastic.
When neutrons impact atoms inside the fuel they cause a cascade of defects, as their momentum is transferred in part to the quasi-still atom in the lattice. This event can also be called collision cascade or displacement cascade and it happens only if the incident neutron exceeds a threshold energy dependent on the lattice. For UO_2 this threshold is around 40 eV [21]. A typical graphical representation of a displacement cascade is shown in figure (2.1).
The first atom to interact with the higher energy neutron is called primary knock-on atom (PKA). It causes most of the damage, by initializing the cascade and displacing other atoms until all its momentum is absorbed by the lattice. During this process a certain number of new self-interstitials and vacancies are formed, and only part of them disappear when the cascade is over, the rest remain in the fuel either as simple point defects or by clustering and forming dislocation loops, voids and even more complex types of defects.
Collision cascades are a continuous phenomenon inside the fuel and the surrounding materials, like the zirconium cladding in pressurized water reactors (PWRs). Since the damage inflected by the neutrons depends on many factors, such as the type of material studied, the energy spectrum of the neutrons, the type of reactor, and so on, an independent unit of measure was proposed in order to compare different damages caused by neutrons. This unit is the displacement per atom (dpa), which is defined as the number of atoms permanently displaced in a certain time period divided by the total number of atoms present in the sample studied. At the same temperature, a higher dpa is associated with higher swelling and embrittlement, thus causing irreversible macro-structural changes.

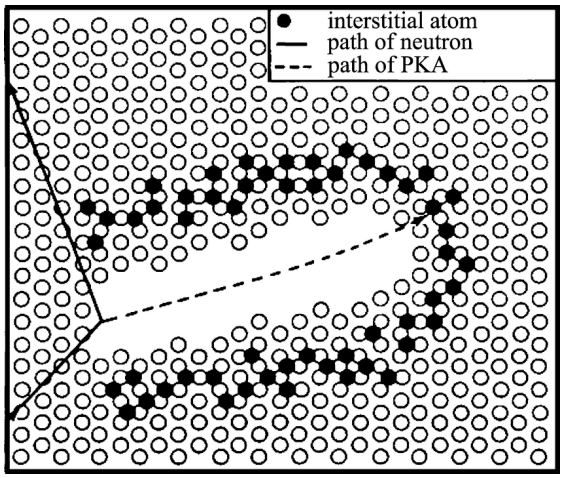

Figure 2.1: Graphical representation of a displacement cascade. [22]

Since this changes in the micro-structure cause an evolution of the macroscopic

properties of the pellets it is progressively important to know the laws that govern these properties for the irradiated fuel, to meet increasingly higher safety standards and to improve the overall performance of the reactors.
Unfortunately, due to its very high radio-toxicity, it is still very complicated to carry out experiments with spent MOX fuel that will give results with low uncertainties, especially at high temperatures. For this reason, a growing portions of the laws describing the evolution of the materials' properties that are now used in fuel performance codes are derived from atomistic simulations rather than relying solely on experimental data.

2.1.4 The presence of bubbles

Assessing the dominant concentration of fission product isotopes within irradiated fuel can be challenging due to various influencing factors. These factors include the region of the pellet investigated, the post-irradiation time elapsed, the energy spectrum of the neutrons, the irradiation temperature, and more. However, it is widely acknowledged that xenon is the predominant element produced by fission [23, 24]. Coincidentally, xenon might also be one of the most impactful elements in certain aspects, such as thermal conductivity and structural behavior. Since it is a noble gas, it is insoluble in the lattice and it is very difficult to move unless a high number of Schottky defects (SDs) is present [25, 26]. The behaviour and migration of xenon from its creation site to the cladding gap is a complex phenomenon. However, it has long been recognized that the atoms are trapped inside bigger and bigger voids, due to the diffusion of vacancies, forming bubbles with very different sizes, ranging from a few nanometers to several micrometers [27].
Other fission gases, like krypton, can also be present inside the bubbles, but their concentration is so low that they are often disregarded as with little or no importance in the context of atomistic simulations of nuclear fuels. Furthermore, these isotopes are noble gases just like xenon, which means their chemical and physical behaviour is quite similar to one another in any case. The gases generated by the fission events are generically referred to as fission gas products (FGPs).
The table (2.1) reports the most common fission gas isotopes produced in the environment of a nuclear fuel, the percentages are reported over the whole fission yield spectrum of the fissile material. In the image (2.2) it is reported the mass yield percentage for each isotope grouped by mass number.

2.1.5 The need of new correlations to describe the bubbles

The aim of this thesis is to investigate some of the properties of the MOX fuels including the effects caused by the presence of fission gas bubbles, to understand

Product	Thermal fission yield (at%)	Fast fission yield (at%)
$^{130}_{54}$Xe	0.000038 ± 0.0000098	0.000152 ± 0.000055
$^{131m}_{54}$Xe	0.0313 ± 0.003	0.0365 ± 0.0031
$^{133}_{54}$Xe	6.6 ± 0.11	6.61 ± 0.13
$^{133m}_{54}$Xe	0.189 ± 0.015	0.19 ± 0.015
$^{135}_{54}$Xe	6.61 ± 0.22	6.32 ± 0.18
$^{135m}_{54}$Xe	1.22 ± 0.12	1.23 ± 0.13
Totality of Xe	14.65 ± 0.468	14.39 ± 0.458
$^{82}_{36}$Kr	0.000285 ± 0.000076	0.00044 ± 0.00016
$^{85}_{36}$Kr	0.286 ± 0.021	0.286 ± 0.026
$^{85m}_{36}$Kr	1.303 ± 0.012	1.307 ± 0.043
Totality of Kr	1.589 ± 0.033	1.593 ± 0.069

Table 2.1: Fission gases yield production for $^{235}_{92}$U, at high and low energy spectrum. [23]

how they change with respect to the same properties in the bulk. In particular, as previously stated, the properties that will be addressed are the specific heat capacity at constant pressure (c_p), the linear thermal expansion coefficient (LTEC), the elastic coefficients (C_{ij}) and the thermal conductivity (k). The results obtained are fitted through new or old laws to account for the porosity in the physical properties.
Since an experimental approach to this problem is very complicated, in this thesis the results are the product of atomistic simulations, in particular using the MD method. Even though all the results reported are compared with experimental measures and previous ab-initio and MD simulations, new data to confront the results is always desirable, either with experiments, ab-initio simulations or at least with different MD potentials.

2.2 Bubble characteristics

2.2.1 Introduction to bubble characteristics

Since the effects of the FGPs are so drastic on the performance of the MOX fuels, a substantial amount of studies has been conducted during the last decades. This research has employed both experimental and simulation approaches to

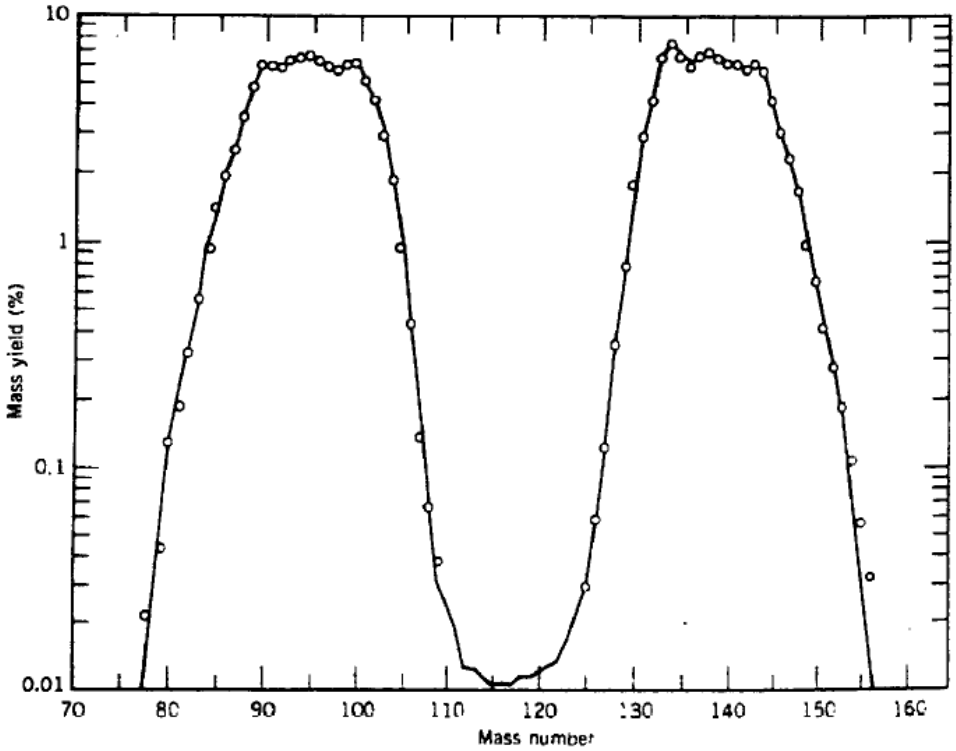

Figure 2.2: Fission products mass yield per mass number, for UO_2 fuels. [28]

investigate how the presence of these fission gas products alters the nuclear fuel's physics. Simulating xenon bubbles encompasses various critical factors, including the distribution of xenon bubble concentrations throughout the bulk material and single grains, as well as considerations about bubble shape, size, average spacing, xenon pressure within the bubbles, and the resulting effects.

2.2.2 The three steps of fission gas release

In their study, Tonks *et al.* [27], present a good overview of the main macro-phenomenon regarding the fission gases, from their creation to their release into the plenum. The process can be schematically split into three steps:

1. Formation of nano-bubbles of xenon and krypton from the fissionable atoms and from the beta decays of the unstable products.

2. Growth of the nano-bubbles and their diffusion toward the grain boundaries.

3. Formation of macro-bubbles which, if big enough, act as open porosities all along the grain boundaries from the inside of the pellet toward the plenum,

with a consequent fission gas release (FGR).

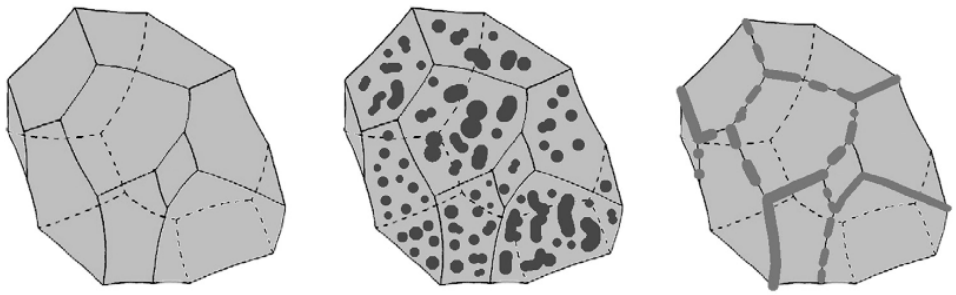

Figure 2.3: The three steps of the FGR phenomenon from the point of view of a single grain. From left to right: formation of nano-bubbles, transport toward the grain boundaries, formation of open porosities that lead to the release of the gases outside the pellet. [27]

The initial nano-bubbles start as single point defects, that in the case of MOX fuels are single gas atoms occupying a SD. But their diffusion inside the grain leads them to interact with each other and segregate into bigger intra-granular bubbles. The growth of nano-bubbles is a complex phenomenon which involves an energy barrier, beyond which spontaneous bubble growth occurs.
Since the bubbles possess some degree of natural mobility, even if very feeble, they diffuse in the lattice until they reach an energy well, which might be any kind of defect in the crystal, like dislocations, precipitated fission products, or even the external surfaces of the pellet. The most stable and common place where they might stop their motion is a grain boundary. Once the bubbles reach the grain boundaries they are no longer called intra-granular and become instead inter-granular.
When the bubbles become inter-granular they start to grow, since other gases form during irradiation and are guided by the same phenomenon. The growth of the bubbles follows the least energetically expensive path, which is the nearby portion of the grain boundary. For this reason the bubbles remain inter-granular. Once the bubbles are big enough they connect forming open porosities.
If the burn-up is high enough, and the thermodynamic conditions favourable, the bubbles become big enough to connect the open porosities to the outer surface of the pellet and release the gases in the plenum. This phenomenon is greatly accelerated by accidental conditions which cause power ramps and a temperature increase. A phenomenon that highly accelerates the fission gases release is the pellet cladding interaction (PCI), which happens when the fuel pellet and the zirconia (ZrO_2) cladding interact. This event is dangerous, as it compromises the integrity of the cladding, which may fracture and release gases from the plenum into the coolant. This scenario bypasses a crucial physical barrier that otherwise

separates toxic elements within the fuel from external environment, such as the fuel itself, the cladding, the primary circuit and the containment building.
The fission gas release into the plenum is not necessarily a bad thing for the reactor operation, the presence of gases in the pellet degrades the thermomechanical properties of the fuel, including the thermal conductivity, the thermal expansion and the yield stress. On the other hand the presence of gases in the plenum degrades the efficiency of the heat exchange between the fuel and the coolant, and the fission gases are no longer trapped inside the fuel but they can move freely inside the plenum, one step closer to the release into the coolant.
The design of different reactors is thus a trade-off between these two effects, thermal reactors are typically designed to have a smaller FGR rate than fast reactors, which means that each rod needs to have a bigger plenum in the latter to accommodate the fission products.

2.2.3 Distribution of the bubbles in the fuel

The distribution of bubbles inside the fuel depends on several factors, most importantly the temperature and the burn-up. In thermal reactors, in normal operating conditions, the burn-up is higher in the outer part of the pellet, since the thermal flux is directed from the water that acts as a moderator for the neutrons toward the fuel. Vertically, the burn-up is at its peak, in a first approximation, near the center of the rod, since the neutron flux resembles a cosine function. It is evident that many other effects change the burn-up distribution from this simple approximation, such as the temperature, the pressure and the many components inside the reactor that influence the thermo-fluid-dynamics and the neutronics aspects of the core's dynamic.
The greater the burn-up, the greater the presence of fission products, and consequently of fission gases. The fact that more FGPs are present in a certain region of the fuel does not necessarily mean that the bubble concentration will be higher there, since the bubbles can merge resulting in a distribution with a lower concentration but a higher average size [27, 29].
Several studies have been carried out in the last decades, and the research is still ongoing, to increase the understanding of these correlations. Many authors [30, 31, 32, 33] published works in which UO_2 spent fuel samples were analyzed with a transmission electron microscope (TEM) and they were able to retrieve some data concerning the bubbles' characteristics. As already mentioned, the comparison of these results would hold little significance, but some general guidelines can be extracted from their results: the most common nano-bubbles' dimensions are in the range between 1 nm and 10 nm in diameter, their density is about $5 \cdot 10^{22}$ bubbles/m^3 and $2 \cdot 10^{24}$ bubbles/m^3, the intra-granular bubbles have a

higher concentration but a smaller average size compared to inter-granular bubbles. Due to the complexity of carrying out experiments on real spent fuel for safety reasons, during the years many more works have been published [34, 35, 36, 37, 38] concerning experiments where xenon was implanted artificially instead of naturally forming as a product of the fissionable elements. Their results closely resembles the experiments on spent fuel, both on the point of view of the bubble size and of their concentration.
Other researches focused on models to characterize the size and the density of bubbles, with close results to experimental data, but often over-quantifying the bubble size, an example is the single knock-on (sko) model proposed by Wood *et al.* [39].
Due to the higher burn-up in the rim region of the pellets, a complete chemical transformation takes place in this region of the lattice. This newly formed structure of the spent fuel is called High Burn-up Structure (HBS). The HBS posses different properties compared to the original structure, and its micro-structure is different too: it posses smaller grains and a much more abundant quantity of fission products. The density of bubbles is naturally higher in the HBS.
The influence of temperature on bubble characterization can be significant. Elevated temperatures augment the kinetic energy of lattice atoms, leading to increased mobility of defects, including bubbles. It is still debated how the diffusion of bubbles works in the detail, but it is clear to the academic community that a greater temperature helps the movement and the interaction between bubbles, which, after overcoming an energy barrier associated to a critical radius, will grow by merging one with the other. This effect can be verified by looking at the concentration of bubbles decreasing with temperature while their dimension increases.
A summary of some experimental data concerning bubbles' concentration and size is reported in table (2.2).

2.2.4 Shape of the bubbles

The shapes of bubbles with different sizes and position can be completely disparate. While inter-granular bubbles tend to grow following the grain boundary to minimize their energy, intra-granular bubbles must grow spherically for the same reason, assuming they are not interacting with any defect. Small intra-granular bubbles tend to resemble spheres, but, since atoms are present in a discrete quantity, when there is only a small number of SDs the nano-bubbles do not resemble necessarily spheres.
In any case, every time the bubbles interact with other defects, such as dislocations, other bubbles or other segregates, their shape changes accordingly to minimize their internal energy [40, 41].
Finally, the shape of the bubbles is also influenced by the internal pressure of the

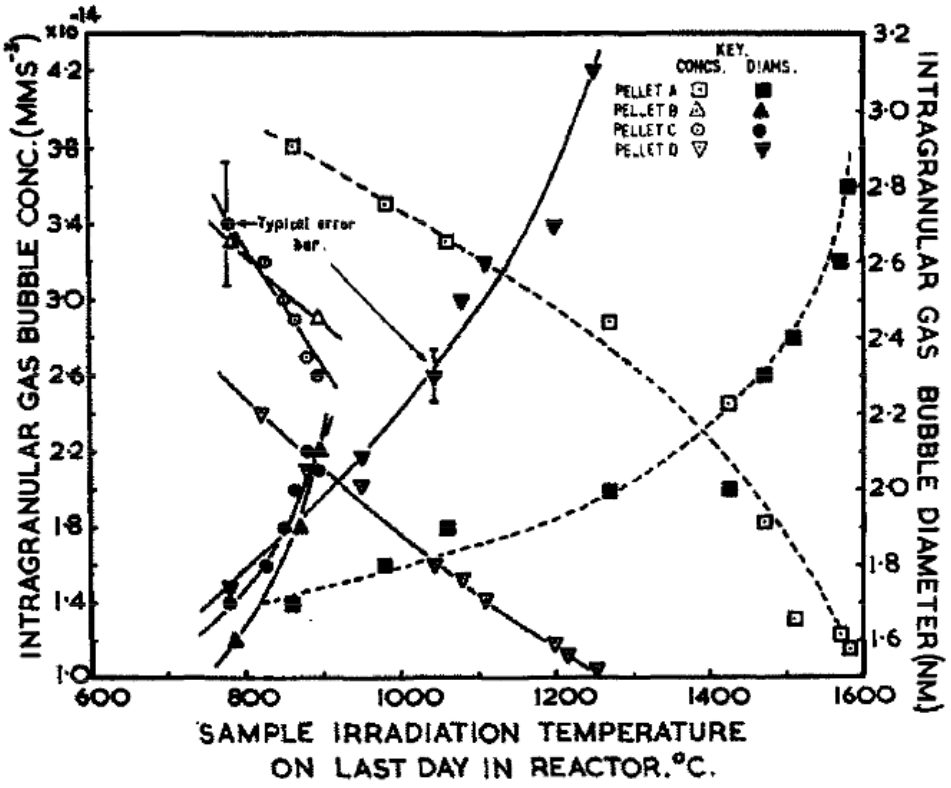

Figure 2.4: The trend of the intra-granular fission gas bubbles' concentrations and diameters as a function of the irradiation temperature on their last day in the reactor and the dose, as determined by the work of Cornell *et al.* using four different pellet samples. The pellet A results are plotted against time-averaged irradiation temperatures. [30]

fission gases: if the pressure is too high, the shape in which the bubble posses the minimum energy is not a sphere anymore, but it becomes faceted. Even the shape which minimises the energy of empty bubbles (or voids) is not a perfect sphere, but one such that the surfaces fall in a combination of the three planes {100}, {110} and {111}. This particular shape is called Wulff shape. It was proposed only recently by Galvin *et al.* [42] and in their work they also calculated the lowest energy shapes at different temperatures. A visual representation of the Wulff shape is reported in figure (2.5).
If the energy difference between the sphere and the Wulff shape is very small for voids, this value increases with the pressure of the gases inside, and it is not negligible when the xenon atoms are not gaseous anymore.
Even though the content of xenon inside the bubbles is well above the critical

R. M. Cornell work [30]			
Temperature [°C]	fissions/mm^3	Concentration [bubbles/m^3]	Size [nm]
700 – 1640	$3.5 \cdot 10^{16}$	$1.2 \cdot 10^{23}$ – $3.8 \cdot 10^{23}$	1.7 – 2.8
650 – 920	$2.3 \cdot 10^{17}$	$2.9 \cdot 10^{23}$ – $3.2 \cdot 10^{23}$	1.6 – 2.1
640 – 910	$4.6 \cdot 10^{17}$	$2.6 \cdot 10^{23}$ – $3.4 \cdot 10^{23}$	1.7 – 2.1
500 – 1275	$2.6 \cdot 10^{17}$	$1.0 \cdot 10^{23}$ – $2.4 \cdot 10^{23}$	2.1 – 3.1
K. Nogita and K. Une work in 1995 [31] at $\sim$ 400 °C $\sim$ 100 GWd/t			
Position		Concentration [bubbles/m^3]	Size [nm]
Intra-granular		$5.4 \cdot 10^{22}$	7.0
Intra-granular HBS		$9.0 \cdot 10^{23}$	2.2
Inter-granular			7.7
Inter-granular HBS		$2.0 \cdot 10^{24}$	2.1
K. Nogita and K. Une work in 1998 [32]			
Temperature [°C]	Burn-up [GWd/t]	Concentration [bubbles/m^3]	Size [nm]
$\sim$ 600	49	$4.3 \cdot 10^{23}$	4.4
S. Kashibe, K. Une, and K. Nogita work [33]			
Temperature [°C]	Burn-up [GWd/t]	Concentration [bubbles/m^3]	Size [nm]
$<$ 800	23	$9.0 \cdot 10^{23}$	2.2
$<$ 800	44	$6.7 \cdot 10^{23}$	3.9
$<$ 800	83	$4.4 \cdot 10^{23}$	4.7

Table 2.2: Summary of some of the many experimental works carried out to correlate bubbles' concentration and size depending on the irradiation temperature and burn-up.

Xe/UO_2 ratio 0.6 indicated by Galvin *et al.* over which faceted surfaces appear, in the present study spherical voids and bubbles were considered. The reason is that simulated bubbles are small enough to ignore the energy difference between the two shapes, and the discrete nature of the lattice holds a bigger importance for the shape of the bubbles.
It must be noted that the algorithm used to create the spherical voids is not the same commonly used in similar works, but it was changed in order to preserve the local charge neutrality. The details are reported in section (3.2).

2.2.5 Dimension of the bubbles

As previously discussed, the dimension of the bubbles varies dramatically from one to the other, depending on the position, the burn-up, the irradiation temperature, and many more factors. In this work nano-bubbles are analyzed, which usually

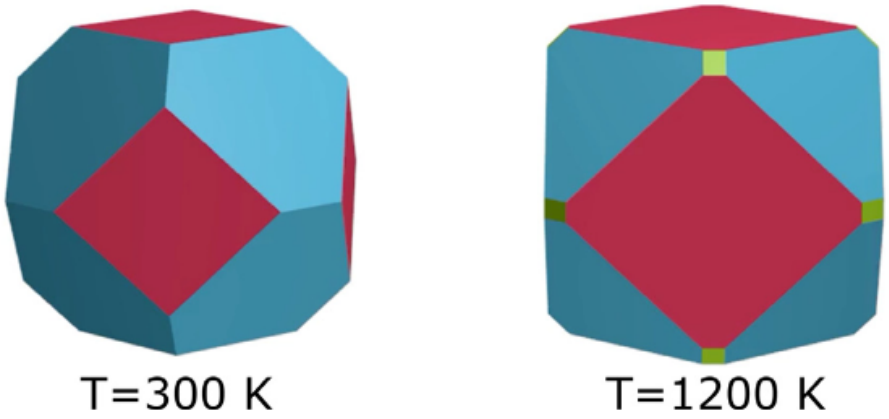

Figure 2.5: Two of the voids' shapes calculated by Galvin *et al.* [42], the distribution of the three planes, showed with different colors, changes at different temperatures. The plane {111} (in blue) is the most important one at 300 K, the plane {100} (in red) at 1200 K and the plane {110} (in green) is by far the less common at both temperatures.

range from 1 nm to 10 nm in diameter, and are more common as intra-granular and in HBSs [30, 31, 32, 33].
A relationship was proposed by Nogita *et al.* [31] between the bubbles density and their average size (2.1), where the density of bubbles N_b is expressed in m^{-3} and the bubbles' average diameter d_b in nm.

$$log\,(N_b) = -2.6\ log\,(d_b) + 25.1 \tag{2.1}$$

The size distribution of bubbles is a complex experimental topic, but some results for UO_2 exist and are reported in the figures (2.6) and (2.7). The first one is a direct representation of experimental results before and after the formation of HBS, while the second compares the sko model to other experimental results.
Three bubble sizes were analyzed in this work, the first one composed of 25 SDs, the second one by 89 SDs and the third one by 200 of them. Their respective diameters are 1.25 nm, 2 nm and 2.5 nm. These types of bubbles are a good representation of the intra-granular ones in the HBS, as shown in the picture (2.6).
In the present study a single bubble at the center of the simulation box is studied and since periodic boundary conditions are imposed on the simulation box in all directions, a system with a simple cubic distribution of bubbles is formed. It was shown that both the porosity of the structure and the distance between the bubbles change fuel properties. Here, both effects are considered. The two free parameters that change the bubble characteristic in the simulation box are the diameter of the

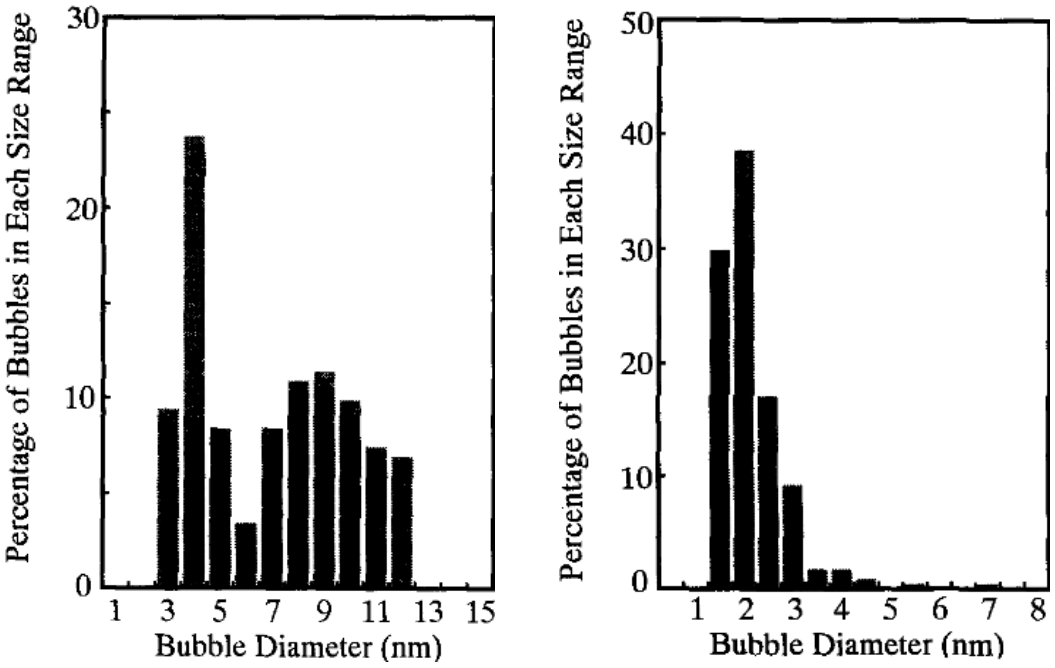

Figure 2.6: A distribution of intra-granular bubbles sizes, before restructuring on the left and after restructuring on the right. [31]

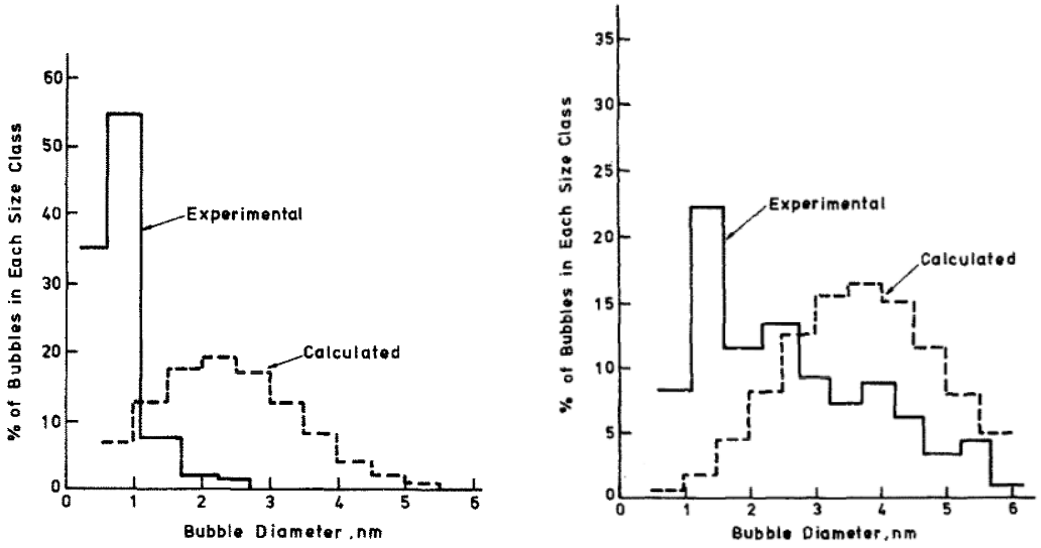

Figure 2.7: Graphical comparison between the sko model and experimental results, on the left at 1575°C and on the right at 1980°C. [39]

bubble and the size of the box. This means that the porosity, the bubbles' distance and the bubbles' concentration are all interconnected one with the others as the degrees of freedom are two. The equations (2.2),(2.3) and (2.4) report the three characteristics as a function of the parameters which can be set.

$$P \equiv \frac{V_b}{V_{tot}} \sim \frac{\frac{1}{6}\pi d^3}{c^3} \tag{2.2}$$

$$\rho \equiv \frac{number\ of\ bubbles}{V_{tot}} = \frac{1}{c^3} \tag{2.3}$$

$$L = c - d \tag{2.4}$$

In the equations above, P is the porosity, ρ is the bubbles' density and L is the distance between each bubble defined as the length separating their closest surfaces. Each of these parameters is expressed as a function of the super-cell size c and the bubbles' diameter d. The first relationship is not an equivalence because it depends on how one defines the volume of the bubble V_b as atoms are point particles in MD simulations. In the MD approximation there is not one correct answer, but many are used in the literature and the most common one is the Voronoi tessellation. The expression (2.2) however considers a different approach: it approximates the volume of the removed SDs equal to the volume of the UO_2 base molecules still present in the lattice.
In a simulation of a bulk structure, the increase in the super-cell size should not be a factor that influences the results of the simulation. In the case of structures with a bubble inside, this is no longer true, as the defects interact elastically with each other, especially at high porosities, and their distance strongly influences the simulation. The effect of the defect dissipates as the number of atoms in the simulation box increases, since the structures tends to the bulk one. This was verified in this work and it is reported in section (4.1).
Since the lattice parameter changes with the temperature, the distance between the bubbles is not fixed but increases as the temperature increases. This is due to the periodic boundary conditions and the expanding box in a NPT simulation. An other condition that influences the lattice parameter is the plutonium content, which means that the distance between the bubbles is also affected by this parameter. Even the presence or absence of the fission gases inside the bubble slightly changes the lattice parameter.
A full summary of the bubbles analysed in this work can be found in section (3.3).

2.2.6 Pressure stability

The pressure inside the bubbles is an important characteristic of the structure. It changes with temperature, plutonium content, and most importantly with the

amount of xenon atoms present inside the bubble [35, 36, 43, 44]. Yang *et al.* [44] reported important results for xenon bubbles inside UO_2 concerning their internal pressure. Some of which are shown in figure (2.8), for bubbles with 1 nm, 2 nm, 3 nm and 4 nm in diameter. It is interesting to notice how the pressure stability decreases at higher temperatures, which might be counter-intuitive, but it is due to the deformation of the surrounding lattice when the xenon atoms are too abundant in the void.

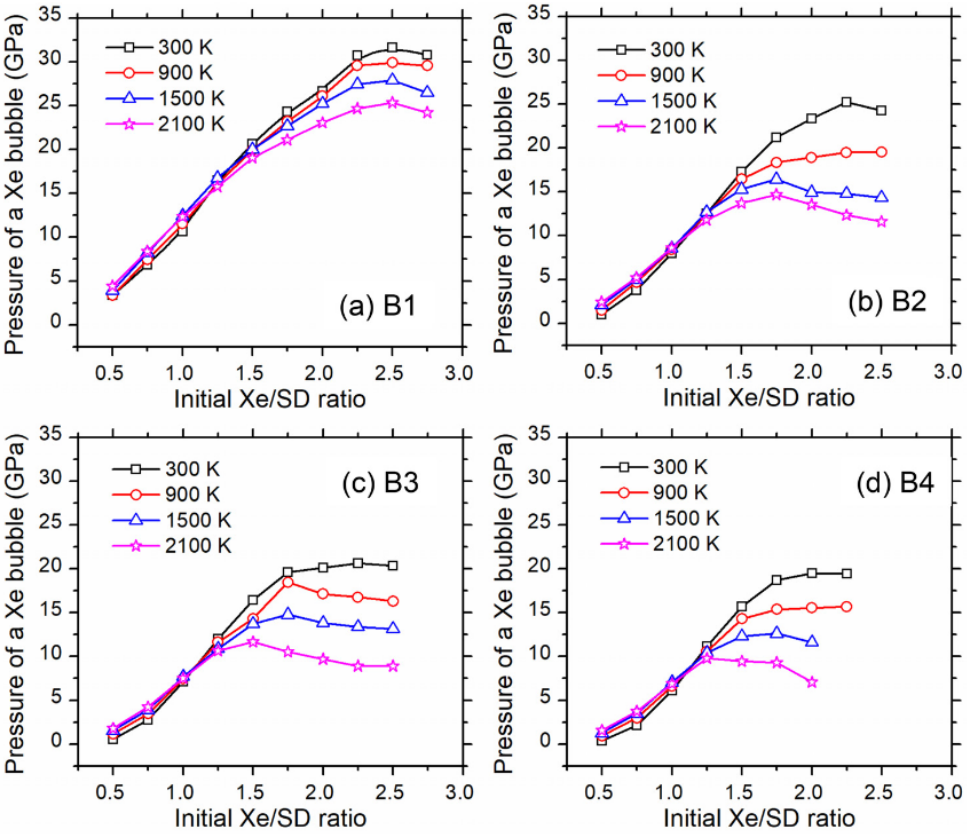

Figure 2.8: Xenon pressure as a function of temperature and Xe/SD ratio for UO_2 bubbles. (a) 1 nm in diameter, (b) 2 nm, (c) 3 nm and (d) 4 nm. [44]

The ratio between xenon atoms and SDs is indicated as Xe/SD, and for stable bubbles it is between 1 and 1.2. A ratio below 1 results in an emission of vacancies with time, by which the ratio tends to return in the stable region, while one above 1.2 results into an emission of interstitials to reequilibrate the bubble once again. The rate of vacancies and interstitials emission depends on the temperature: the higher the thermal energy, the faster the process, but any simulation above 0 K will result in a reequilibration.

In this work both empty and filled bubbles are studied. While the filled bubble have a Xe/SD ratio equal 1.2, *i.e.*, inside the equilibrium range, the empty bubbles have a ratio equal to zero, which means they are not in equilibrium. In the results presented it is possible to see that empty bubbles, at high temperature, have began to emit vacancies and disappear, but for lower temperatures this phenomenon is not visible in the time ranges of the simulations used here, which are always below 1 ns.

2.3 Plutonium usage and effects

2.3.1 The use of plutonium

Plutonium is one of the main ingredients of MOX fuels for power production, substituting uranium in quantities that vary from 1.5 wt.% to 25-30 wt.%, depending on the reactor. Plutonium is also produced in uranium oxide fuels during operation, mainly by the interaction of neutrons and ^{238}U, which is the most abundant isotope of uranium in the fuel. The formation of ^{239}Pu inside this type of fuel, which accounts for around two thirds of the total plutonium, follows the reaction (2.5). Other isotopes of plutonium are produced from ^{239}Pu following its absorption of neutrons and the consequent decay chain.

$$^{238}_{92}\mathrm{U} + ^{1}_{0}n \rightarrow \ ^{239}_{92}\mathrm{U} \xrightarrow[23.5\ \mathrm{min}]{\beta-} \ ^{239}_{93}\mathrm{Np} \xrightarrow[2.356\ \mathrm{d}]{\beta-} \ ^{239}_{94}\mathrm{Pu} \tag{2.5}$$

Since ^{239}Pu and ^{241}Pu are fissile, the reprocessing of spent uranium oxide fuels would allow to use the plutonium generated during the reactors' operation once again in fresh fuel rods part of new power cycles. This is the main way MOX fuel is produced and it is a big step toward the closure of the fuel cycle: some countries are following this path, mostly France and, to a lesser extent, Russia, India and Japan.
The plutonium content in MOX fuels for LWRs is usually around 10%, while in FNRs it can reach up to 30% [45, 46]. In the present study the full range of plutonium content was covered, with simulations of pure UO_2, pure PuO_2 and mixtures of 50% uranium and 50% plutonium randomly distributed.

2.3.2 The effects of plutonium

In the context of this work, it was proved that different plutonium distributions in the bulk do not affect the heat capacity in any way [47], unless the super-cell size is so small that the periodic boundary conditions create a particular pattern due to the low number of atoms. This, however, might not be necessarily true around defects or for other properties.

For the particular case of FGPs' bubbles, the distribution of uranium and plutonium around the defect, and particularly on the surface of the bubble, might have an impact on the properties of the material, and there might be a configuration or a set of them which minimizes the energy of the structure.
At the present, however, there are no studies on the stability of plutonium concentration on the surface of bubbles, for this reason in this work the impact of the concentration of plutonium on the surface was studied. The results, detailed in the proper chapter, conclude that there is no effect of the plutonium concentration on the surface of the bubble on the properties of the MOX fuel, at least regarding the elastic coefficients evaluation.
Due to this conclusion, a random distribution of plutonium inside the structure, including on the surface of the bubbles, was used.
In the specific case of the thermal conductivity evaluation, the effect of cathions' disorder was investigated in this work, and it was found that a higher disorder might strongly impact the thermal conductivity of MOX fuels, especially at low temperatures.

2.4 Molecular dynamics

2.4.1 Introduction to molecular dynamics

Atomistic simulations are computational methods to predict the behaviour of a group of particles by applying equations and algorithms that vary vastly from one method to the other. One of the most important of these methods is molecular dynamics, a computational method to simulate the trajectories and forces of atoms and molecules which, in its most common form, solves Newton's law of motion numerically for a system of particles.
MD can either calculate the forces between atoms using classical potentials or ab-initio methods, *i.e.*, solving Schrodinger equation. In its more complex version, MD algorithms evaluete directly the trajectory of atoms by quantum means. In this document only classical means where used.
Other atomistic methods exist, such as density functional theory (DFT) and Monte Carlo methods. DFT is used in atomic physics to simulate the electronic shell around nuclei using the non-relativistic Schrödinger equation for all the electrons of the system. This quantum-level depiction of atoms offers higher precision compared to classical models, especially when specific atomic characteristics are not accurately captured by the trajectory of whole atoms. The DFT algorithms are ab initio (or first principles) methods, as no parameter characterizing the Hamiltonian of the system is related to empirical data. Simulation results are thus independent from any empirical observation. DFT calculations are also much more computationally demanding than MD, and to run them for the same time ranges

and the same number of atoms as MD would be impossible, even with the current rapid technological advancement of high-performance computers (HPCs).
While MD and DFT methods are referred to as deterministic methods, Monte Carlo methods are by definition stochastic in their nature. The idea behind them is to repeat many times the same calculation with a different input random sample, it usually is less computationally expensive than MD and it is used to slightly larger scales than the former. Monte Carlo methods, as well as MD and DFT methods are effective and well known tools commonly used in the nuclear fuel industry, each for its scale and applications.
The use of classical mechanics in MD translates into some approximations of the phenomena involved in the dynamics with respect to DFT methods. One of the most important is the Born–Oppenheimer approximation, according to which the mass of the electrons is negligible compared to the one of nuclei. This leads to treat the dynamic of the former as instantaneous in the scale of MD.
In purely classical MD methods, another key approximation is the treatment of nuclei as point particles following classical Newtonian laws. From these laws MD methods calculate the trajectories of the atoms. From a known scalar potential U one can calculate the force applied to an object with equation (2.6).

$$\mathbf{F} = -\boldsymbol{\nabla} U \tag{2.6}$$

In MD, the most simple potentials are only a function of the distance between two particles, $U_{ij} = U(\|\mathbf{r_i} - \mathbf{r_j}\|)$ and so is the force between the two. MD algorithms calculate all the forces applied on the atoms inside the box at every time step, and from the forces use Newton's second law of motion (2.7) to calculate the resulting position after the time step.

$$F_i = \sum_{j \neq i} F_{ij} = m_i \frac{d^2}{dt^2} r_i \tag{2.7}$$

The integration of the force applied to the particles is not as easy as it might seem, and it requires specific algorithms detailed below.
Every MD simulation needs an initial structure with the atoms' positions and velocities, as well as an inter-atomic potential. From these few ingredients many different simulations can be carried out fixing diverse parameters and obtaining disparate results. Some of the parameters that can be fixed are:

- Total simulation time and time step.
- Boundary conditions of the system.
- Two thermodynamic coordinates, *i.e.*, the ensemble of the simulation.

The total simulation time is entirely up to the user to decide but it should be long enough to represent a physically meaningful set of structures in time depending on the desired output. At the same time, it should not be too long since the computational speed is limited by the technological resources one can work with. The time step of the simulation must be chosen considering what type of atoms are present in the simulation box as well as the desired results expected. For example, to investigate the diffusion of hydrogen one would need a very small time step compared to the one needed for the diffusion of a heavy metal atom, since the process is much faster in the first case because of the much smaller mass of hydrogen. At the same time, for the same reason, the former case will need a much smaller total simulation time than the latter.

2.4.2 Boundary conditions

Every face of the simulation box needs a boundary condition for the simulation to run, many of these can be defined, but the ones that are usually used because of their physical meaning are the following:

- Periodic.
- Non periodic and fixed.
- Non periodic and shrink-wrapped.
- Non periodic and shrink-wrapped with a minimum value.

By far the one used more often in the nuclear fuel field is the first condition. The periodicity of the surfaces lets the atoms move through the surface itself and interact with each other via the potential even if the surface is separating them. This boundary condition can be seen as a replication of the super-cell many times in the direction of the imposed condition, and by applying it one can simulate materials theoretically stretching indefinitely. This is not the real case of course, since the simulations lacks macroscopic effects that, in the case of nuclear fuels, are the multi-crystalline nature of the material, the vast amount of defects and their distribution, the gradients in thermodynamic quantities, and so on.
For some specific cases one can use non periodic boundary conditions, the first of which imposes a fixed boundary that, if crossed by a particle, deletes the atom from the simulation all-together.
Instead of fixing the position of the boundary one can move it freely setting a constant distance between the closest atom and the surface, this is the case of the third boundary condition. The problem with this method is the possibility to shrink the box too much during the equilibration procedure, for this reason one can fix a minimum value for the shrinkage and let it expand from there. This is the case of the last condition.

2.4.3 Ensembles

The ensemble of the system defines what thermodynamical coordinates are fixed, the options usually adopted for the standard applications are the following, even if an infinite amount could be theoretically defined.

- NVE - Microcanonical ensemble.
- NVT - Canonical ensemble.
- NPT - Isothermal–isobaric ensemble.
- NPH - Isoenthalpic–isobaric ensemble.

The abbreviation indicates what parameters are being fixed, N, for example, is the number of moles, and it is always fixed. The volume is V, the temperature is T, the energy is E, the pressure is P, the enthalpy is H.
The NVE ensemble simulates an adiabatic process, in which the mechanical energy of the system is conserved throughout all the simulation and the only exchange in energy is between the potential energy and the kinetic energy of the particles. The NVE ensemble simulates a closed system, as it does not require any thermostat or barostat and it is theoretically faster than the other ensembles.
In an NVT simulation the system is free to exchange energy with a thermostat in order to keep the temperature constant, it is a difficult task to do this in a physically realistic way and many algorithms exist for different applications and cases. The most popular ones include Langevin dynamics, the Andersen thermostat, the Berendsen thermostat, Nosé–Hoover chains and Nosé–Hoover thermostat.
NPT simulations not only need a thermostat but also a barostat, which adjusts the pressure at every time step to keep it constant at the desired value. Some of the algorithms used for barostats include Berendsen barostat, Parrinello-Rahman barostat, Nosé-Hoover barostat and Martyna-Tuckerman-Tobias-Klein (MTTK) barostat.
The NPH ensemble fixes the enthalpy $H \equiv E + PV$ and it is used for very specific applications, such as the evaluation of the Joule–Thomson coefficient and the supercritical point.

2.4.4 Molecular statics

Molecular statics (MS) are algorithms to minimize the energy of a system, usually they are iterative processes and the most important ones include the first-order steepest descents method, sometimes called conjugate gradient, and the second-order Newton-Raphson method, also called Quasi-Newton's.
By definition, MS simulations are not dynamic and they return a single structure

fixed in time, if the algorithm works efficiently the solution is close to the global minimum energy configuration, without converging toward a local minimum. This is of course a difficult task, and it gets harder the more complex is the initial structure, *e.g.*, with an abundant presence of defects or a high level of atomic disorder.
If the global minimum is reached the final structure is at 0 K, as the atoms are fixed at the lowest energy position and there are no resulting forces to accelerate them. Since the MS do not take into account quantum effects the zero point energy is neglected during the minimization.

2.4.5 Inter-atomic potentials

The inter-atomic potentials describe how the particles in the system interact, they can be as simple as tabulated curves or they might be more complex and include, for some aspects, charge distribution. The potentials describe the force field surrounding the particles in the super-cell.
Empirical potentials try to represent the effects of the atomic interactions via specific functions that are fitted with the use of DFT calculations or experimental data. Due to the long range nature of the interaction between particles, to avoid a truncation error theoretically one should calculate the interaction of every atom with every other atom, but this is of course not possible. In order to avoid this problem, numerical approximations are used, such as the shifted cutoff radii, reaction field algorithms, particle–particle-particle–mesh (P3M), or the Ewald summation.
The simplest type of potential is the pair potential, in which the potential is just a function of the pair of atoms considered. An example of pair potential, and also the simplest and most famous potential in general is the Lennard-Jones (LJ) potential (2.8).

$$U(r) = 4\varepsilon \left[\left(\frac{\sigma}{r} \right)^{12} - \left(\frac{\sigma}{r} \right)^{6} \right] \tag{2.8}$$

The LJ potential is one of the simplest type of potential as it can be derived directly from two oscillating dipoles, *i.e.*, two atoms interacting via the London interaction, and from experimental data that reproduce the repulsive interaction caused by the Pauli exclusion principle [48]. The LJ potential reproduces well gases and neutral atoms, its generic graphical representation is proposed in figure (2.9).
The terms ε and σ represent respectively the depth of the potential well and the distance at which the potential is null. They are usually referred to as dispersion energy and size of the particle.
Another example of pair potential is the Coulomb–Buckingham potential, expressed in equation (2.9), which instead works better for ionic crystals, for which it was proposed. Both the LJ potential and the Coulomb–Buckingham one have many alternative forms depending on the system analyzed and on the simulation goals.

The Coulomb–Buckingham itself is an extension of the Buckingham potential which was proposed as an alternative to LJ for gaseous systems.

$$U(r) = A\exp\left(-Br\right) - \left(\frac{C}{r}\right)^6 + \frac{q_1 q_2}{4\pi\varepsilon_0 r} \tag{2.9}$$

In the Coulomb–Buckingham potential, the van der Waals energy term is substituted to the LJ one, A, B and C are constants that were fitted with experimental data for different materials. In both potentials, the term r is the distance between the two atoms, the two potentials do not depend on other atoms as they are pair potentials.

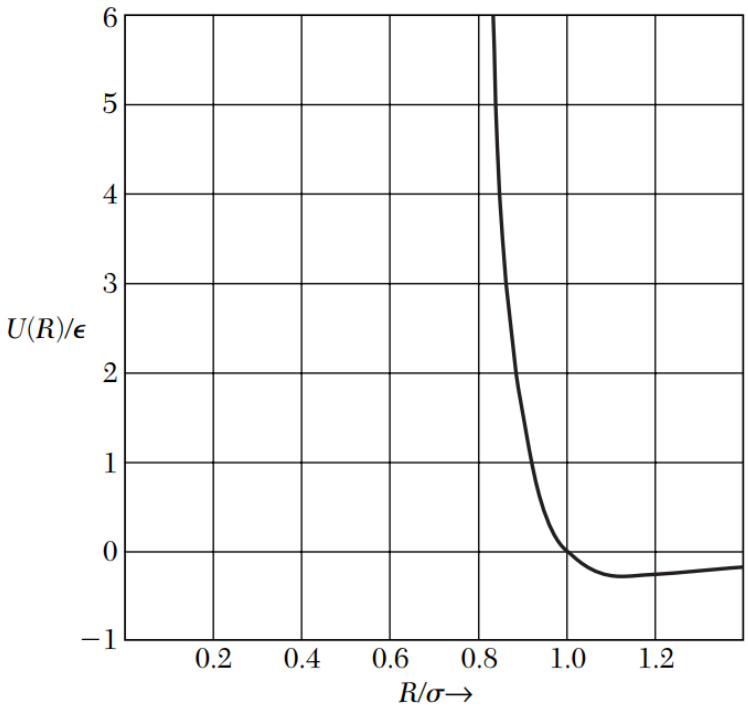

Figure 2.9: The graphical representation of the Lennard-Jones potential for a generic gas. [48]

In many-body potentials, the potential energy depends on more than two atoms. This complicates the method but adds the precision necessary for most of the system to have reliable results. An example of many-body potential is the Cooper-Rushton-Grimes (CRG) potential, which is used in this work.
The CRG model was proposed in 2014 by Cooper *et al.* as an alternative to already existing potentials for actinide oxides, which, for example, are imprecise in the simulation of the elastic constants and did not reproduce the Cauchy violation.

In a first paper [49], the potential for Ce, Th, U, Np, Pu, Am, Cm and O was presented, while in a following paper [50], in 2016, they also included the fission gases Xe and Kr into the model.
The CRG potential is defined in equation (2.10), in which a pairwise component and a many-bodied one describe the potential related to the atom i, respectively the first and the second term of the definition.

$$U_i = \frac{1}{2}\sum_j \phi_{\alpha\beta}\left(r_{ij}\right) - G_\alpha\sqrt{\sum_j \sigma_\beta\left(r_{ij}\right)} \tag{2.10}$$

The pairwise term (2.11) accounts for the electrostatic interaction using the potential in equation (2.12) and for short range interactions using Morse's potential (2.13) and Buckingham's (2.14).

$$\phi_{\alpha\beta}\left(r_{ij}\right) = \phi_C\left(r_{ij}\right) + \phi_B\left(r_{ij}\right) + \phi_M\left(r_{ij}\right) \tag{2.11}$$

$$\phi_C\left(r_{ij}\right) = \frac{q_\alpha q_\beta}{4\pi\varepsilon_0 r_{ij}} \tag{2.12}$$

$$\phi_M\left(r_{ij}\right) = D_{\alpha\beta}\left[\exp\left(-2\gamma_{\alpha\beta}\left(r_{ij}-r_0\right)\right) - 2\exp\left(-\gamma_{\alpha\beta}\left(r_{ij}-r_0\right)\right)\right] \tag{2.13}$$

$$\phi_B\left(r_{ij}\right) = A_{\alpha\beta}\exp\left(\frac{-r_{ij}}{\rho_{\alpha\beta}}\right) - \frac{C_{\alpha\beta}}{r_{ij}^6} \tag{2.14}$$

The second term is used by Cooper *et al.* to account for the many-body part of the potential via the embedded-atom method (EAM). The functions $\sigma_\beta(r_{ij})$ are shown in equation (2.15), in which the error function is used to prevent the EAM term to interfere with the short range interactions below 1.5 Å.

$$\sigma_\beta\left(r_{ij}\right) = \left(\frac{n_\beta}{r_{ij}^8}\right)\frac{1}{2}\left(1 + erf\left(20\left(r-1.5\right)\right)\right) \tag{2.15}$$

Many other types of potentials exist, it is worth mentioning the semi-empirical potentials, polarizable potentials or quantum-mechanical molecular mechanics (QM/MM) potentials.

2.4.6 Algorithms for molecular dynamics

As expressed above, MD is the simple numerical implementation of Newton's law of motion for a many body system. Its pseudo-code can be expressed as the one below.

```
program md

call init
```

```
t=0
do while (t<tmax)
     call force(f,en)
     call integrate(f,en)
     t=t+delt
     call sample
enddo
stop
end
```

After an initialization of the system the dynamic starts, with discrete time steps. At each step the forces are computed from the potential and then integrated to obtain the new positions of the particles. Most of the MD software use Störmer-Verlet's algorithm [51, 52], usually simply called Verlet's algorithm, to integrate Newton's equations of motion and obtain the new coordinates, which implements a central difference approximation to the second derivative. At every integration step n the new position of each particle is calculated using equation (2.16).

$$\mathbf{r}_{n+1} = 2\mathbf{r}_n - \mathbf{r}_{n-1} + \mathbf{a}_n \Delta t^2 \tag{2.16}$$

Here $\mathbf{a}_n$ is the acceleration of the particle and it comes directly from the force evaluation.
Verlet's algorithm provides good numerical stability and time reversibility, other algorithms exist to be used instead of Verlet's one, like Euler method or a generic Taylor expansions, but they are rarely used.
In LAMMPS, the default thermostat is the Nosé–Hoover one [53, 3], which simply adds a term to the Hamiltonian for the fictitious presence of the heat bath, so that it becomes as in equation (2.17).

$$\mathcal{H} = \sum_i \frac{\mathbf{p}_i^2}{2ms^2} + \frac{1}{2} \sum_{i,j,i \neq j} U\left(\mathbf{r}_i - \mathbf{r}_j\right) + \frac{p_s^2}{2Q} + g k_B T \ln\left(s\right) \tag{2.17}$$

While the first and second term represent the kinetic and potential energy of the real particles, the third and fourth ones represent the corresponding energies for the fictitious coordinate s, which momentum is p_s and mass is Q. The parameter Q must be chosen with care to obtain realistic results. In LAMMPS' algorithm the rate of relaxation of the thermostats is expressed by one single parameter called T_{damp}: the higher T_{damp} is, the less the temperature fluctuates, but it also takes more time to equilibrate. A trade-off is thus required in the implementation of the code.
The Nosé–Hoover barostat is also the default in LAMMPS, its inertia is again controlled by one single parameter, called p_{damp}. The inertia depends on the target

temperature [54] and its evaluation is reported in equation (2.18).

$$W = (N+1)\, k_B T_{target} p_{damp}^2 \tag{2.18}$$

In order to simulate the long range interactions of the potentials it would seem that the MD algorithms should iterate over an infinite amount of particles, but to avoid to simply truncate the summation at a cut-off the MD algorithms resort to Ewald's summation. Ewald summation divides the potential into two terms, separating them at a cut-off distance, like in equation (2.19).

$$U(\mathbf{r}) = U_{sr}(\mathbf{r}) + U_{lr}(\mathbf{r}) \tag{2.19}$$

By assuming that the system is infinitely periodic, a Fourier transform can be applied to the long range interactions U_{lr}, this term quickly converges in Fourier's reciprocal space, while the short range interaction quickly converges in the real space.
As seen above, other methods exist to calculate the long range interactions, one of these is the P3M algorithm, or PPPM algorithm. The method is very similar to Ewald's one, but it scales as N, instead of $N^{\frac{3}{2}}$, where N is the number of particles in the simulation box. In all the simulations carried out in this work the P3M method was used to calculate the long range interactions.

Chapter 3

Methods and assumptions

3.1 Working process overview

The process of calculating the properties of the desired structures included the following steps:

1. Creation of the structures
2. Evaluation of the properties
3. Evaluation of the uncertainties
4. Post-processing the results

In this chapter the parts of this process are explained in detail.

3.2 Creation of the structures

The complete process to generate the structures is divided in smaller and easier steps, each of which uses different tools and languages.
In the first step, by starting from a simple UO_2 fluorite structure with 12 atoms, and replicating it in the three dimensions, a super-cell of the desired size is created. In the majority of the previous studies [43, 55] about xenon bubbles in UO_2 using MD, the method to create the bubble was straightforward: to remove the atoms from the central position up to a certain radius, without accounting for the elements position and possibly creating a charged surface. The problem is usually solved by adding or removing the right amount of oxygen atoms randomly near the surface of the bubble, to neutralize the total charge. The issue with this method, however, is that the local charge is not conserved and different parts of the surface are likely to have a local electrical charge. This phenomenon is worsened with an

increasing bubble size and at lower temperatures. A bigger surface will have a higher chance of randomly generate oxygen atoms in the wrong position, while a lower temperature leads to a lower mobility of the oxygen atoms that will not easily relocate to minimize the potential energy once again. If the temperature reaches the Bredig transition [14] the oxygen sub-lattice melts, completely overcoming the relocation issue and avoiding a locally charged surface.
Due to these problems with the previous method to create the structure with the spherical void, an other one was used in this study. Starting from the central position of the void, the closest metal atom was selected and deleted. After the first metal atom was deleted a second metal atom is selected close to the first one, and two of the four oxygen atoms neighbouring both the metal atoms are deleted as well. The second metal atom is then selected as the closest to the center of the void and the process continues until the right amount of Schottky defects is inserted and the void is formed. By using this method the local charge is effectively conserved and there are no issues at low temperatures and with bubbles too large. This first step is done with python and the OVITO library, and its scheme is reported in figure (3.1).

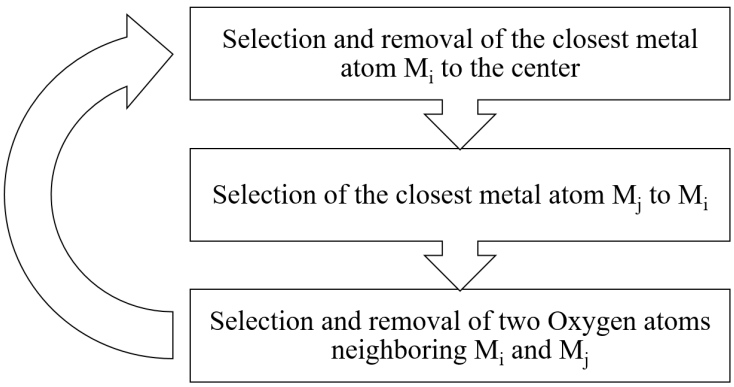

Figure 3.1: Scheme of the algorithm used to create the void structure, starting from the center and deleting the desired amount of UO_2 atoms while conserving the local charge.

In the second step, the desired amount of uranium is substituted with plutonium. In this study the only three cases are pure UO_2, pure PuO_2 and 50% of each, distributed randomly, but it was possible to create a structure with any amount of U and Pu. This process is again carried out using python, the algorithm is reported in figure (3.2).
The third and final step is used to add xenon atoms inside the void previously created. This operation is the most critical one, and attention must be paid in

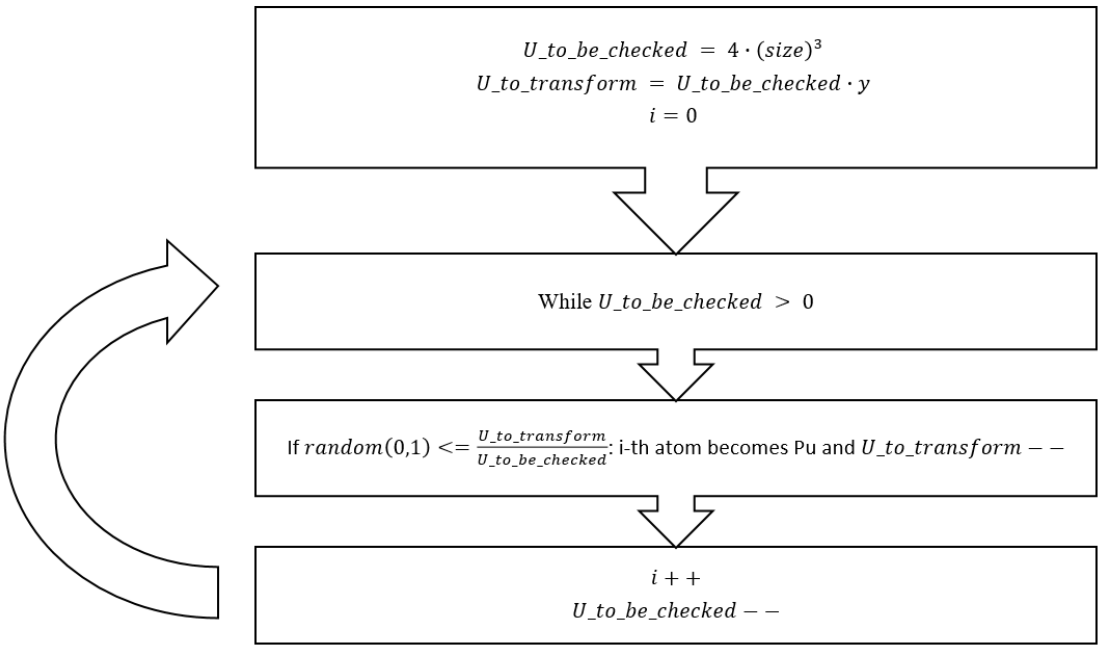

Figure 3.2: Scheme of the algorithm used to substitute uranium atoms with plutonium, y is the desired plutonium concentration and $size$ is the number of atoms composing each edge of the simulation box.

order to avoid creating a non-physical and unstable structure, that would either give useless results or no results at all.
To add the xenon, a simulation at low temperature, 100 K, in the NVT ensemble, was used, to prevent the newly introduced xenon atoms to exaggeratedly expand the structure in a nonphysical way. After minimizing the system, xenon atoms were added, one at a time, in the spherical empty region at the center of the structure, randomly. They were also added far enough from any other atom to avoid destroying the structure. At least 50 ps passed between the insertion of two different xenon atoms, to be sure that they would settle in the most stable location without destabilizing the structure too much.
The oxidation numbers of the uranium and of the plutonium were both fixed at +4, because in this study only stoichiometric cases were considered: it might be the subject of future works the expansion of the present results to more generic hypo-stoichiometric and hyper-stoichiometric structures. In figure (3.3) it can be seen an example of a structure with a xenon bubble.

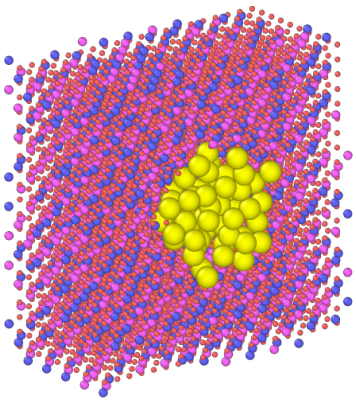

Figure 3.3: A structure with a xenon bubble, sliced in order to see inside of it. The oxygen atoms are in red, the plutonium in purple, the uranium in blue and the xenon in yellow. The radius of the xenon particles is shown much bigger than the rest to highlight the big presence they pose by being a noble gas and thus having their electron orbitals full.

3.3 Summary of the bubbles studied

In this section one can find a summary of the studied bubbles characteristics, chosen based on experimental results on real materials and on the available computational power available for the project. The full bibliographic work can be found in the previous chapter.
The following structures were analyzed: a bubble 1.25 nm in diameter in a 6x6x6 super-cell, a bubble 1.25 nm in diameter in a 10x10x10 super-cell, a bubble 2 nm in diameter in a 9x9x9 super-cell, a bubble 2 nm in diameter in a 11x11x11 super-cell, a bubble 2.5 nm in diameter in a 10x10x10 super-cell and a bubble 2.5 nm in diameter in a 12x12x12 super-cell. These numbers are also reported in the table (3.1).
The super-cell size is directly related to the bubbles' density, as explained in the previous chapter. Table (3.2) shows the bubble density corresponding to each super-cell size, the values refer to structures at 1000 K and they are indicated for $(U_{1-y},Pu_y)O_2$ with y equal to 0, 0.5 and 1. The effect of the bubble size is neglected in the following table, as well the internal xenon pressure.
It is important to notice that the bubble density analyzed in this work is around half order of magnitude higher than the experimental results, detailed in the previous

	25 Schottky defects 1.25 nm in size		**89 Schottky defects** 2 nm in size		**200 Schottky defects** 2.5 nm in size	
6x6x6 864 bulk metal atoms	Porosity 2.894%	Distance 27.05 Å				
9x9x9 2916 bulk metal atoms			Porosity 2.984%	Distance 39.95 Å		
10x10x10 4000 bulk metal atoms	Porosity 0.625%	Distance 49.25 Å			Porosity 5.000%	Distance 43.00 Å
11x11x11 5324 bulk metal atoms			Porosity 1.634%	Distance 51.05 Å		
12x12x12 6912 bulk metal atoms					Porosity 2.894%	Distance 54.10 Å

Table 3.1: The six structures analyzed in order to investigate both the effect of porosity and the distance between the bubbles (*i.e.*, the super-cell size). In fact the porosity 2.894% is present twice. In particular, the distance between the bubbles refers to the one at 2000 K with 50% Pu content. For each structure an analysis of the full and empty bubble, with different plutonium contents and in a wide range of temperatures is carried out.

	UO_2	$(U_{0.5},Pu_{0.5})O_2$	PuO_2
6x6x6 864 bulk metal atoms	$2.76 \cdot 10^{25}$ m^{-3}	$2.82 \cdot 10^{25}$ m^{-3}	$2.88 \cdot 10^{24}$ m^{-3}
9x9x9 2916 bulk metal atoms	$8.20 \cdot 10^{24}$ m^{-3}	$8.38 \cdot 10^{24}$ m^{-3}	$8.57 \cdot 10^{24}$ m^{-3}
10x10x10 4000 bulk metal atoms	$5.98 \cdot 10^{24}$ m^{-3}	$6.11 \cdot 10^{24}$ m^{-3}	$6.23 \cdot 10^{24}$ m^{-3}
11x11x11 5324 bulk metal atoms	$4.49 \cdot 10^{24}$ m^{-3}	$4.59 \cdot 10^{24}$ m^{-3}	$4.68 \cdot 10^{24}$ m^{-3}
12x12x12 6912 bulk metal atoms	$3.46 \cdot 10^{24}$ m^{-3}	$3.54 \cdot 10^{24}$ m^{-3}	$3.60 \cdot 10^{24}$ m^{-3}

Table 3.2: The bubble density of the structures considered at 1000 K.

chapter, while the porosity is very similar to the one caused by nano-bubbles observed during measurements. Bigger simulation boxes will represent better the effect of the experimental bubbles, as the density decreases, and the structures with

864 bulk metal atoms (2592 total bulk atoms) are the less accurate, but they are still kept for comparison. The reason behind the difference in the bubble density is due to the nature of the MD simulations that are presented in this work: a simulation of a bubble with the correct bubble density would require too severe computational costs, as the number of atoms surrounding the bubble would need to considerably increase.

3.4 Evaluation of the properties

3.4.1 Heat capacity and linear thermal expansion coefficient

The heat capacity is a property defined as the amount of heat that a material needs to absorb in order to increase its temperature of one unit.

$$C \coloneqq \frac{dQ}{dT} \tag{3.1}$$

In this work the specific molar heat capacity was calculated at constant pressure, as reported in equation (3.2), and in particular at zero pressure.

$$c_p \coloneqq \frac{1}{n}\left(\frac{\partial Q}{\partial T}\right)_p = \frac{1}{n}\left(\frac{\partial H}{\partial T}\right)_p \tag{3.2}$$

In practice, during the simulations, the enthalpy was used instead of using the heat, following the conservation of energy (3.3) and the isobar nature of the simulations (3.4).

$$dQ - PdV = ndU \tag{3.3}$$

$$\frac{dQ}{n} = dU = \frac{dH}{n} - VdP - PdV = \frac{dH}{n} \tag{3.4}$$

Following each MD simulation, a value for the enthalpy is found at each temperature, from this value the heat capacity can be calculated using the equations (3.5) and (3.6). The subscript p is dropped since the simulations are always at constant pressure.

$$h \coloneqq \frac{H}{n} \tag{3.5}$$

$$c_p\left(\frac{T_i + T_{i-a}}{2}\right) = \frac{\Delta h}{\Delta T} = \frac{h\left(T_i\right) - h\left(T_{i-a}\right)}{T_i - T_{i-a}} \tag{3.6}$$

The parameter a must be chosen in order to get ΔT equal to 150 K, as it was proved to give the highest accuracy for MD simulations with very similar conditions by Bathellier *et al.* [47]: they used the same inter-atomic empirical potential, similar super-cell sizes and bulk structures with the same plutonium contents (0%, 50%

and 100%) instead of bubbles. Since the simulations were carried out every 50 K, the correct value of a is 3. This law was validated from 1000 K to the melting points of the MOX compound, as below 1000 K quantum effects are not negligible and MD is no longer valid.
Equation (3.6) shows that the only parameter to measure in the MD simulation is the average atomic enthalpy of the system: the process used to measure it is expressed below.
The volumetric thermal expansion coefficient is an intensive property that describes how much a material deforms when its temperature changes, it is defined as reported in equation (3.7).

$$\alpha_V \coloneqq \frac{1}{V}\left(\frac{\partial V}{\partial T}\right)_p \tag{3.7}$$

Instead of the volumetric thermal expansion, one is usually interested in the linear thermal expansion coefficient (LTEC), in which the expansion is referred to a characteristic length instead of a volume.

$$\alpha_L \coloneqq \frac{1}{L}\left(\frac{\partial L}{\partial T}\right)_p \tag{3.8}$$

In isotropic materials, such as (U,Pu)O_2, the relationship (3.9) between the two TECs can be used, as the direction in which the deformation is taking place does not change the coefficient.

$$\alpha_L = \alpha_V/3 \tag{3.9}$$

In this work, the method used to calculate the LTEC is very similar to the one used to calculate the specific heat, since in both cases an isobar derivative over temperature is required. Instead of calculating the enthalpy in a new NPT simulation, the volume is obtained from the same simulation. After obtaining the volume at constant pressure for each of the desired temperatures the equation to evaluate the LTEC is thus the following (3.10).

$$\alpha_L\left(\frac{T_i + T_{i-a}}{2}\right) = \frac{1}{3}\frac{1}{V_0}\frac{\Delta V}{\Delta T} = \frac{1}{3V\left(T_0\right)}\frac{V\left(T_i\right) - V\left(T_{i-a}\right)}{T_i - T_{i-a}} \tag{3.10}$$

In equation (3.10) the volume V_0 is calculated at the reference temperature T_0 which is the room temperature. In this work the value of T_0 was fixed at 300 K. The value of a is equal to 3 also in this case, for the reason reported above.
To calculate the enthalpy and the volume, firstly the structure is thermalized at the desired temperature with a Gaussian distribution, and then an equilibration is imposed for 120 ps. By using different steps to increase the T_{damp} and p_{damp} parameters of the thermostat and the barostat during the equilibration, one allows the structure to rapidly reach the desired thermodynamic state with large

oscillations, and once this is reached the oscillations are reduced until a precise enough state is obtained. The parameters used at different times are summarised in table (3.3). They are the same for every temperature and structure, and were chosen to give good results for the highest temperatures, since these are the ones that the thermostats lets naturally oscillate more.

Time $[ps]$	T_{damp} $[fs]$	p_{damp} $[fs]$
10	1.00	1.00
10	10.0	10.0
100	100	10.0
500	100	10.0

Table 3.3: Summary of the T_{damp} and p_{damp} parameters used for the equilibration and, in the last row, for the enthalpy and volume measurement.

As reported in table (3.3), the simulations lasted a totality of 620 ps each, but only in the last 500 ps the properties were outputted in order to be averaged at the end and give the final result. The time-step used for the simulation is 1 fs, and the thermodynamic data are saved from the simulation every 10 fs, in order to have a large enough sampling size while keeping the values independent from each previous time step.

3.4.2 Elastic coefficients

In most of the materials, the elastic region of the force-displacement curve is linear, and the steepness of this curve is referred to as elastic coefficient. This property can be generalized in three dimensions and the resulting coefficient becomes a tensor, that can be expressed in Hooke's law (3.11).

$$\sigma_i = C_{ij}\varepsilon_j \tag{3.11}$$

In Hooke's law, σ_i is the stress vector and ε_j the respective strain, the two indices range from one to six, resulting in a tensor matrix of thirty six values. In a generic material, of these thirty six values only twenty one are independent, due to the symmetries, and in general they are non-zero. In the majority of the applications the degrees of freedom decrease even more because of the specific peculiarities of the material studied, such as orthotropicity and isotropicity.
For example, in isotropic materials, such as (U,Pu)O_2, the number of independent

coefficients typically decreases to just three, and equation (3.11) becomes (3.12).

$$\begin{pmatrix}\sigma_{11}\\ \sigma_{22}\\ \sigma_{33}\\ \sigma_{23}\\ \sigma_{31}\\ \sigma_{12}\end{pmatrix} = \begin{pmatrix}C_{11} & C_{12} & C_{12} & 0 & 0 & 0\\ C_{12} & C_{11} & C_{12} & 0 & 0 & 0\\ C_{12} & C_{12} & C_{11} & 0 & 0 & 0\\ 0 & 0 & 0 & C_{44} & 0 & 0\\ 0 & 0 & 0 & 0 & C_{44} & 0\\ 0 & 0 & 0 & 0 & 0 & C_{44}\end{pmatrix} \begin{pmatrix}\varepsilon_{11}\\ \varepsilon_{22}\\ \varepsilon_{33}\\ 2\varepsilon_{23}\\ 2\varepsilon_{31}\\ 2\varepsilon_{12}\end{pmatrix} \tag{3.12}$$

The coefficients C_{12} and C_{44} are identical for many materials. This effect is described by Cauchy relation. Another group of isotropic materials, which (U,Pu)O_2 oxides are part of, experimentally shows the opposite behaviour, referred to as Cauchy violation, in which $C_{12} \neq C_{44}$.
In this work the coefficients C_{11}, C_{12} and C_{44} were calculated as a function of temperature, plutonium content and bubbles' characteristics, together with other elastic properties that can be directly derived from the three independent tensor's coefficients. These properties are the bulk modulus K, the shear modulus G, the Young modulus E and the Poisson coefficient ν.
The way these properties were calculated from the coefficients C_{11}, C_{12} and C_{44} is not the most common one, but instead an adaption for randomly orientated poly-crystalline materials proposed by Hill [56] was used. In Hill's proposal, the bulk modulus is suggested to remain the same for mono-crystalline materials and poly-crystalline ones. Equation (3.13) shows how it was evaluated.

$$K_{mono} = K_{poly} = \frac{C_{11} + 2C_{12}}{3} = K \tag{3.13}$$

The same thing does not apply for the other coefficients that were calculated. The evaluation of the shear modulus is provided by equations (3.14), (3.15), (3.16), (3.17); the one of the Young modulus by equations (3.18), (3.19) and the one of the Poisson coefficient by equations (3.20), (3.21).

$$G_{mono} = \frac{C_{11} - C_{12}}{2} \tag{3.14}$$

$$G_{Reuss} = \frac{5\,(C_{11} - C_{12})\,C_{44}}{4C_{44} + 3\,(C_{11} - C_{12})} \tag{3.15}$$

$$G_{Voigt} = \frac{C_{11} - C_{12} + 3C_{44}}{5} \tag{3.16}$$

$$G_{poly} = \frac{C_{Reuss} + C_{Voigt}}{2} \tag{3.17}$$

Hill proposed to use the Voigt-Reuss model for the shear modulus with poly-crystalline materials, which is the average between the axial loading (Voigt) and the

transverse loading (Reuss), both useful to calculate several mechanical properties in material science. The Voigt-Reuss model is also able to provide upper and lower bounds for the calculated properties.

$$E_{mono} = C_{11} \tag{3.18}$$

$$E_{poly} = \frac{9KG_{poly}}{3K + G_{poly}} \tag{3.19}$$

$$\nu_{mono} = \frac{1}{1 + C_{11}/C_{12}} \tag{3.20}$$

$$\nu_{poly} = \frac{E_{poly}}{2G_{poly}} - 1 \tag{3.21}$$

In the MD simulations, the approach to evaluate the stress coefficients is based on a systematic deformation of the simulation box in the directions x, y, z, xy, yz, zx and the measure of the resulting stress.
In practice, equation (3.22) is used, which is composed by a kinetic term and a virial one, evaluated every 10 fs, and an average over 20 ps in each direction in an NVE simulation results in the final tensor.

$$\sigma_{ij} = \frac{1}{V}\sum_{k=1}^{N} m^k v_i^k v_j^k + \frac{1}{V}\sum_{k=1}^{N}\sum_{l\neq k}^{N} r_i^{kl} f_j^{kl} \tag{3.22}$$

3.4.3 Thermal conductivity

The thermal conductivity measures the ability of a material to transfer heat via conduction, it is used in Fourier's law of heat conduction (3.23) which relates the heat flux to its thermal gradient.

$$\mathbf{q} = -k\nabla T \tag{3.23}$$

Several methods exist to calculate the thermal conductivity of a material using MD [57, 58, 59, 60, 61], a brief overview is given here, followed by a detailed description of the method used in this work.
The first method worth mentioning is the evaluation of the phonon dispersion spectra, which describes the transfer of momentum and energy through the lattice and can thus be used to evaluate the thermal conductivity. In ceramic materials, such as urania based compounds, the thermal conductivity is mainly caused by the presence of phonons, and their frequency and life time are the main parameters that influence it.
The second method uses the definition of thermal conductivity itself (3.23), by establishing two regions in the simulation box with different constant temperature

and measuring the resulting heat flux. The two regions would remain at constant temperature due to the equilibration with the thermostats and the resulting simulation would converge toward an equilibrium state.
The third method is very similar to the second one, as it is based on the use of Fourier's law. Its application is reversed though, since an initial heat flux is imposed on the system and the MD simulation measures the resulting temperature gradient. This method is not in equilibrium.
The fourth method is based on the reverse non-equilibrium molecular dynamics (rNEMD) algorithm by Muller-Plathe [60], which is based on the third method, *i.e.*, it fixes the heat flux and calculates the resulting temperature gradient, but in this case the kinetic energy is swapped between atoms in two different layers of the simulation box. The main advantage of rNEMD is the rapid convergence of the results.
The fifth and last method proposed here is also the one used in this work. It is based on the Green-Kubo formula, which relates the ensemble average of an auto-correlation function to the property one wants to measure. This method was chosen for being in equilibrium and for not requiring a direction for the heat flux, as the bubble geometry would make it more complex than necessary. Even if it has its advantages, the Green-Kubo method's main disadvantage is its slow convergence, which causes a higher computational cost compared to other methods, especially at low temperatures. In the case of thermal conductivity, the Green-Kubo formula takes the shape shown in equation (3.24), in which the auto-correlation function is the heat flux averaged over the domain of interest.

$$k = \frac{1}{3k_B T^2 V} \int_0^\infty \langle \mathbf{J}(t) \cdot \mathbf{J}(0) \rangle \, dt \tag{3.24}$$

The algorithm implemented using MD solves the integral a certain number of times, giving a result for the thermal conductivity that changes dynamically. The newly formulated thermal conductivity is thus evaluated every step Δt, resulting in a discrete sample as showed in equation (3.25). It is important to keep in mind that the integration boundary t_i is equivalent to $i\Delta t$.

$$k_i = k(i\Delta t) = \frac{1}{3k_B T^2 V} \int_{t_i}^{t_i + t^*} \langle \mathbf{J}(t) \cdot \mathbf{J}(0) \rangle \, dt \tag{3.25}$$

The time range over which the integral is evaluated is t^*, which is not necessarily equivalent to the time spent between each evaluation Δt. If $t^* > \Delta t$ there are some MD steps over which the integral is not evaluated, which is typically a waste of computational time unless those steps are needed for other purposes. If $t^* < \Delta t$ the successive integrations will have some MD steps in common, which is useless as those common steps are not bringing any new information to the second integral. The best way to implement the algorithm is thus to fix $t^* = \Delta t$.

In order for the final value of k to be meaningful, both the convergence of the correlation function over the interval $[t_i, t_i + t^*]$ and the convergence of the complete simulation time need to be investigated. These results are shown in chapter (4.2), to show that both the convergences occur, but it can be anticipated that the value of k is always converged after 400 ps in the NVE ensemble, for every temperature and structure. For this reason the total simulation time was chosen to be 500 ps for all the simulations and the last 100 ps were used to average the value of k over time in order to obtain a more precise value.
The values of t^* was chosen to be 5 ps for the bulk structures and the voids, while a longer time of 20 ps was needed for the correlation function of the structures with the xenon-filled bubble to converge.
It is worth mentioning that the value of each integration step needs to be very low for the evaluation to be precise, due to the correlation function high frequency. In this work the value of $dt = 1$ fs was chosen, much smaller than the time steps used to evaluate the previous properties (10 fs). This increases the computational cost.
At too low and too high temperatures the values of k evaluated with MD methods ought to be imprecise, as they only consider the effect of phonons, which is not the only contribution to the thermal conductivity. In particular, at low temperatures the thermal conductivity is influenced by spin scattering effects, which are caused by the interaction of electron spins. Furthermore, due to quantum effects, at low temperatures the thermal conductivity does not follow the Dulong–Petit law, but the Debye model, which is not reproducible with a classical MD formulation. The difference between the models starts to be non negligible below the Debye temperature, which is 384 K in the case of UO_2 [62].
At high temperatures the contribution of polarons to k becomes important. Fink [63] proposed equations (3.26) and (3.27) for the evaluation of the two contributions to thermal conductivity of UO_2 at 95% theoretical density, the first accounts for the phonons contribution and the second one for polarons.

$$k_{phonons}(T) = \frac{1}{7.5408 \cdot 10^{-2} + 17.692 \cdot 10^{-5} T + 3.6142 \cdot 10^{-8} T^2} \tag{3.26}$$

$$k_{polarons}(T) = \frac{6400}{(T/1000)^{5/2}} \exp\left(-\frac{16350}{T}\right) \tag{3.27}$$

The polarons contribution becomes more and more important by increasing the temperature, table (3.4) summarizes this contribution at some temperatures. While at the lowest temperatures simulated in this work the polarons would not contribute in any way, at the highest temperatures the MD simulations are missing a contribution to the thermal conductivity of 65%. One should thus take into account that the results obtained are only a part of the whole thermal conductivity.

Contribution of polarons [%]	Temperature [K]
0	300
25	2196
50	2688
65	3100
75	3509

Table 3.4: Percentage contribution of polarons on the thermal conductivity of UO_2 at different temperatures. [63]

3.5 Evaluation of the uncertainties

In order to evaluate the uncertainty of every simulated value, in this work the same strategy was adopted: the corrected sample standard deviation was found with equation (3.28) by running the same simulation several times and changing only the initial velocities and the plutonium distribution of the structure.

$$\sigma = \sqrt{\frac{1}{N-1}\sum_{i=1}^{N}(x_i - \bar{x})^2} \tag{3.28}$$

Let x be the property to measure, $\hat{x}$ is its average over multiple simulations and x_i is the single value measured during the i-th simulation. N is the total number of simulations for that specific temperature, structure and property, and it might vary depending on these factors. For the heat capacity, the LTEC and the elastic constants a value of $N = 3$ was enough to have accurate results, but for the evaluation of thermal conductivity at low temperature the number of points needs to be higher as the fluctuation of the results is wider. A summary of the number of points evaluated for each temperature to measure the thermal conductivity can be found in table (3.5). Since for the UO_2 and PuO_2 structures the change in

Temperature [K]	[300,700]	[750,1000]	[1100,2000]	[2200,3100]
Simulations	7	5	3	3

Table 3.5: Number of simulations carried out at different temperatures to evaluate the thermal conductivity, only varying the initial velocities' field and the plutonium distribution.

plutonium distribution has no meaning, for these two cases only the distribution of the initial velocities was changed, leaving the only structure studied with a varying plutonium distribution the $(U_{0.5}Pu_{0.5})O_2$ one.

Chapter 4

Results

4.1 The choice of the simulation box size

In bulk structures, by increasing the number of atoms in the simulation box, the results converge, as the accuracy increases. In structures with a defect such as a bubble, a change in the number of atoms corresponds to a different structure all together, and one should not expect the same results. In the case of a bubble, by changing the super-cell size one decreases the porosity and the bubbles' density.
Nevertheless, a sensibility study to be certain that the number of atoms in the simulations is enough to obtain convincing results is necessary. Bathellier *et al.* [47], found that a super-cell with 2592 atoms (6x6x6) is enough to obtain an uncertainty of $\pm 5 \frac{J}{K-mol}$ on the heat capacity for bulk structures. In this work we confirmed the same minimum size for the bubbles' structure, as showed in figure (4.1), which is referred to a minimized UO_2 structure, with a 25 SDs bubble and 30 xenon atoms.
For this reason it was chosen to run bulk simulations with 12000 atoms (10x10x10) and bubbles structures in a range from 2592 atoms (6x6x6) to 20736 atoms (12x12x12).

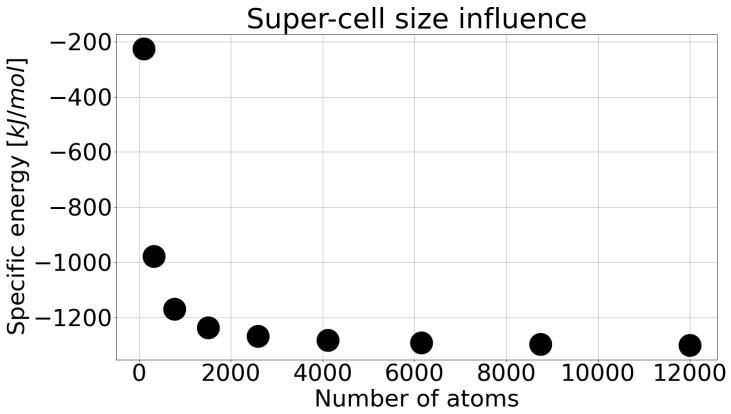

Figure 4.1: Sensibility study of the super-cell size, for the structure with 25 SDs and 30 xenon atoms.

4.2 The choice of the simulation time

In order to find the correct total time for each simulation, a sensibility study was carried out at the beginning of the work. Properties like enthalpy and volume ought to converge by increasing the simulation time, and if the convergence is not reached the results have no meaning.
In the present section, the results of the variance for volume and enthalpy is shown. The variance is evaluated as in equation (3.28), where $N = t/\Delta t$ is the number of points which increases with the simulation time. Δt is the time spent between each evaluation of the desired property, in this work it is set to 10 fs. The number of points over which the average is made is i, looping from one value to N, which means that the average is more and more precise the more the simulation approaches its end. The equation to obtain the standard deviation can thus be rewritten as in (4.1).

$$\sigma(t) = \sqrt{\frac{1}{\frac{t}{\Delta t} - 1} \sum_{i=1}^{\frac{t}{\Delta t}} \left(x_i - \frac{\sum_{j=1}^{i} x_j}{i} \right)^2} \tag{4.1}$$

It is worth noting that a thermalisation time is also present, but only after the thermalisation is over the properties begin to be evaluated, hence this time is not accounted for in the convergence of the properties.
At first, the convergence of enthalpy (4.2) and volume (4.3) in NPT simulations are shown, as they are used for the evaluation of the heat capacity and the LTEC. Using the information obtained from long simulations of 2 ns of different structures in the sensibility study it was decided to run the simulations up to 500 ps, which always give a precision of 5 J/mol for the enthalpy and 10^{-3} nm^3 for the volume, compared to the long ones. At higher temperatures the convergence is slower, while the plutonium content does not have a strong influence on the convergence rate.
While for the specific heat and the LTEC long time periods are needed for the simulations, for the elastic coefficients short time periods such as 10 ps are enough. This was not demonstrated in this work, but it is common in the literature, such as in the work of Cooper *et al.* [64] in which they used 5 ps of averaging time.
The procedure to calculate the thermal conductivity is explained in detail in section (3.4.3), here it is just presented the convergence of the results. In figure (4.4) is presented the correlation function for the bulk UO_2, $(U_{0.5},Pu_{0.5})O_2$ and PuO_2 averaged over 1 ns and evaluated for 20 ps.
The results confirm that at lower temperatures the correlation function converges more slowly, and it was found that the higher is the uranium content, the slower the convergence is. It seems that after 5 ps all curves are converged, and indeed the truncation times t^* were also chosen below or equal to this limit for the bulk in this work. In the figure (4.5) the corresponding integrated correlation functions

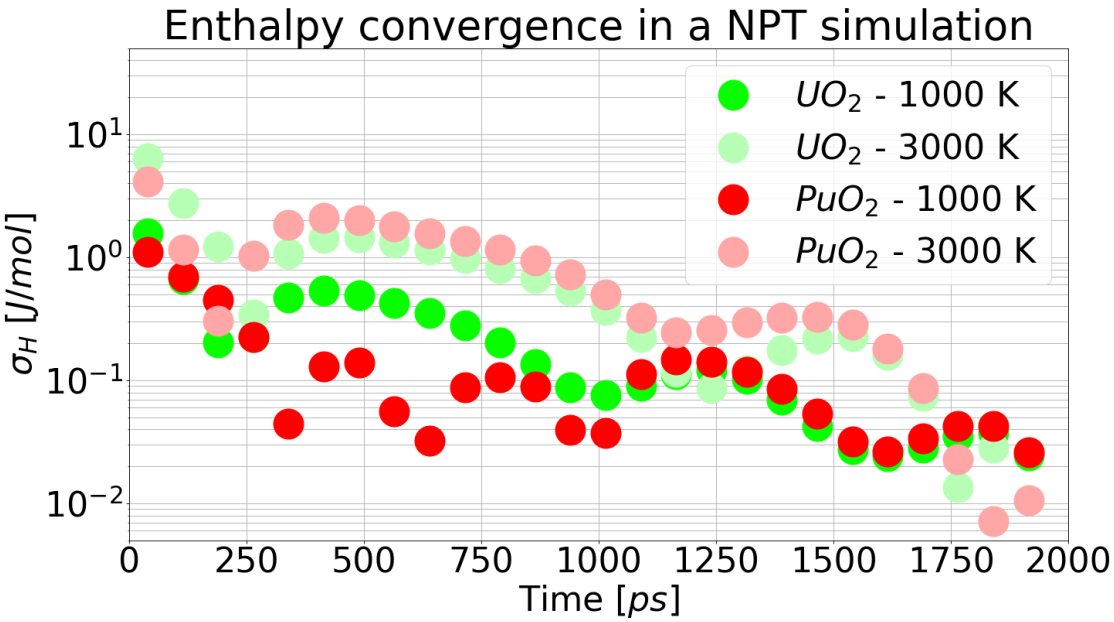

Figure 4.2: Enthalpy convergence during 2 ns of a NPT simulation.

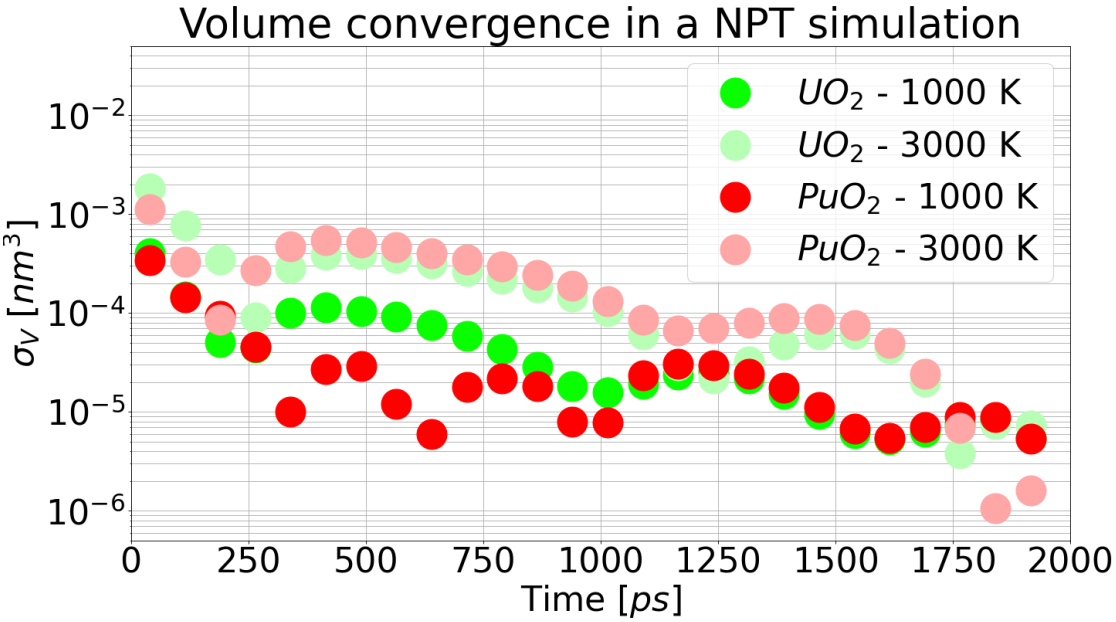

Figure 4.3: Volume convergence during 2 ns of a NPT simulation.

are shown, again for bulk UO_2, $(U_{0.5},Pu_{0.5})O_2$ and PuO_2 and for the same time parameters.
As the integrated correlation function is directly proportional to the phonon

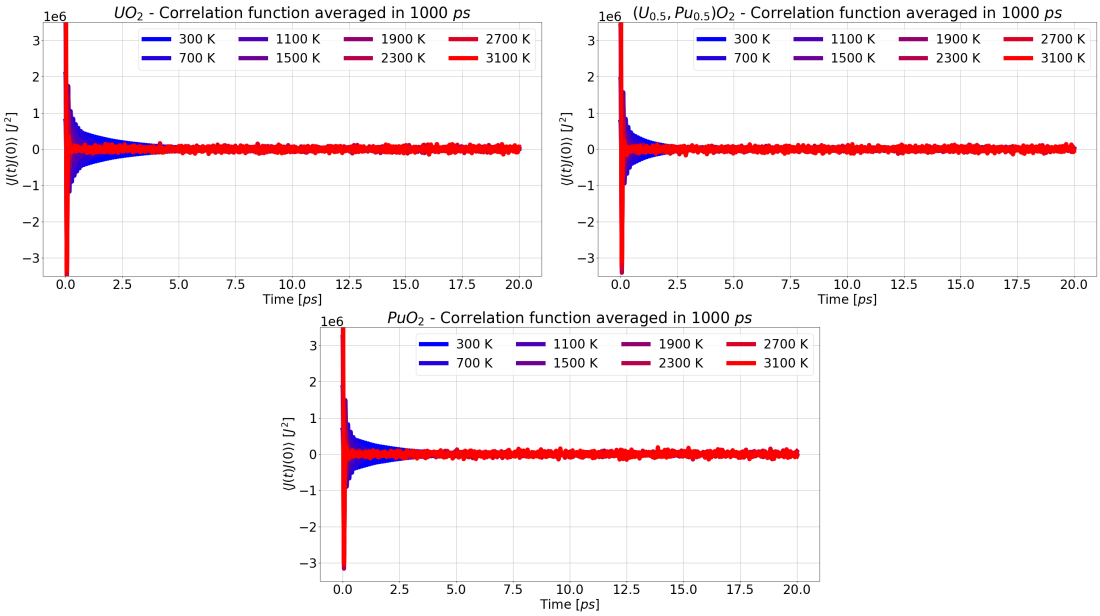

Figure 4.4: The correlation function at different temperatures for three different bulk $(U_{1-y},Pu_y)O_2$ structures.

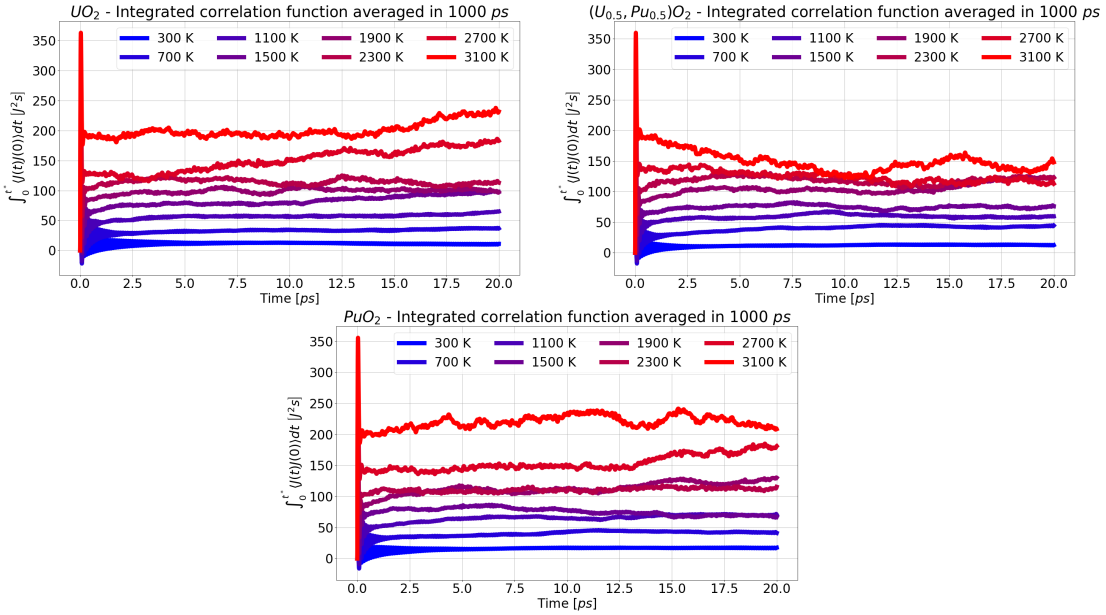

Figure 4.5: The integrated correlation function at different temperatures for three different bulk $(U_{1-y},Pu_y)O_2$ structures.

contribution of the thermal conductivity, which is inversely proportional to the temperature, it is higher when the temperature increases. It can also be seen that by increasing too much the integration time t^* the results are no longer meaningful, as the time is much longer than the phonons' mean life. This phenomenon is more important at higher temperatures, meaning that at different temperatures the value of t^* must be carefully studied in order for the correlation function to converge but also to be meaningful. To conclude, all integration times for the bulk and the voids were chosen between 1 ps and 5 ps, depending on the convergence rate of the specific structure, while for the bubbles a convergence time of 20 ps was deemed necessary.
If the correlation function must converge in each integration time, the thermal conductivity ought to converge during the total simulation time. In figure (4.6) it is shown the convergence of k at different temperatures for the bulk UO_2. Each simulation lasted 500 ps, and the values of the thermal conductivity were obtained averaging k over the last 200 ps.

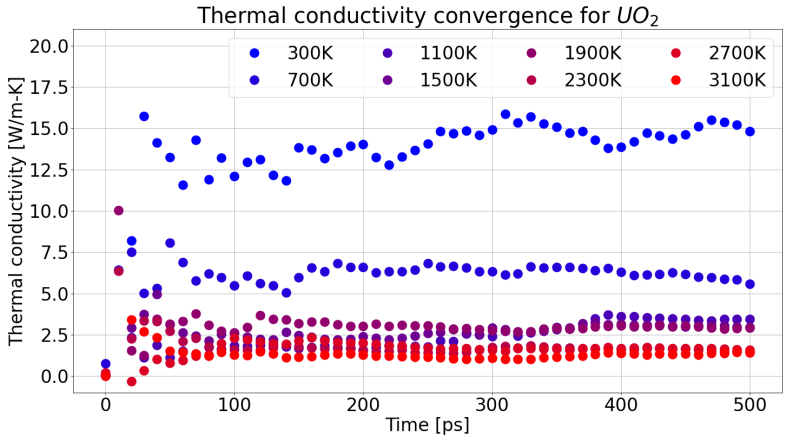

Figure 4.6: Thermal conductivity convergence for UO_2.

4.3 Heat capacity and linear thermal expansion coefficient

In this section, the results of the heat capacity and the LTEC are presented, firstly for each simulated porosity, and then for the obtained fitted law that takes into account the porosity.
In figure (4.7), the heat capacity for the simulated structure is presented, on the left column are shown the empty bubbles, while on the right the xenon-filled bubbles. From the top to the bottom of the picture the porosity increases. The region of 95% confidence values is reported in each figure, but since the uncertainties are very small it is barely noticeable in the pictures.

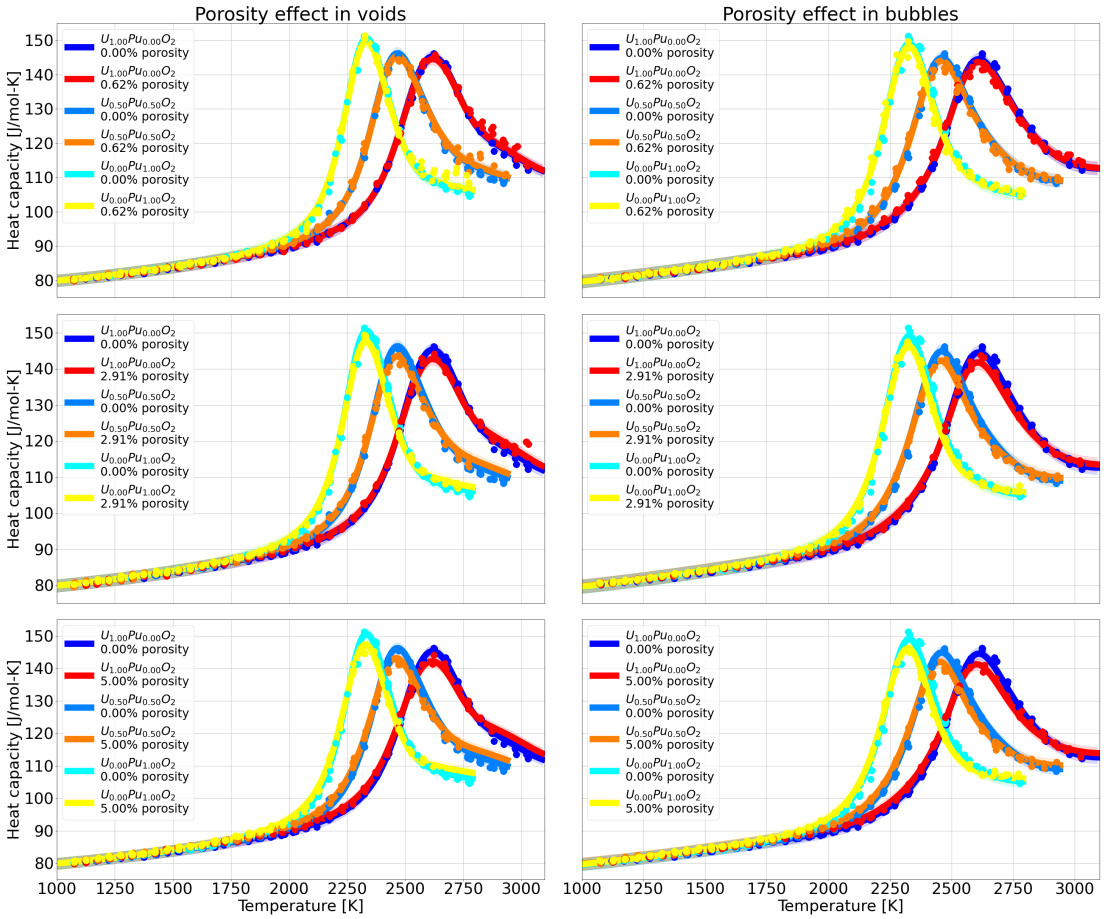

Figure 4.7: The specific heat capacity for the simulated porosities.

The Bredig transition is present in the same conditions reported by Bathellier *et al.* [47], the plutonium content shifts the peak to the left, decreasing the Bredig

temperature. The porosity effect tends to slightly decrease the heat capacity over all, and the effect is more pronounced close to the Bredig temperature. It does not seem like the porosity has any effect on the width of the Bredig peak, while it has a very small effect on the Bredig temperature, which decreases slightly.
The presence of xenon slightly decreases the heat capacity and the voids' results are also different after the Bredig transition, as there is an emission of vacancies which is not present in the case of the bubbles.
The Bredig temperatures are found to be 2610 K for bulk UO_2, and 2330 K for bulk PuO_2, and while the peak decreases with porosity the characteristic temperatures are found to be constant. These values are higher than the approximation $T_B \sim 0.8T_m$ proposed by Browning *et al.* [13], where T_B is the Bredig temperature and T_m the melting point, the reason likely being the very approximated nature of the formula.
Similarly to the specific heat, in this chapter are presented the values of the LTEC obtained for each porosity, they are reported in figure (4.8).
The Bredig transition is clearly visible, just like in the results of the heat capacity. The plutonium and porosity effects are also the same as specific heat. The presence of xenon inside the bubbles slightly increases the value of the LTEC and the results are more easily fitted in the case of the voids: this is the reason why the prediction band is wider in the case of the bubbles.
A law for the evaluation of the specific heat and the LTEC that takes into account the effect of the plutonium content and the porosity is proposed in equation (4.2), where α can be either of the two, by using the appropriate coefficients. The coefficients were fitted with the simulated points and are reported in table (4.1). The law was originally proposed by Bathellier *et al.* [47], without taking into account the porosity effect of nano-bubbles. The expression is composed by three Gaussian functions and three Lorentzian functions, only the latter are modified to take into account the porosity, the former are identical to the work of Bathellier *et al.*.

$$\alpha\left(T,y,P\right) = \left(A + yP_{HL}\right)\prod_{i=1}^{3}\mathcal{L}_i\left(T,y,P\right) + \sum_{i=1}^{2}\mathcal{G}_i\left(T,y\right) + \mathcal{G}_3\left(T\right) + A_0 \tag{4.2}$$

The Gaussian functions $\mathcal{G}_1$ and $\mathcal{G}_2$ are expressed as in equation (4.3).

$$\mathcal{G}_i\left(T,y\right) = \frac{g_i - yP_{HG}}{\sigma_i\sqrt{2\pi}}\exp\left[-\frac{\left(T - \mu_i + yP_{MG}\right)^2}{2\sigma_i^2}\right] \tag{4.3}$$

The Gaussian function $\mathcal{G}_3$ is expressed as in equation (4.4). It is different from the previous two as it accounts for the region before the Bredig transition, and thus does not depend on the plutonium content.

$$\mathcal{G}_3\left(T\right) = \frac{g_3}{\sigma_3\sqrt{2\pi}}\exp\left[-\frac{T^2}{2\sigma_3^2}\right] \tag{4.4}$$

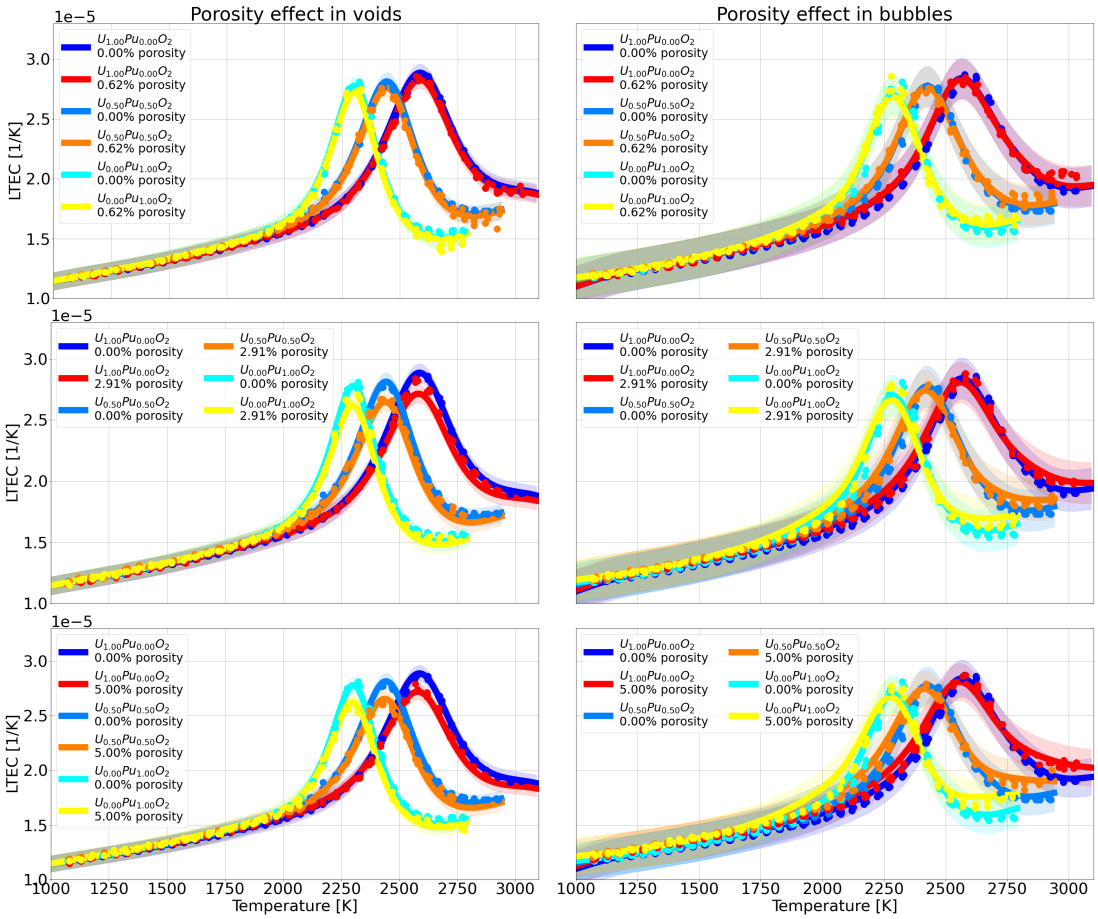

Figure 4.8: The linear thermal expansion coefficient for the simulated porosities.

The three Lorentzian functions $\mathcal{L}_i$ are expressed as in equations (4.5),(4.6) and (4.7), and they take into account the porosity effect.

$$\mathcal{L}_1(T, y, P) = \frac{1}{1 + \left[\frac{T - A_1 + yP_{ML} - \beta_3 P}{B_1}(1 - \beta_1 P)\right]^2} \tag{4.5}$$

$$\mathcal{L}_2(T, y, P) = \frac{1}{1 + \left[\frac{T - A_2 + yP_{ML}}{B_2 - yW_2}(1 - \beta_2 P)\right]^2} \tag{4.6}$$

$$\mathcal{L}_3(T, y) = \frac{1}{1 + \left[\frac{T - A_3 + yP_{ML}}{B_3}\right]^2} \tag{4.7}$$

The newly introduced coefficients β_1, β_2 and β_3 are the ones shifting the curve based on the porosity. In figure (4.9) the general behaviour of the law for the heat

	$c_{p,void}$ [J/mol-K]	$c_{p,bubble}$ [J/mol-K]	α_{void} [1/K]	α_{bubble} [1/K]
A	24115.8 J/mol-K	24473.8 J/mol-K	5.8496E-2 1/K	1.87071E-3 1/K
A_0	4240.81 J/mol-K	4331.44 J/mol-K	-9.22817e-05 1/K	9.00457E-4 1/K
A_1	2955.94 K	2807.21 K	4369.87 K	2862.01 K
A_2	2564.65 K	2555.25 K	2593.31 K	2541.27 K
A_3	-1.56002E6 K	-1.85208E6 K	1923.05 K	1105.14 K
B_1	432.029 K	375.280 K	44.3596 K	310.440 K
B_2	166.062 K	180.349 K	199.637 K	256.722 K
B_3	96496.0 K	98164.6 K	583.284 K	371.145 K
W_2	38.6816 K	43.2802 K	68.9383 K	12.3245 K
σ_1	-98.8910 K	106.771 K	429.547 K	179.720 K
σ_2	-667.465 K	-667.465 K	1492.48 K	237.349 K
σ_3	26442.4 K	-25742.6 K	985.414 K	23395.8 K
μ_1	2527.70 K	2526.42 K	3377.91 K	2412.50 K
μ_2	-9413.31 K	-9413.31 K	2310.35 K	2559.76 K
g_1	1122.02 J/mol	1215.41 J/mol	2.85373E-2	1.07659E-2
g_2	27867.8 J/mol	27867.8 J/mol	0.375233	-3.64859E-2
g_3	-2.75989E8 J/mol	-2.74559E8 J/mol	0.146476	-52.2808
P_{HL}	3105.72 J/mol-K	3366.14 J/mol-K	-3.92451E-3 1/K	-1.84141E-5 1/K
P_{ML}	252.791 K	253.979 K	284.518 K	271.629 K
P_{HG}	156.328 J/mol	301.385 J/mol	-2.85131E-4	1.43965E-4
P_{MG}	2.28380 K	9.63148 K	-0.806960 K	266.160 K
β_1	5.20785	6.16467	4.09785	1.11415
β_2	2.02653	-0.662258	0.690942	0.721271
β_3	3597.20 K	2571.83 K	11722.9 K	383.494 K
RMSE	1.05031 J/mol-K	1.00102 J/mol-K	3.66441E-7 1/K	8.40346E-7 1/K

Table 4.1: List of the fitted parameters for the proposed specific heat and linear thermal expansion coefficient law.

capacity can be seen, for three plutonium concentrations and a porosity ranging from the bulk to 5%. In figure (4.10) the same thing is shown but for the LTEC.

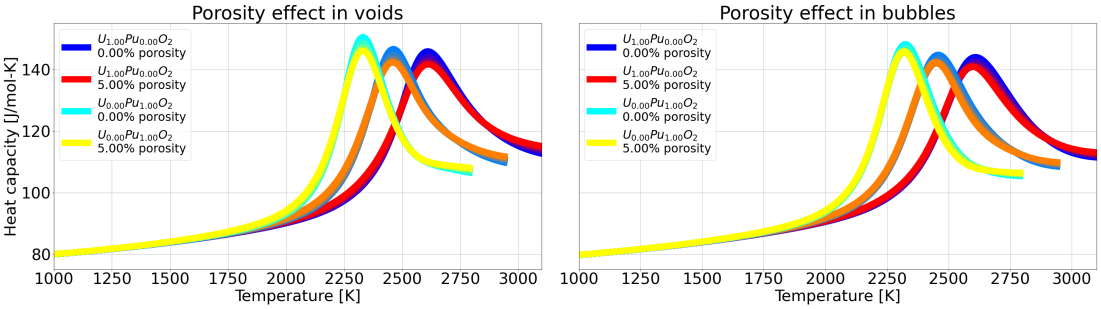

Figure 4.9: Behaviour of the heat capacity proposed law for the voids and the bubbles.

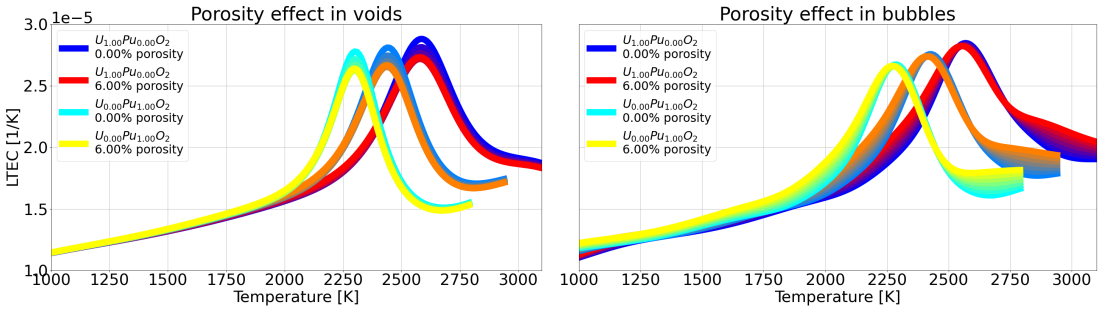

Figure 4.10: Behaviour of the LTEC proposed law for the voids and the bubbles.

4.4 Elastic coefficients

In this section the elastic coefficients obtained are presented. These include C_{11}, C_{12}, C_{44}, the bulk modulus K, the shear modulus G, the Young modulus E and the Poisson coefficient ν.
Firstly, the properties for each simulated porosity are shown, to compare the simulation results with the proposed fitted curve. Each of the property is shown both for the void (on the left) and for the xenon-filled bubble (on the right) and its always compared with the bulk. Furthermore, the prediction band with a probability of 95% for each curve is always reported.
For most of the properties of the voids the prediction band is so small that is impossible to see in the pictures, while for the xenon-filled bubbles it can be seen even if small. A part from this, there is no appreciable difference between the empty and the full bubbles, which translates in similar coefficients for the fitted law as reported in tables (4.2) and (4.3). The Bredig transition can be seen as it changes the slope of the curves, and in some cases it even causes peaks in the properties. These effect occurs earlier for higher plutonium contents and the porosity plays almost no role in the position of the peaks.
The general impact of the porosity, both for voids and xenon-filled bubbles is to decrease the elastic constants. This decrement is supposed to be linear in the fuel performance codes and in this work it was chosen to impose the same condition for the fitted curve. At the same time the porosity effect does not differ from one plutonium content to the other and it is constant at different temperatures. Since the properties generally decrease with the temperature, the porosity effect is more pronounced at lower temperatures.
The change in plutonium content generally impacts the properties less than the porosity, with the important exception of C_{44} and ν, but it is interesting to notice that some of them are higher for UO_2 (C_{44}, G and E) and others for PuO_2 (C_{11}, C_{12}, K and ν). Vegard's law can be applied on the plutonium content effect for all the elastic properties, as their shift is always linear.
In figure (4.18) are shown the elastic properties of a 50% UO_2-PuO_2 mixture, where in the bulk the distribution of the actinides is randomly imposed, while on the surface of the bubble the concentration is imposed to be either pure uranium, pure plutonium or random. The bubble is composed by 25 SDs and 30 xenon atoms. This study was done to confirm that the plutonium distribution on the surface of the bubble does not impact the elastic results, and the outcome confirms the prediction.
Finally, the law to fit each property is reported in equation (4.8). Since the same law applies for all the properties, the symbol Γ is used as a generic reference in the equation, and with the correct coefficients it represents each of the property simulated in this work. From any three of this properties one could find a valid

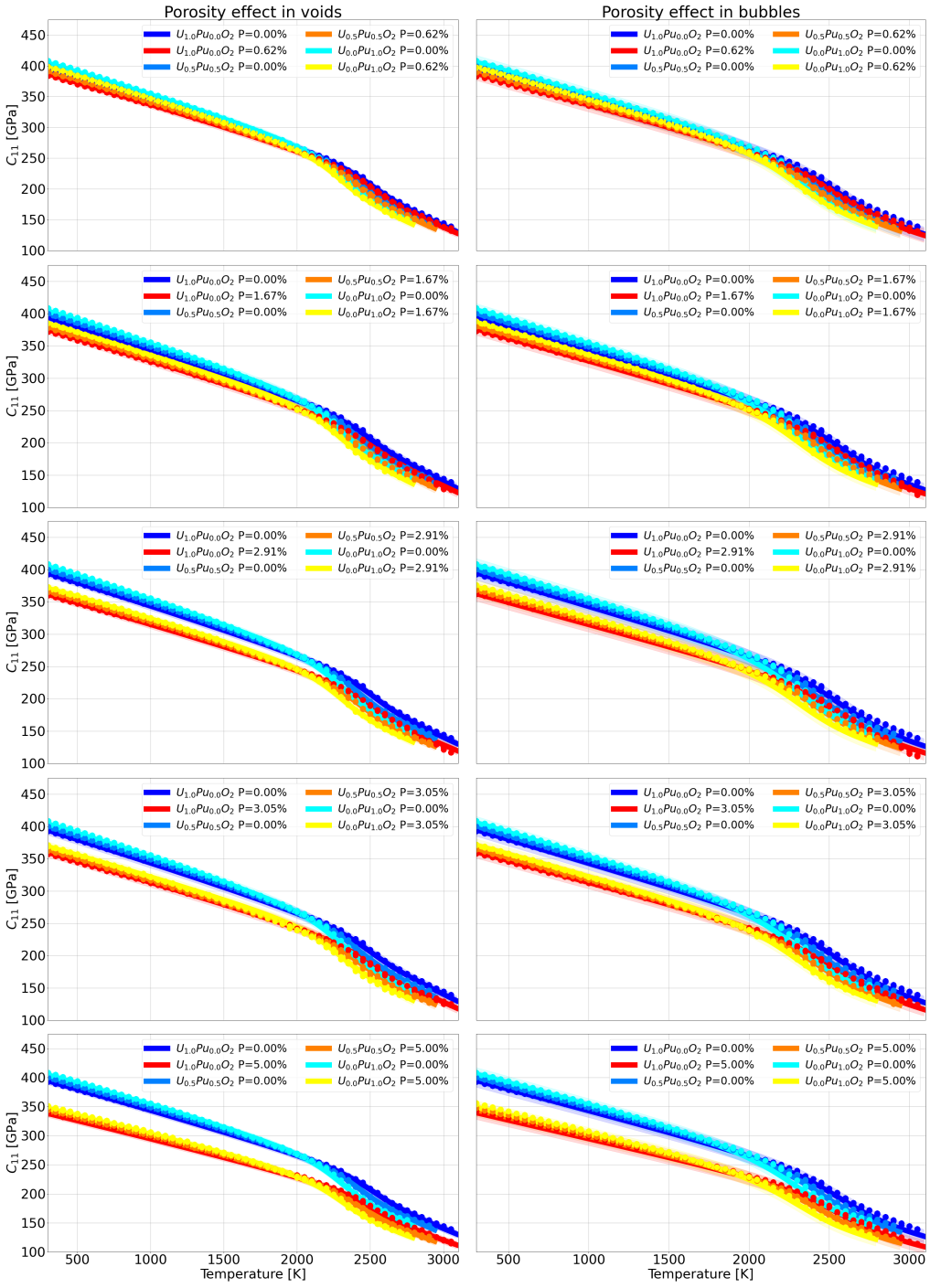

Figure 4.11: The elastic coefficient C_{11} for all the simulated porosities.

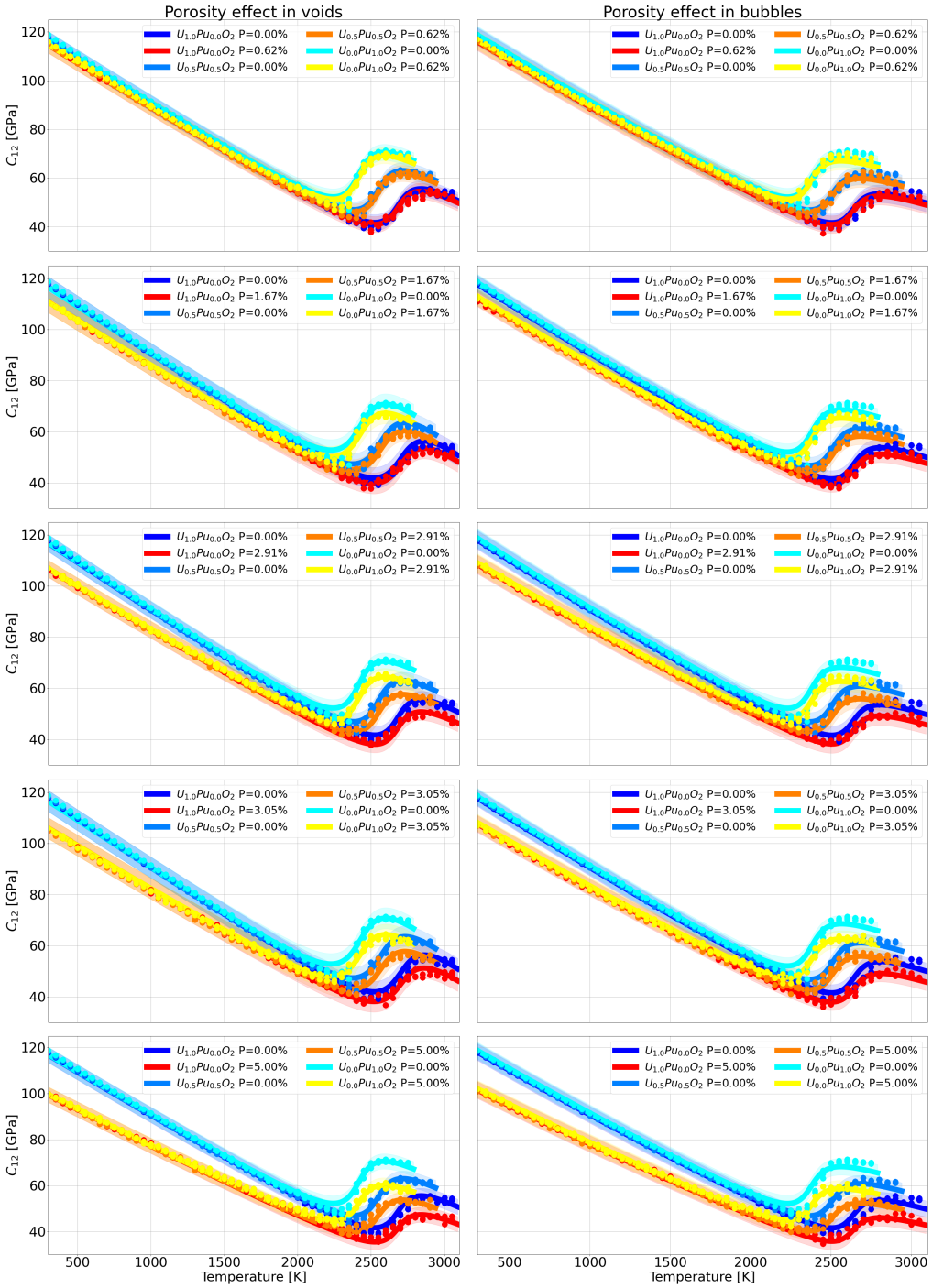

Figure 4.12: The elastic coefficient C_{12} for all the simulated porosities.

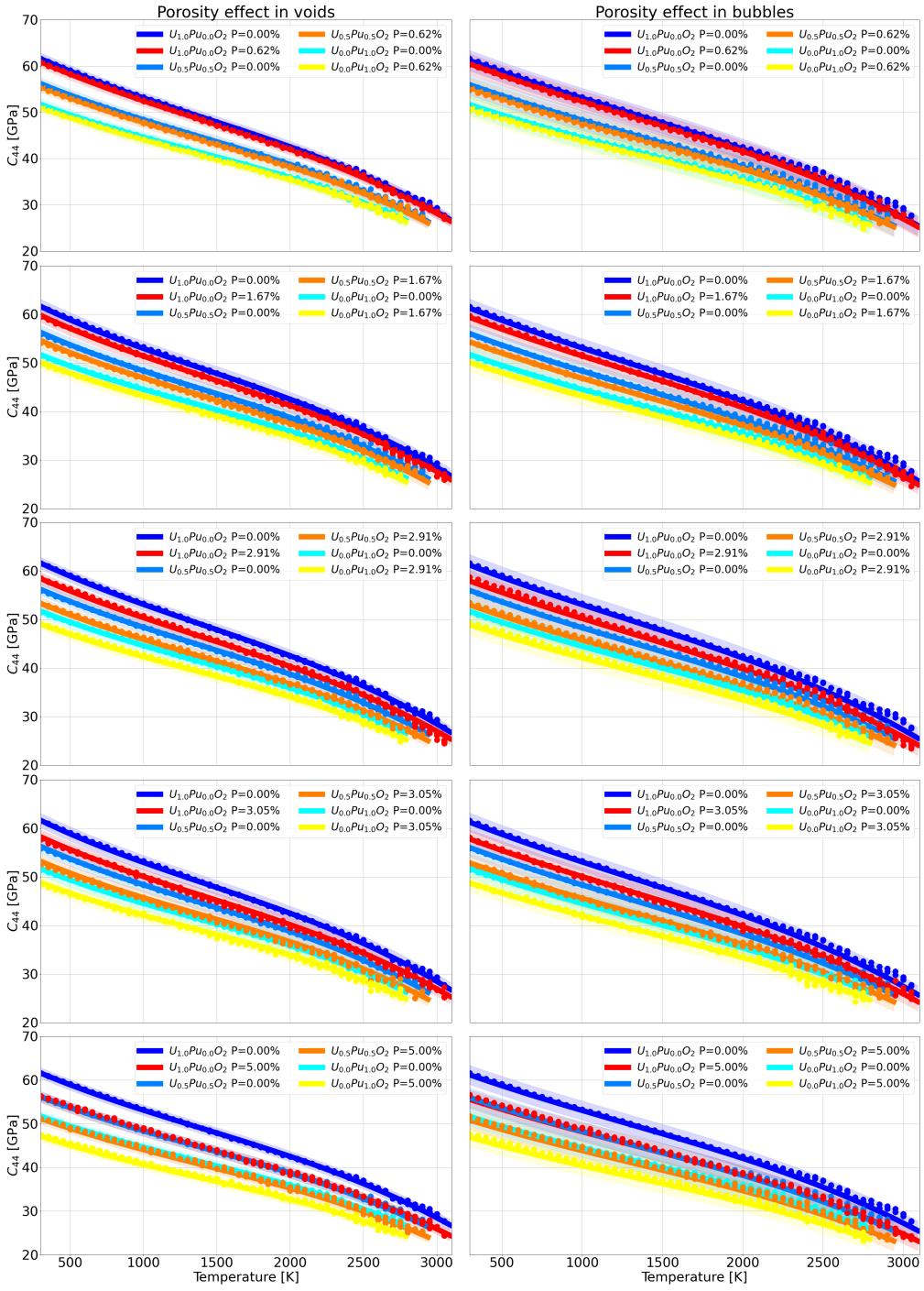

Figure 4.13: The elastic coefficient C_{44} for all the simulated porosities.

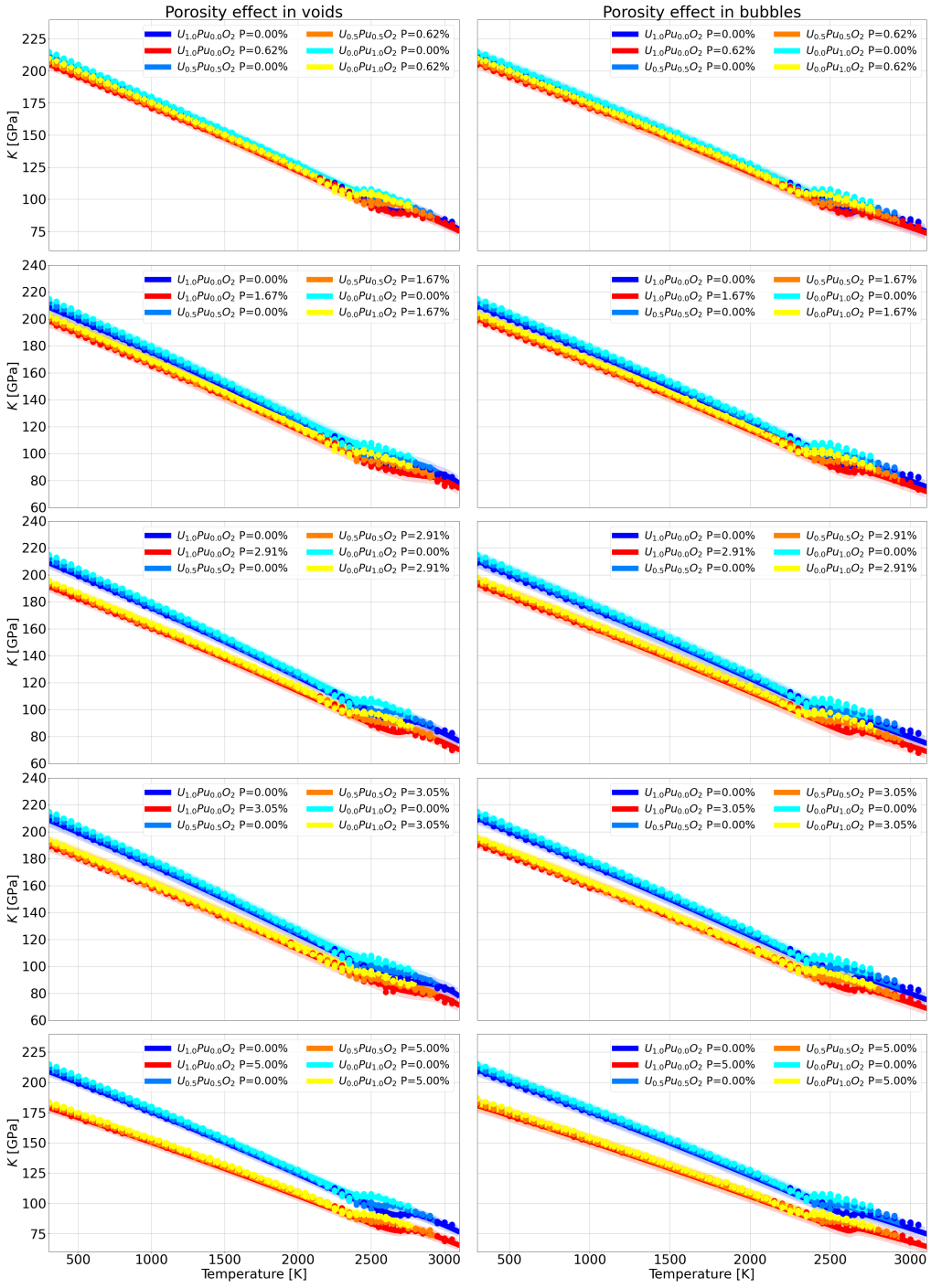

Figure 4.14: The bulk modulus K for all the simulated porosities.

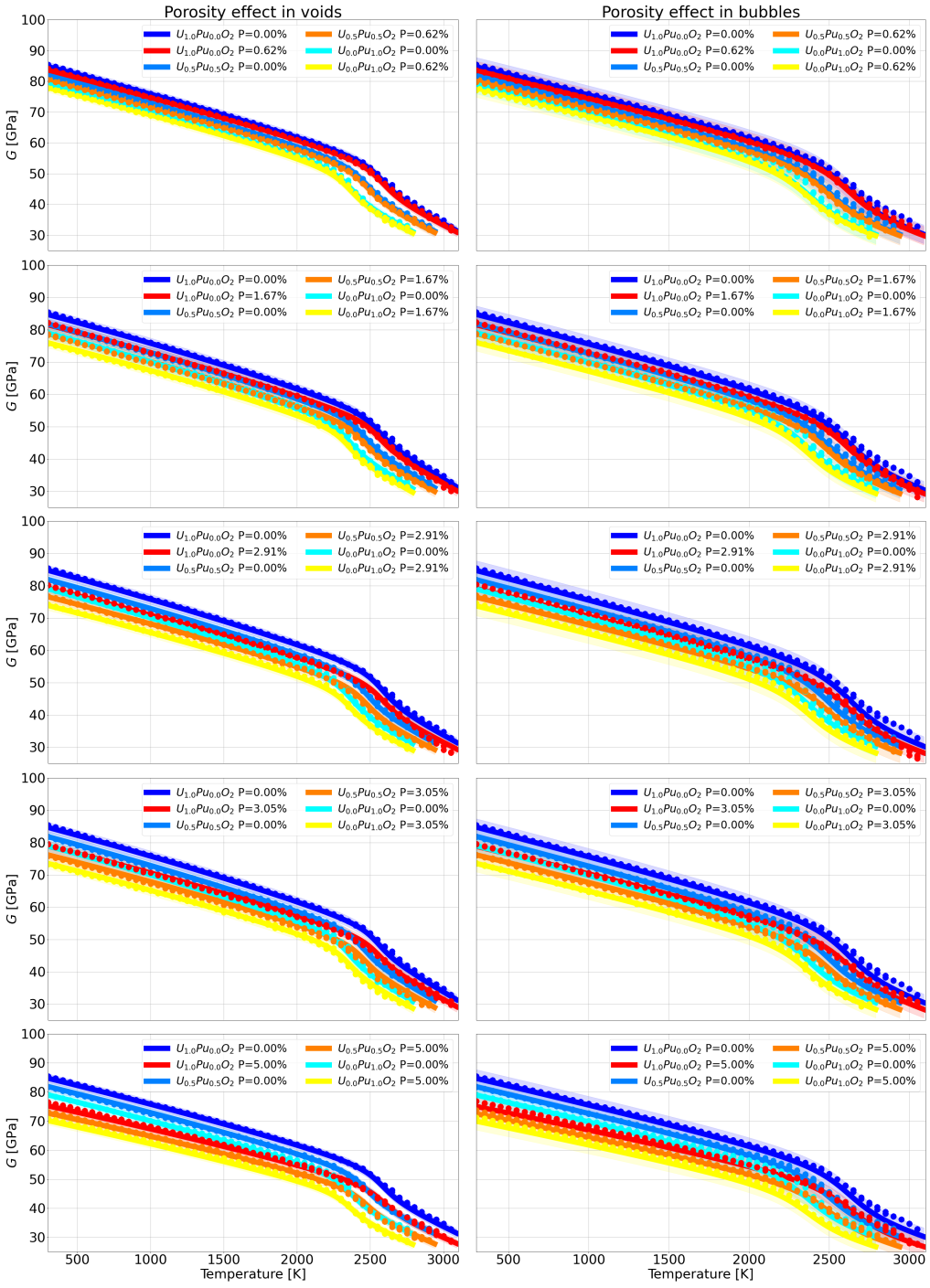

Figure 4.15: The shear modulus G for all the simulated porosities.

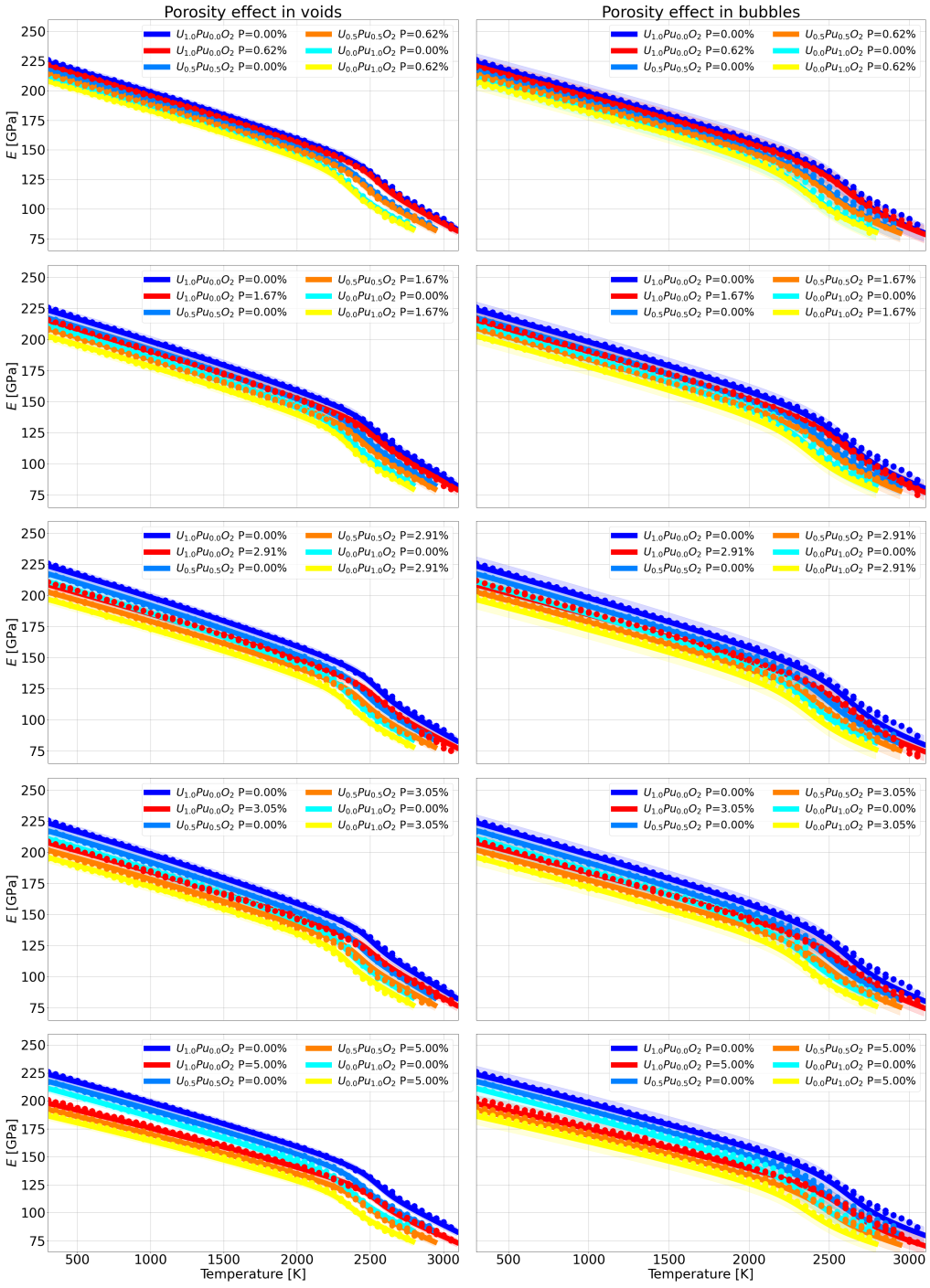

Figure 4.16: The Young modulus E for all the simulated porosities.

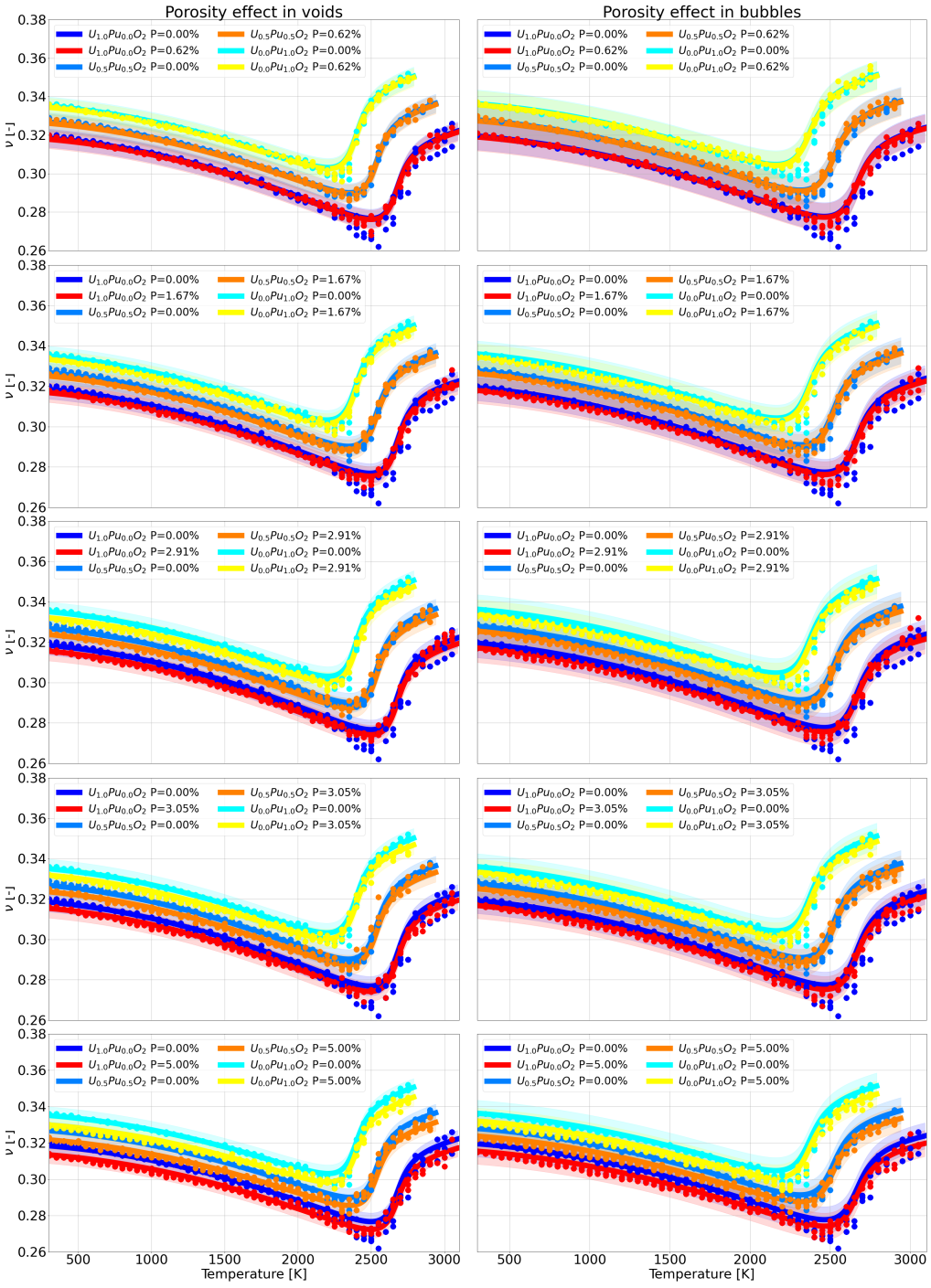

Figure 4.17: The Poisson coefficient ν for all the simulated porosities.

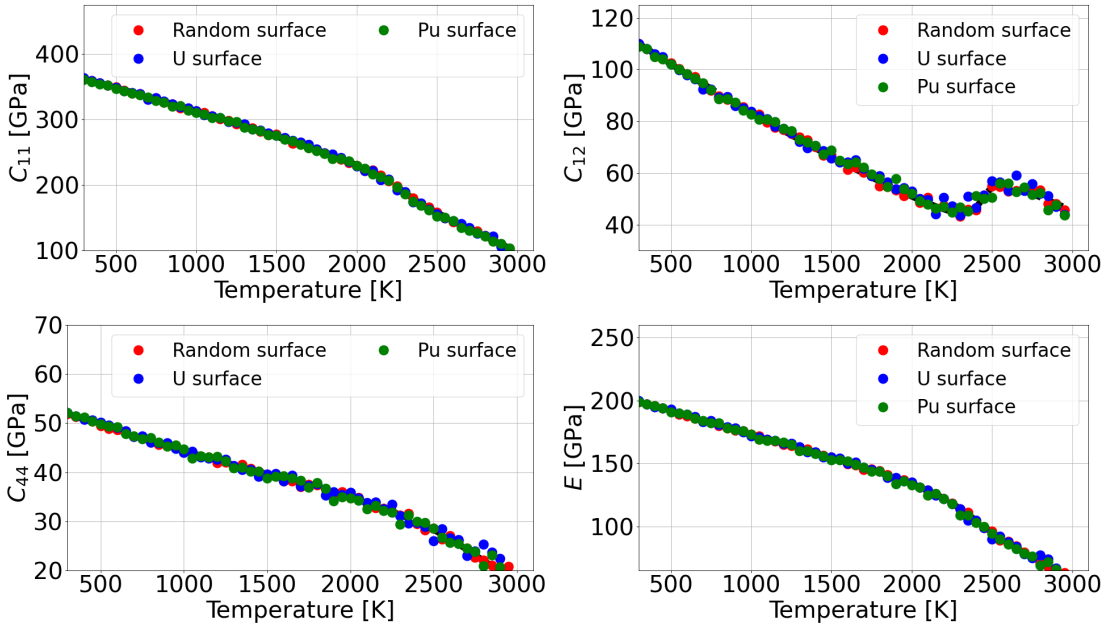

Figure 4.18: C_{11}, C_{12}, C_{44} and the Young modulus for different plutonium distributions on the surface of the bubble.

law for any other property, but we chose to report the fitted parameters for each of them for completeness.

$$\Gamma(T, y, P) = (\Gamma_1(T, y) + \Gamma_2(T, y))(1 - \beta P) \tag{4.8}$$

$$\Gamma_1(T, y) = (aT - b - cy) \arctan\left(\frac{T - d - ey}{s}\right) \tag{4.9}$$

$$\Gamma_2(T, y) = ZT^2 + AT - B - Cy \tag{4.10}$$

The contribution Γ_1 and Γ_2 represent respectively the one for the Bredig transition and the one for the region before the transition.
The coefficients for equations (4.8) can be found in tables (4.2), (4.3), (4.4) and (4.5).

	C_{11}	C_{12}	C_{44}
a [GPa/K]	7.93531E-3	3.67073E-3	1.80292
b [GPa]	4.69938	25.0886	97111.5
c [GPa]	-10.3463	0.832123	895.334
d [K]	2473.52	2706.13	14967.1
e [K]	-195.014	-276.497	169.156
s [K]	-205.978	-122.539	12818.6
Z [GPa/K^2]	-1.44112E-6	3.01758E-7	6.92501E-5
A [GPa/K]	-8.20319E-2	-4.38608E-2	4.74338
B [GPa]	-422.027	-166.230	83699.1
C [GPa]	5.33100	-1.02593	1326.61
β [-]	2.85564	2.97911	1.79525
RMSE [GPa]	3.81960	2.09847	0.753023

Table 4.2: List of the fitted parameters for the proposed simulated elastic coefficients law, for the void.

	C_{11}	C_{12}	C_{44}
a [GPa/K]	-3.34828E-3	-3.03834E-3	-0.280344
b [GPa]	-42.0243	1.92519	7330.75
c [GPa]	-5.89081	2.86701	259.476
d [K]	2578.90	2639.14	14065.6
e [K]	-264.064	-260.847	326.487
s [K]	-311.162	-86.9183	11971.5
Z [GPa/K^2]	1.51404E-6	1.38610E-6	2.34497E-5
A [GPa/K]	-6.81072E-2	-3.61201E-2	-3.63376E-6
B [GPa]	-356.129	-132.829	6280.49
C [GPa]	-3.14982	-4.96866	320.316
β [-]	2.82368	2.81869	1.85341
RMSE [GPa]	5.05801	1.66303	0.969335

Table 4.3: List of the fitted parameters for the proposed simulated elastic coefficients law, for the bubble.

	K	G	E	ν
a [GPa/K] [1/K]	-1.87519E-2	3.00019E-3	7.25937E-3	-1.88386E-5
b [GPa] [-]	-70.0031	4.53282	12.3606	-3.23375E-2
c [GPa] [-]	6.48262	-0.808660	-2.41871	5.13082E-3
d [K] [K]	2907.96	2551.51	2502.61	2674.11
e [K] [K]	-212.564	-202.561	-164.906	-284.185
s [K] [K]	205.754	-106.594	-107.287	-80.7741
Z [GPa/K^2] [1/K^2]	-3.16005E-6	-6.81562E-7	-1.89237E-6	-6.88439E-9
A [1/K]	-7.34128E-2	-1.64520E-2	-4.46148E-2	2.66594E-5
B [GPa] [-]	-327.016	-95.2067	-252.736	-0.270075
C [GPa] [-]	7.55143	6.98996	16.5154	-2.45234E-2
β [-] [-]	2.88599	2.25332	2.33092	0.316265
RMSE [GPa] [-]	2.57119	0.833921	2.18487	2.43928E-3

Table 4.4: List of the fitted parameters for the proposed derived elastic coefficients law, for the void. The first units of measure indicated beside the coefficients are referred to K, G and E, while the second to ν.

	K	G	E	ν
a [GPa/K] [1/K]	4.74129E-3	7.07053E-4	1.13254E-3	-1.95845E-5
b [GPa] [-]	9.95084	-4.08539	-10.6173	-3.36168E-2
c [GPa] [-]	-0.193298	0.255963	0.295709	5.00578E-3
d [K] [K]	2646.54	2618.84	2605.91	2656.03
e [K] [K]	-236.538	-252.699	-240.311	-291.934
s [K] [K]	21.5584	-177.644	-195.144	-87.8990
Z [GPa/K^2] [1/K^2]	-1.98145E-6	-2.35210E-7	-7.42761E-7	-7.04526E-9
A [1/K]	-3.92085E-2	-1.36307E-2	-3.69734E-2	2.75146E-5
B [GPa] [-]	-208.720	-82.4244	-218.808	-0.269139
C [GPa] [-]	-2.75840	5.29812	12.1836	-2.45134E-2
β [-] [-]	2.81614	2.28863	2.35161	0.258095
RMSE [GPa] [-]	2.37502	1.33414	3.31225	3.28862E-3

Table 4.5: List of the fitted parameters for the proposed derived elastic coefficients law, for the bubble. The first units of measure indicated beside the coefficients are referred to K, G and E, while the second to ν.

4.5 Thermal conductivity

In this section the effect of the nano-bubbles porosity on the thermal conductivity of MOX is shown. In figure (4.19) the comparison between the bulk structures simulated in this work and the main references for UO_2 and PuO_2 are confronted. The references are both experimental values and simulated values, in the latter case it is shown a comparison between the Green-Kubo method (EMD) used in this work and the non-equilibrium (NEMD) method, but both computed with the CRG potential.

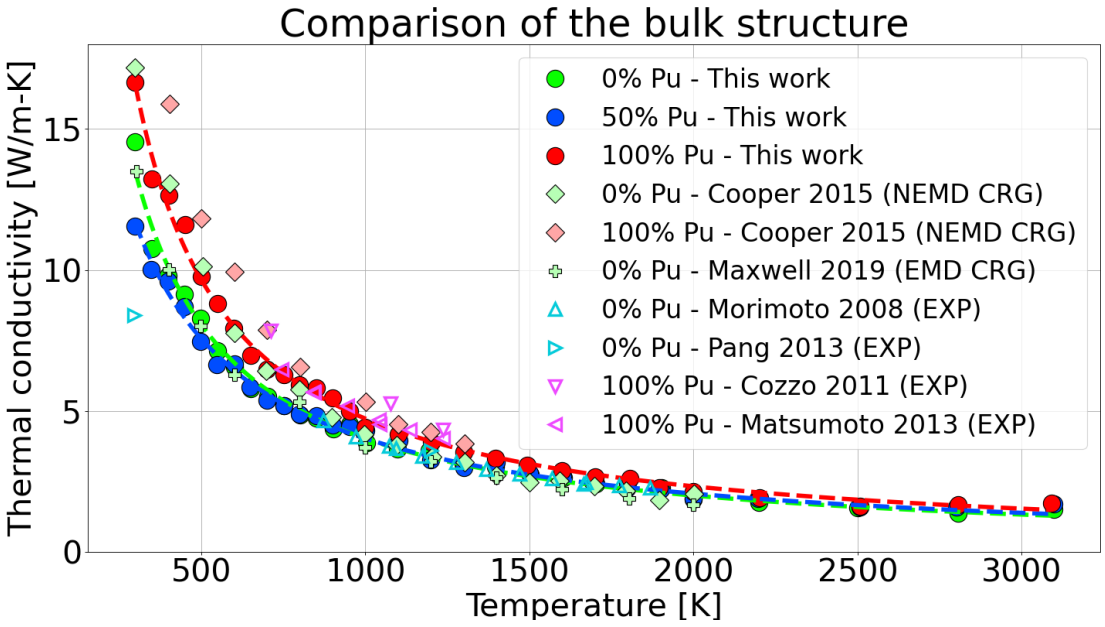

Figure 4.19: Comparison between the thermal conductivity of this work, other works [65, 66], and experimental data [67, 68, 69, 70].

The only study which uses the same method and the same potential is the one by Maxwell *et al.* [66], in green crosses. The results are exactly the same, despite the large fluctuations of the Green-Kubo method.
In figure (4.20), the curves for each simulated porosity are shown, on the left column for voids, on the right column for bubbles, and from top to bottom as porosity increases.
The main takeaway is that, just like all the other properties studied in this work, the thermal conductivity decreases as porosity increases, confirming the results in the literature [71]. The effect of voids seems to be stronger than xenon-filled bubbles, as the drop in k is higher, which is not in line with the results of Zhu *et al.* [55]. The reason for the discrepancy in the results can be due to the different

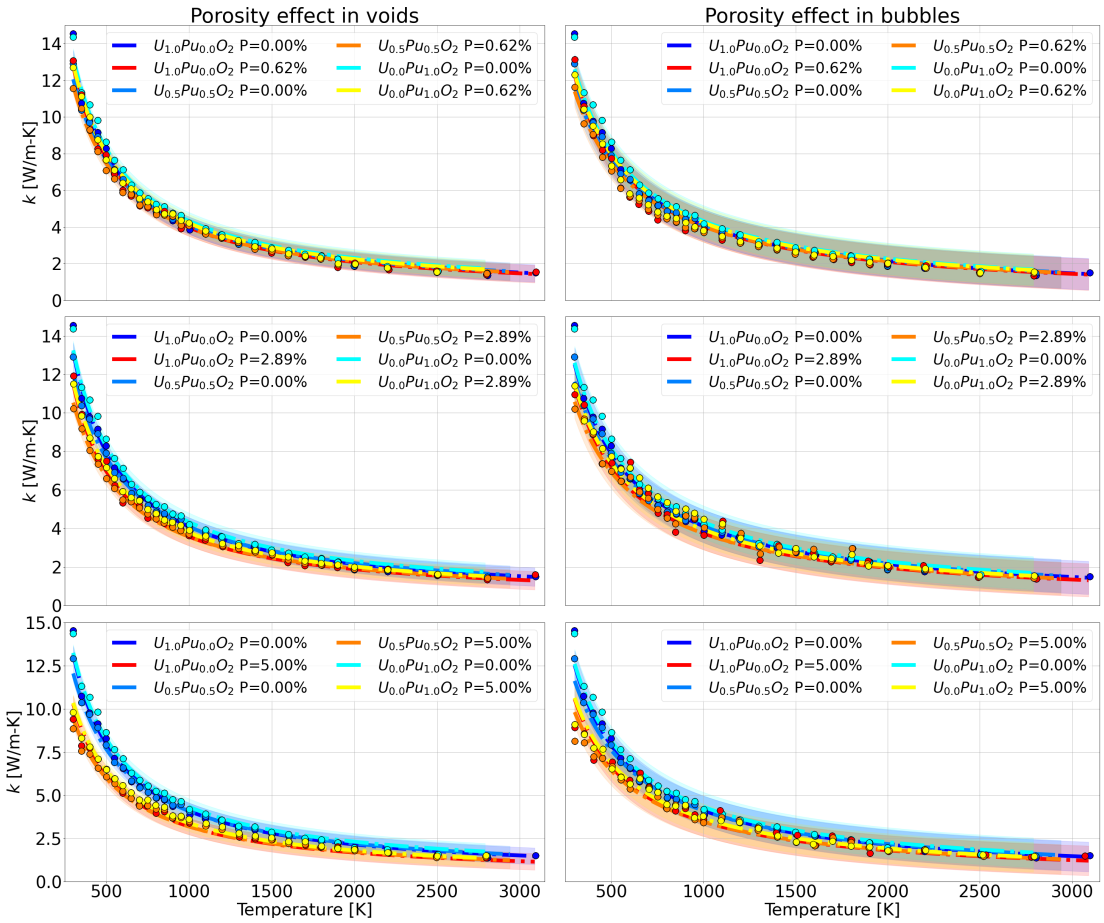

Figure 4.20: The thermal conductivity for all the simulated porosities.

method used, as they adopt the rNEMD algorithm developed by Müller-Plathe [60]. Furthermore, the bubbles results in this work are more scattered than the ones of voids, just like in the simulations for other properties, and this brings a larger uncertainty and a wider confidence range that is shown in the graphs.
The effect of plutonium does not follow Vegard's law, which is supported by the literature [72, 66, 65]. The minimum is supposed to be found close to the 50% U-Pu concentration [65]. This is unsurprising, since the plausible explanation is the U-Pu disorder which decreases the phonons lifetime. For this reason, in this work we decided to study the effect of disorder on (U,Pu)O_2 compounds, to investigate if a random configuration of U and Pu atoms results in different values of k compared to a structure composed by two blocks of pure UO_2 and pure PuO_2. Of course, in MD simulations the periodic boundary conditions transform the system in a periodic distribution of ordered parallelepipeds.
The MD initial ordered super-cell can be seen in figure (4.21): it is composed by

12000 atoms, 8000 of which are oxygen, 2000 are uranium (on the left) and 2000 are plutonium (on the right). The resulting thermal conductivity can be seen in figure (4.22).

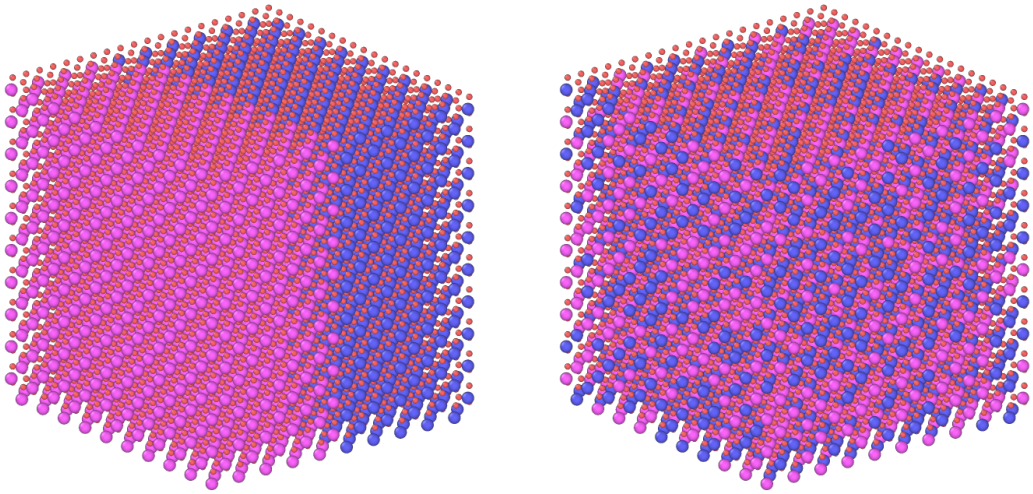

Figure 4.21: The structures used to investigate the effect of disorder on the MOX thermal conductivity. The oxygen particles are in red, the plutonium in purple and the uranium in blue. On the left the ordered structure, on the right the disordered one.

It can be seen that indeed the order impacts on the thermal conductivity, and a more ordered structure like the one investigated brings the thermal conductivity of $(U_{0.5},Pu_{0.5})O_2$ much closed to Vegard's law.
With the obtained data from the simulations, a law was fitted to consider the porosity effect on the thermal conductivity. The law is reported in equation (4.11), and the fitted parameters for the voids and bubbles are reported in table (4.6).

$$k\left(T,y,P\right)=\frac{k_0}{1+A\left(T-300\text{ K}\right)+By^2+Cy}\left(1-\beta P\right) \tag{4.11}$$

In the law, T is the temperature, y is the Pu content, P is the porosity. k_0 is the thermal conductivity of bulk UO_2 at 300 K, A accounts for the decrease due to the temperature increase, B and C account for the Pu effect, which is not linear. Finally, β accounts for the decrease due to the porosity.

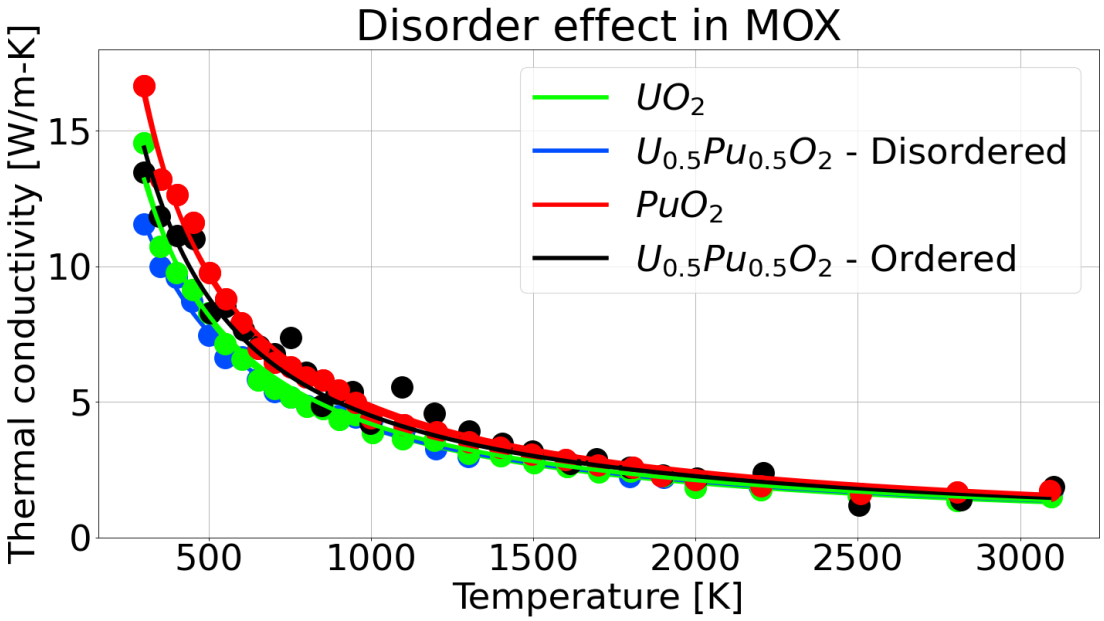

Figure 4.22: The effect of disorder in MOX thermal conductivity.

	k_{void} [W/m-K]	k_{bubble} [W/m-K]
k_0 [W/m-K]	12.852	12.306
A [1/K]	2.940E-3	2.751E-3
B [-]	-0.371	-0.317
C [-]	0.337	0.286
β [-]	4.377	3.105
RMSE [W/m-K]	0.256	0.436

Table 4.6: List of the fitted parameters for the proposed thermal conductivity law.

4.6 Lattice parameters

The lattice parameter, sometimes also called lattice constant, determines the equilibrium distance between the atoms in a lattice. In the MOX fluorite structure the lattice parameter is the distance between the metal atoms.
In MD simulations where the volume is not fixed, *e.g.*, using the NPT ensemble, the lattice parameter is simply related to the volume itself, as the number of atoms per edge is fixed. On the other hand, in simulations where the volume is fixed, like with NVE ensembles, one should be careful to impose the correct lattice parameter from the start, as it won't be able to equilibrate itself during the simulation.
Since the lattice parameter is directly linked to the volume, it is also a thermodynamic property which is dependent on the temperature and the pressure of the system. For this reason, in the following results, in figure (4.23), the lattice parameters are not only showed for different structures and plutonium content, but also as a function of temperature.

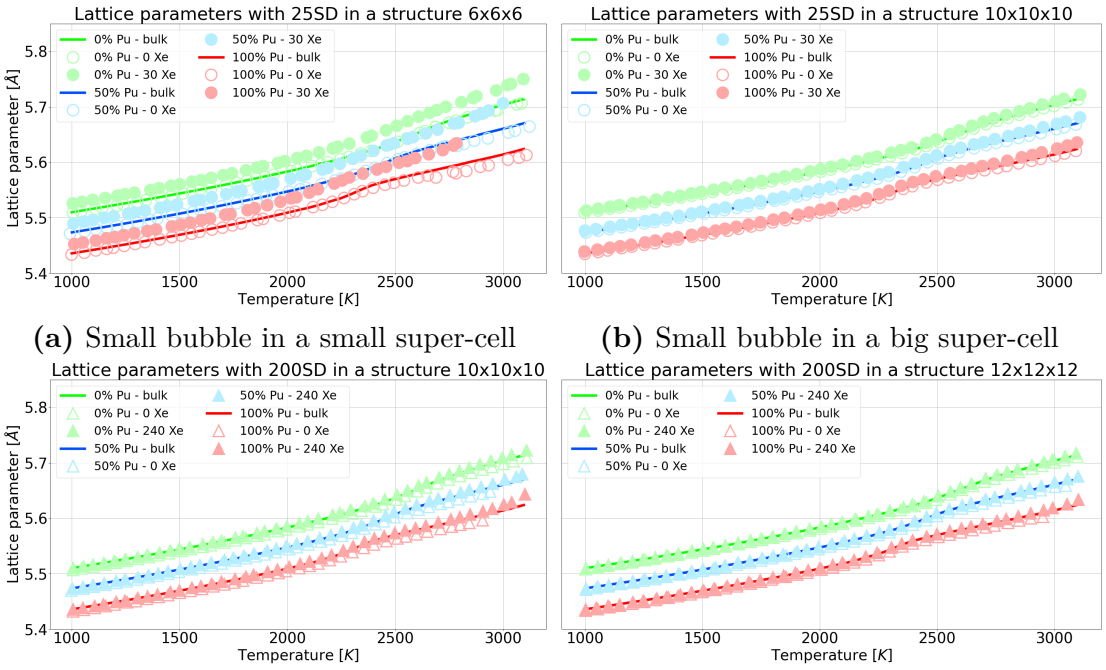

(a) Small bubble in a small super-cell

(b) Small bubble in a big super-cell

(c) Big bubble in a small super-cell

(d) Big bubble in a big super-cell

Figure 4.23: The lattice parameters of the structures with a bubble, compared with the bulk.

The results obtained for the bubbles are always compared with the bulk's, which were calculated for a 10x10x10 super-cell (12000 atoms).
In the results, it can be seen the Bredig transition [14] changing the slope of the

profile. The Bredig temperature shifts on the left for higher plutonium contents. It can also be seen that the lattice parameter is higher for lower plutonium content, which confirms the results of previous studies [49, 73].
The effect of the empty bubbles is to slightly decrease the lattice parameter, and, even if this effect is very small, it is somewhat higher for the larger bubble. The filled bubble has the opposite effect: it increases the lattice parameter. This result is more important at higher temperatures and especially with a higher concentration of bubbles.
For the smaller bubble, *i.e.*, a higher bubbles' concentration, the filled bubble at higher temperatures melts earlier than the bulk. This is a MD effect, as these simulations are not built to efficiently simulate the melting point and other methods, such as the moving interface, should be used instead. Nevertheless, this is the reason why the results where truncated earlier for the filled bubble.
On the other hand, for the voids, the reason of the earlier truncation is that they are not stable, as discussed in section (2.2.6), and at high temperatures they quickly dissolve emitting vacancies and beginning to return results that hold no meaning.

4.7 Initial behaviour of the NPT simulations

As explained in the section concerning MD, the NPT ensemble equilibrates the structure at a certain temperature and pressure using a thermostat and a barostat. The volume in a NPT simulation is thus free to change, and it naturally adjusts itself depending on the imposed thermodynamical conditions.
At the beginning of every simulation the structure is not yet thermalized, which means that the position and the velocities of the atoms are not the ones that they would have if the system was in equilibrium at the desired temperature. In this work the initial structures are either perfect lattices or, in the case of bubbles filled with xenon, are thermalized at 100 K, since this is the temperature at which the xenon was inserted.
It can be useful to study the evolution of the system during the first time steps of the thermalisation, in order to see how quickly the properties converge, how widely they fluctuate and what is the impact of the temperature.
In figure (4.24) there is an example of such study, the picture shows the evolution of the volume of a structure with 50% uranium and 50% plutonium, in a cell with six atoms per edge, with 25 Schottky defects and 30 xenon atoms.

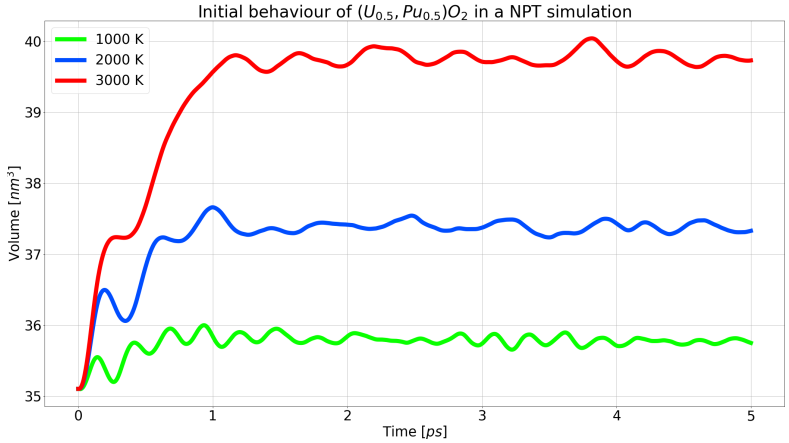

Figure 4.24: Initial evolution of the volume in a NPT thermalisation.

Since the structure is a filled bubble, the initial temperature is 100 K, this influences the initial volume. The pictures shows the first 5 ps of a NPT thermalisation with $T_{damp} = 0.1$ fs and $p_{damp} = 1$ fs.
It can be seen that the volume quickly reaches the imposed conditions, with these values of T_{damp} and p_{damp} it only takes around 1 ps. The fluctuations are bigger at higher temperatures, as it is to be expected because of the nature of the thermostat.

4.8 Radial distribution functions

The radial distribution function, also referred to as RDF, is a dimensionless function describing the distance of particles that are part of a wider system. It can be interpreted as an indicator of the probability to find a particle at a certain distance of any other particle inside the system. The RDFs can be useful to have an idea of the physical state of the system, its internal energy and pressure. Furthermore, RDFs are obtainable also with neutron scattering and X-ray scattering measurements, which is a useful and direct connection between simulations and experiments [74]. The relationship between experiments and RDFs uses the structure factor and the integrated RDF.
The RDF is defined as showed in equation (4.12), where ρ is the density of particles.

$$g(r) = \frac{\langle \rho(r) \rangle}{\rho} \tag{4.12}$$

In a lattice the RDF starts at zero, oscillates with a peak for each stable position at a certain distance from the reference particle, and converges to one as the distance increases to a value much bigger than the lattice parameter. A higher temperature lowers and broadens the peaks, as the particles oscillate more widely around their stable position. A perfect crystal displays a RDF with single point peaks, as the atoms are completely fixed.
While for solids the curve reaches a null value between the peaks, this does not happen if the system is liquid. For solids, the position of particles is fixed and they can only vibrate around their equilibrium position. For liquids, the particles can move around, thus resulting in a not null possibility of finding an atom at any distance of a reference point. Even if the RDF is always positive for liquids, there are still fluctuations in the curve, but this is not true for gaseous systems, in which after the first peak the curve just converges directly to one. In defectless simple cubic solids the radial positions of the peaks are found at the specific values $\sqrt{n}\sigma$, where n is a positive integer and σ is the lattice parameter. For fluorite structures such as urania it is slightly different because of the FCC nature of the uranium sub-lattice.
From $g(r)$ it is possible to calculate the probability to find a particle at a distance r in the neighbourhood dr by using equation (4.13).

$$P(r) = 4\pi r^2 g(r)\, dr \tag{4.13}$$

In the following pages, the results of the calculated RDFs are shown, both for bulk structures and the bubbles. The effect of the plutonium concentration, as well as the temperature, can be studied.
In the first figure (4.25), the RDFs of a bulk structure of PuO_2 are shown, while

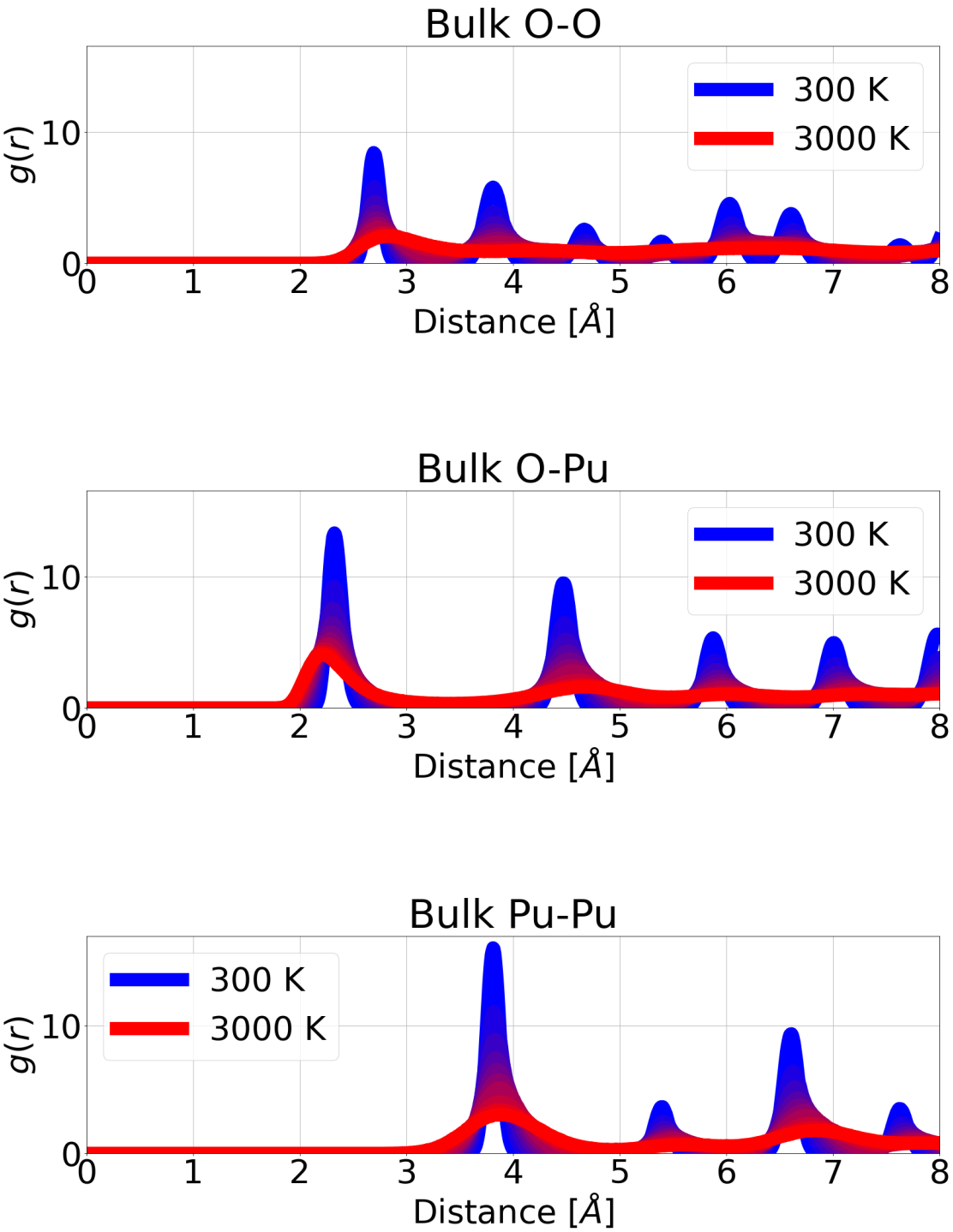

Figure 4.25: The radial distribution functions of a bulk PuO_2 structure.

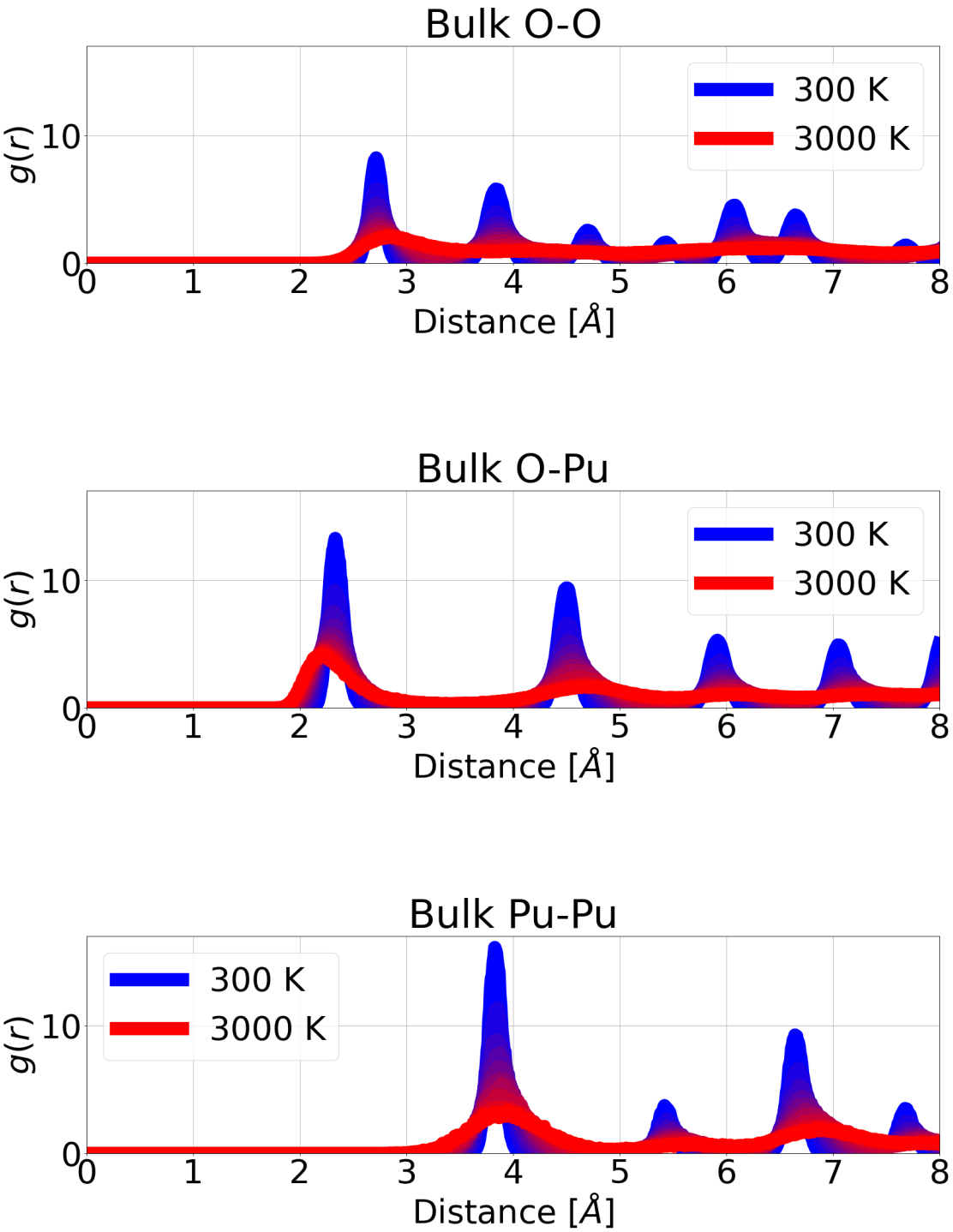

Figure 4.26: The radial distribution functions of a bulk $(U_{0.5},Pu_{0.5})O_2$ structure.

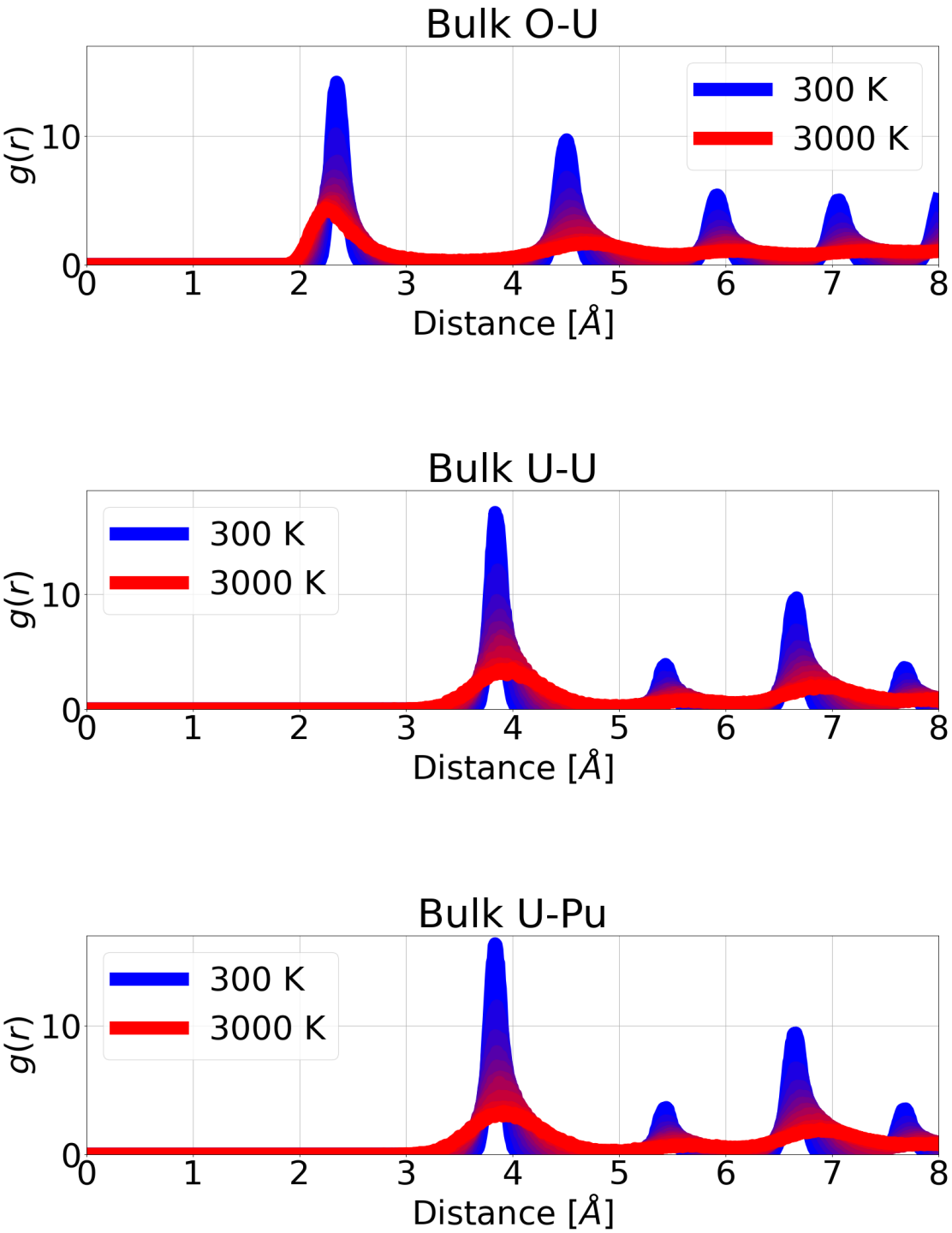

Figure 4.27: The radial distribution functions of a bulk $(U_{0.5},Pu_{0.5})O_2$ structure.

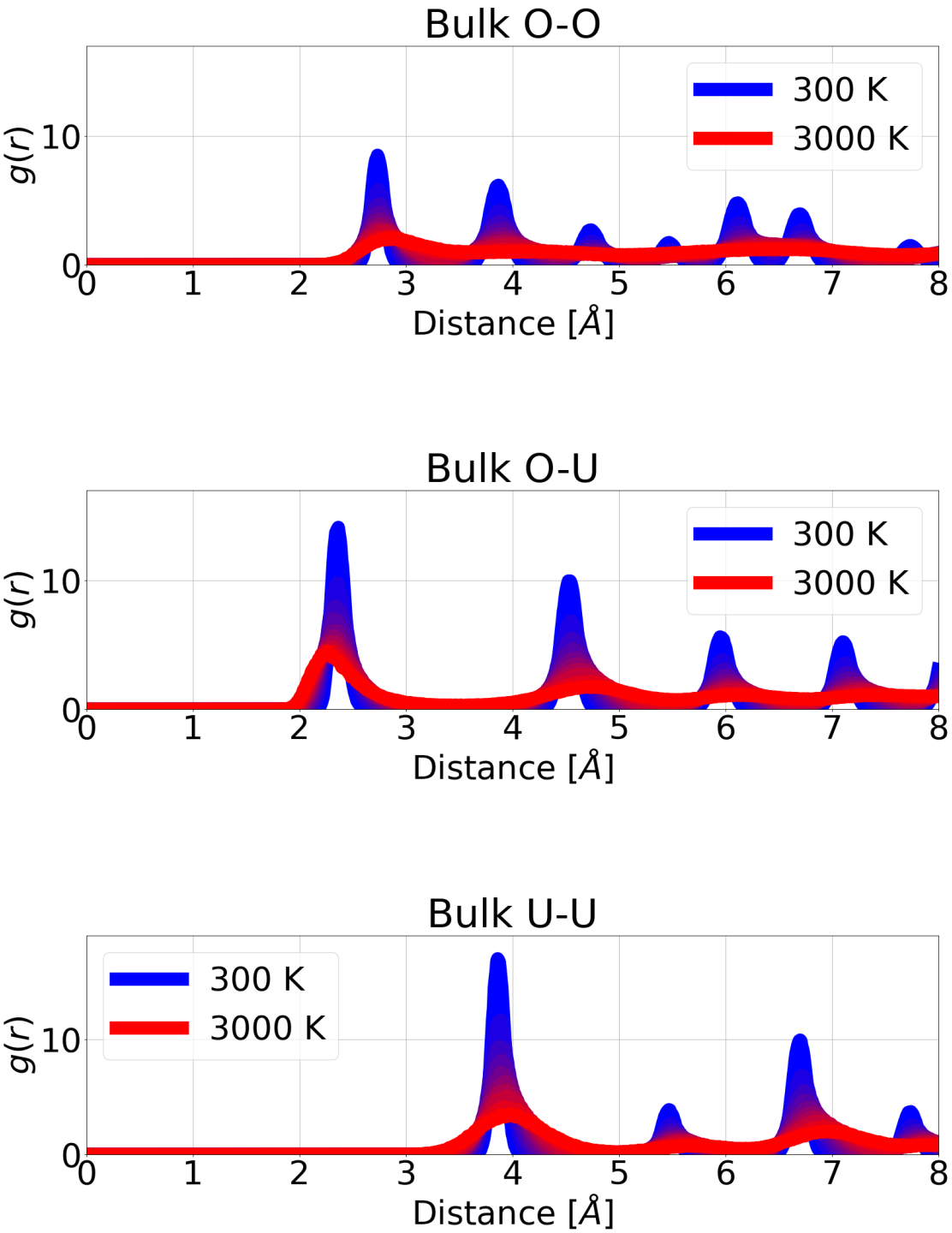

Figure 4.28: The radial distribution functions of a bulk UO_2 structure.

the second one (4.26) and the third one (4.27) show the 50% mixture of UO_2 and PuO_2 and the fourth one (4.28) pure UO_2.
The behaviour of the oxygen-oxygen relationship is the same for each of the three structures, with seven peaks below 8 Å. The same thing can be said for the relationship between oxygen-uranium and oxygen-plutonium, since uranium and plutonium atoms occupy the same lattice positions, and again for uranium-uranium, uranium-plutonium and plutonium-plutonium for the same reason. As expected the influence of an increase in temperature is to lower and broaden the peaks, in some cases almost to a constant value.
At 3000 K the oxygen-oxygen curve does not fall to a null value between the peaks, indicating a melting of the sub-lattice that confirms the prediction of the Bredig transition. The same thing cannot be said for the other relationships, indicating that the materials are not fully melted at 3000 K.
The presence of a void is explored in figure (4.29), the difference in the RDFs is minimal. One can expect that the presence of the void would broaden the peaks as the atoms on the surface would feel the lack of neighbors, but the relative quantity of surface atoms compared to the total amount is negligible and no effect can thus be observed.
If xenon is inserted in the void, the RDFs remain indistinguishable from the bulk, but the curves of xenon can be studied, as showed in figure (4.30) and (4.31). In the first one only 30 xenon atoms in 25 Schottky defects are present, while in the second one there are 240 xenon atoms in 200 Schottky defects, resulting in smoother curves but inherently different results, as they correspond to different systems. The biggest difference can be seen in the xenon-xenon curves, where the peak is much higher and steeper for the small bubble, since all the xenon atoms are trapped in a much smaller region, while for the bigger bubble they are free to move in a bigger space. The RDFs of oxygen-xenon and uranium-xenon are good tools to understand the surface behavior, indicating for example the minimum distance at which the xenon atoms are positioned to the bulk atoms, as well as their preferential distance for close interactions, *i.e.*, the first peak. For the smaller bubble not only the values of the xenon-xenon $g(r)$ curve are higher, but also the values of oxygen-xenon and uranium-xenon, since many more xenon atoms occupy surface positions, while in the bigger bubble many xenon atoms are distant to the bulk as they are not on the surface.

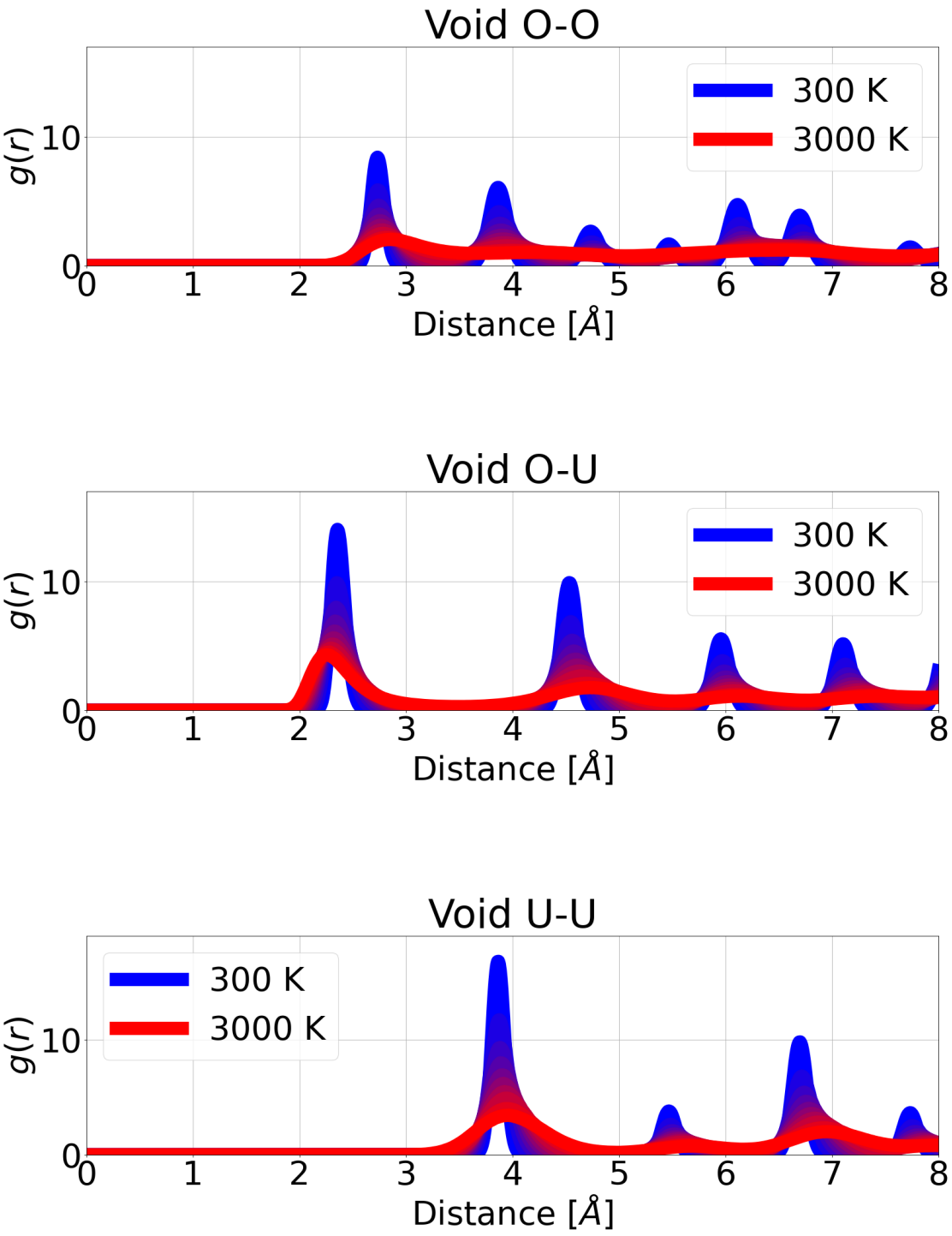

Figure 4.29: The radial distribution functions of a UO_2 structure with a cubic distribution of spherical voids of 25 Schottky defects each.

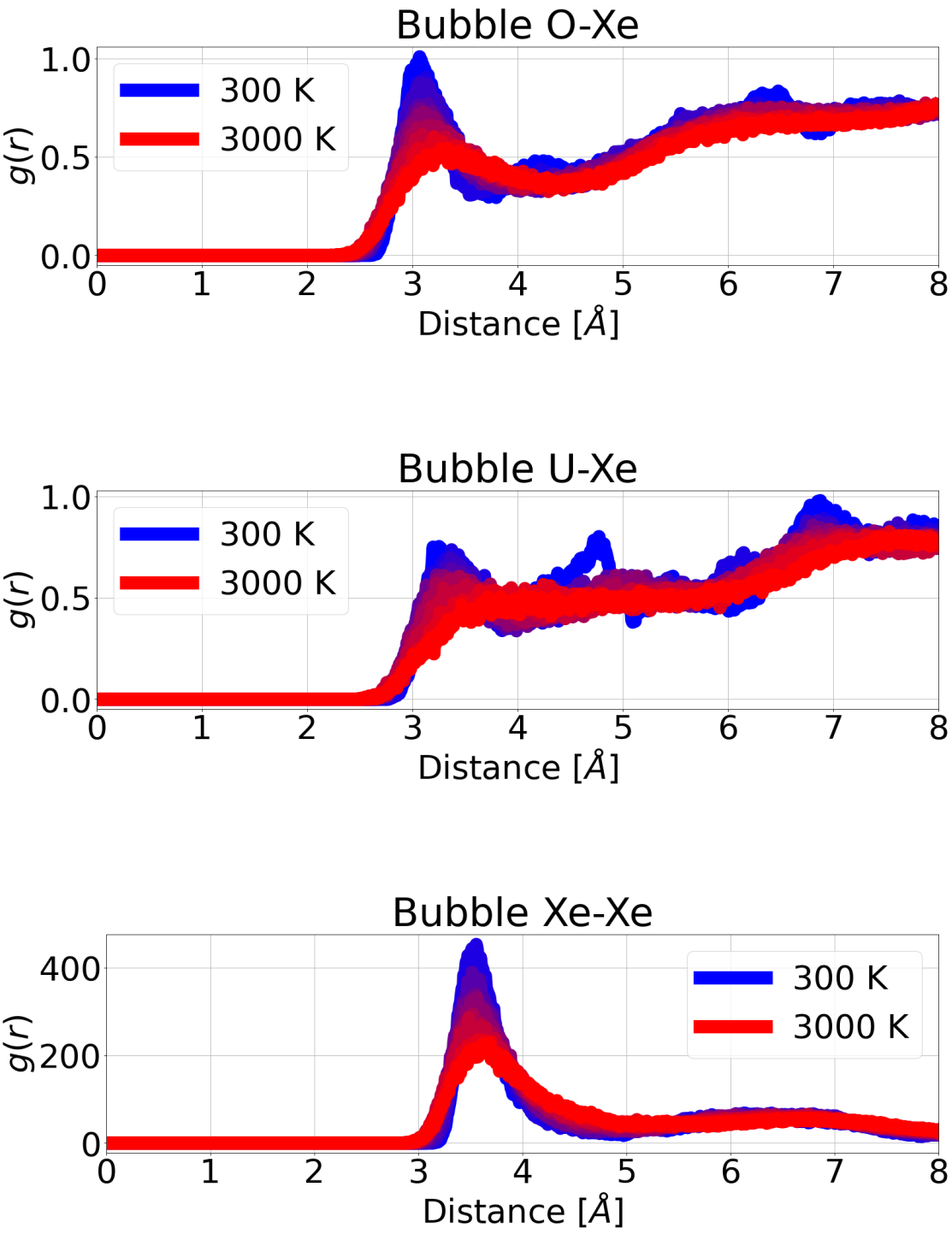

Figure 4.30: The radial distribution functions of a UO_2 structure with a cubic distribution of spherical bubbles of 25 Schottky defects and 30 xenon atoms each.

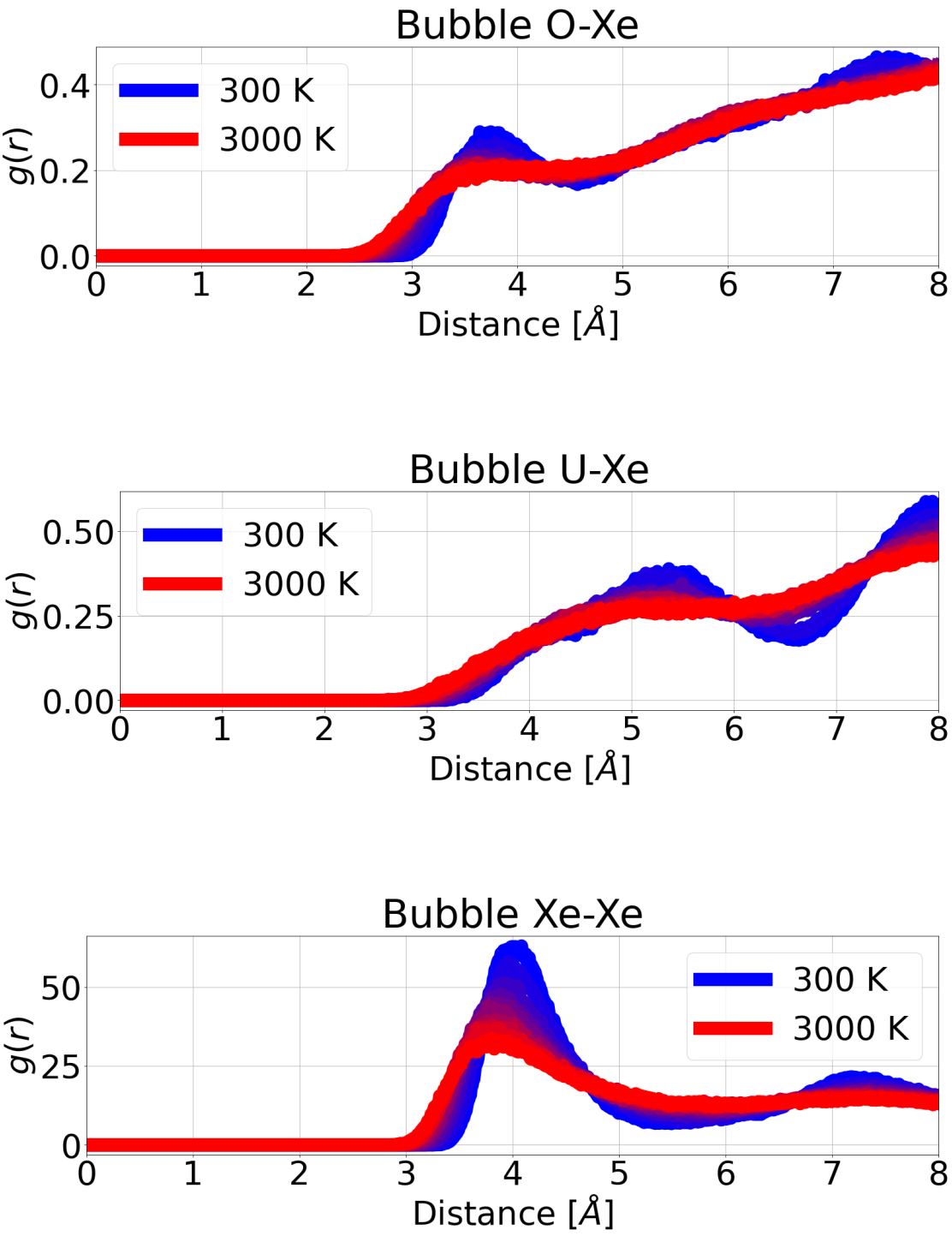

Figure 4.31: The radial distribution functions of a UO_2 structure with a cubic distribution of spherical bubbles of 200 Schottky defects and 240 xenon atoms each.

Chapter 5

Conclusions

In this work the analysis of the effect of xenon nano-bubbles on the physical properties of MOX fuels was investigated using atomistic simulations. The document provides a theoretical background in its initial part, to summarize the main insight found in the literature concerning MOX properties in general, xenon bubbles characteristics and existing experimental data.
The second part contains the methods, the algorithms and the assumptions of the models that were imposed, this should not be considered as an exhaustive explanation of the things done to obtain the results, but as a guideline. The results are then presented, including both the main physical properties that this work aimed to obtain (heat capacity, linear thermal expansion coefficient, elastic coefficients, thermal conductivity), and other properties of the materials useful to understand its behaviour, such as the lattice parameters.
The consequence of xenon presence in the fuel is to decrease all the properties investigated. The decrease is more important for higher porosities and the amount of xenon present seems to be of a second order importance, as it only slightly effects the properties. The Bredig transition is clearly visible in all the properties, either as a peak, like in the case of the specific heat, or as a change in the slope, like the case of the Young modulus. Three laws are proposed to take into account the effect of nano-bubbles porosity, one for the specific heat and the LTEC, one for the elastic coefficients and one for the thermal conductivity; all the laws have been fitted with the obtained simulation data and the resulting coefficients can be found in the results' chapter.
To complement the results of this work, it could be useful in the future to investigate the effect of nano-bubbles porosity using ab-initio methods or different MD potentials (machine learning potentials for MOXs are currently developed at the LM2C laboratory), to study bigger and differently shaped bubbles, to inspect a spacial configuration of the bubbles different from the simple cubic studied here, to examine more closely the effect of xenon pressure on the bubble's behaviour and to

consider non-stoichiometric conditions.
This work was completed at the CEA center of Cadarache, during an internship experience in the course of a double degree nuclear engineering master program between Politecnico di Torino and Grenoble INP - Phelma.

Bibliography

[1] World Resources Institute. 2020. URL: http://cait.wri.org/ (cit. on p. 1).

[2] IEA. *Nuclear Power and Secure Energy Transitions*. Paris, License: CC BY 4.0. 2022. URL: https://www.iea.org/reports/nuclear-power-and-secure-energy-transitions (cit. on p. 1).

[3] A. P. Thompson et al. «LAMMPS - a flexible simulation tool for particle-based materials modeling at the atomic, meso, and continuum scales». In: *Comp. Phys. Comm.* 271 (2022), p. 108171. DOI: 10.1016/j.cpc.2021.108171 (cit. on pp. 2, 27).

[4] Alexander Stukowski. «Visualization and analysis of atomistic simulation data with OVITO-the Open Visualization Tool». In: *MODELLING AND SIMULATION IN MATERIALS SCIENCE AND ENGINEERING* 18.1 (JAN 2010). ISSN: 0965-0393. DOI: {10.1088/0965-0393/18/1/015012} (cit. on p. 2).

[5] T.K. Engel. «The heat capacities of Al2o3, Uo2 and PuO2 From 300 To 1100 °K». In: *Journal of Nuclear Materials* 31.2 (1969), pp. 211–214. ISSN: 0022-3115. DOI: https://doi.org/10.1016/0022-3115(69)90194-9. URL: https://www.sciencedirect.com/science/article/pii/0022311569901949 (cit. on p. 5).

[6] Fredrik Grønvold, Nils Jørgen Kveseth, Arvid Sveen, and Jiři Tichý. «Thermodynamics of the UO2+x phase I. Heat capacities of UO2.017 and UO2.254 from 300 to 1000 K and electronic contributions». In: *The Journal of Chemical Thermodynamics* 2.5 (1970), pp. 665–679. ISSN: 0021-9614. DOI: https://doi.org/10.1016/0021-9614(70)90042-X. URL: https://www.sciencedirect.com/science/article/pii/002196147090042X (cit. on p. 5).

[7] A E Ogard and J A Leary. «HIGH-TEMPERATURE HEAT CONTENT AND HEAT CAPACITY OF URANIUM DIOXIDE AND URANIUM DIOXIDE–PLUTONIUM DIOXIDE SOLID SOLUTIONS.» In: *pp 651-65 of Thermodynamics of Nuclear Materials, 1967. Vienna, International Atomic Energy Agency, 1968.* (Oct. 1968). URL: https://www.osti.gov/biblio/4528215 (cit. on p. 5).

[8] J P Hiernaut, G J Hyland, and C RonchP. «Premelting transition in uranium dioxide». en. In: (1993), p. 25 (cit. on p. 5).

[9] T.R. Pavlov, M.R. Wenman, L. Vlahovic, D. Robba, R.J.M. Konings, P. Van Uffelen, and R.W. Grimes. «Measurement and interpretation of the thermo-physical properties of UO2 at high temperatures: The viral effect of oxygen defects». In: *Acta Materialia* 139 (2017), pp. 138–154. ISSN: 1359-6454. DOI: https://doi.org/10.1016/j.actamat.2017.07.060. URL: https://www.sciencedirect.com/science/article/pii/S1359645417306419 (cit. on p. 5).

[10] Jeffrey Ralph and G. J. Hyland. «Empirical confirmation of a bredig transition in UO2». In: *Journal of Nuclear Materials* 132 (1985), pp. 76–79. URL: https://api.semanticscholar.org/CorpusID:94294832 (cit. on p. 5).

[11] M T Hutchings, K Clausen, M H Dickens, W Hayes, J K Kjems, P G Schnabel, and C Smith. «Investigation of thermally induced anion disorder in fluorites using neutron scattering techniques». In: *Journal of Physics C: Solid State Physics* 17.22 (Aug. 1984), p. 3903. DOI: 10.1088/0022-3719/17/22/011. URL: https://dx.doi.org/10.1088/0022-3719/17/22/011 (cit. on p. 5).

[12] C. Ronchi and G.J. Hyland. «Analysis of recent measurements of the heat capacity of uranium dioxide». In: *Journal of Alloys and Compounds* 213-214 (1994). International Conference on Actinides, pp. 159–168. ISSN: 0925-8388. DOI: https://doi.org/10.1016/0925-8388(94)90897-4. URL: https://www.sciencedirect.com/science/article/pii/0925838894908974 (cit. on p. 5).

[13] Paul Browning, Gerard J. Hyland, and Jeffrey Ralph. «ORIGIN OF THE SPECIFIC HEAT ANOMALY IN SOLID URANIA.» In: *High Temperatures - High Pressures* 15.2 (1983). Cited by: 44, pp. 169–178. URL: https://www.scopus.com/inward/record.uri?eid=2-s2.0-0020901890&partnerID=40&md5=5cda516769741ad3076459f04926f1ca (cit. on pp. 5, 49).

[14] A. S. Dworkin and Max A. Bredig. «Diffuse transition and melting in fluorite and antifluorite type of compounds. Heat content of potassium sulfide from 298 to 1260.degree.K». In: *The Journal of Physical Chemistry* 72.4 (1968), pp. 1277–1281. DOI: 10.1021/j100850a035. eprint: https://doi.org/10.1021/j100850a035. URL: https://doi.org/10.1021/j100850a035 (cit. on pp. 5, 30, 68).

[15] Michael Cooper. «Atomic scale simulation of irradiated nuclear fuel». PhD thesis. Imperial College London, Apr. 2015. DOI: https://doi.org/10.25560/23808. URL: http://hdl.handle.net/10044/1/23808 (cit. on p. 5).

[16] Hao Zhang, Xinyi Wang, Alexandros Chremos, and Jack F. Douglas. «Superionic UO2: A model anharmonic crystalline material». In: *The Journal of Chemical Physics* 150.17 (May 2019), p. 174506. DOI: 10.1063/1.5091042. URL: https://doi.org/10.1063%2F1.5091042 (cit. on p. 5).

[17] Ajay Annamareddy and Jacob Eapen. «Low Dimensional String-like Relaxation Underpins Superionic Conduction in Fluorites and Related Structures». In: *Scientific Reports* 7.1 (Mar. 2017), p. 44149. ISSN: 2045-2322. DOI: 10.1038/srep44149. URL: https://doi.org/10.1038/srep44149 (cit. on p. 5).

[18] Angus Gray-Weale and Paul A. Madden. «Dynamical Arrest in Superionic Crystals and Supercooled Liquids». In: *The Journal of Physical Chemistry B* 108.21 (2004), pp. 6624–6633. DOI: 10.1021/jp037706a. eprint: https://doi.org/10.1021/jp037706a. URL: https://doi.org/10.1021/jp037706a (cit. on p. 5).

[19] Michael J Castiglione and Paul A Madden. «Fluoride ion disorder and clustering in superionic PbF2». In: *Journal of Physics: Condensed Matter* 13.44 (Oct. 2001), p. 9963. DOI: 10.1088/0953-8984/13/44/311. URL: https://dx.doi.org/10.1088/0953-8984/13/44/311 (cit. on p. 5).

[20] J.B. Boyce, J.C. Mikkelsen, and M. O'Keeffe. «Ion dynamics and sublattice melting in the superionic conductor PbF2». In: *Solid State Communications* 21.10 (1977), pp. 955–958. ISSN: 0038-1098. DOI: https://doi.org/10.1016/0038-1098(77)90898-5. URL: https://www.sciencedirect.com/science/article/pii/0038109877908985 (cit. on p. 5).

[21] Benjamin Dacus, Benjamin Beeler, and Daniel Schwen. «Calculation of threshold displacement energies in UO2». In: *Journal of Nuclear Materials* 520 (2019), pp. 152–164. DOI: 10.1016/j.jnucmat.2019.04.002. URL: https://www.sciencedirect.com/science/article/pii/S0022311518312571 (cit. on p. 6).

[22] Yasir Idrees. «MICROSTRUCTURAL EVOLUTION IN ZR AND ZR ALLOY EXCEL UNDER ION IRRADIATION». PhD thesis. Dec. 2013. DOI: 10.13140/RG.2.2.26459.46884 (cit. on p. 6).

[23] IAEA. *Cumulative Fission Yields*. Oct. 2006. URL: https://www-nds.iaea.org/sgnucdat/c3.htm (cit. on pp. 7, 8).

[24] F. Lemoine, O. Serot, P. Leconte, and D. Bernard. «The Isotopic Composition of Fission Gas Release from MOX and High Burnup UO2 Fuel to Check the Fission Yield Database». In: (Sept. 2014) (cit. on p. 7).

[25] M. Gerardin, E. Gilabert, D. Horlait, M-F. Barthe, and G. Carlot. «Experimental study of the diffusion of Xe and Kr implanted at low concentrations in UO2 and determination of their trapping mechanisms». In: *Journal of Nuclear Materials* 556 (2021), p. 153174. ISSN: 0022-3115. DOI: https://doi.org/10.1016/j.jnucmat.2021.153174. URL: https://www.sciencedirect.com/science/article/pii/S0022311521003974 (cit. on p. 7).

[26] Christopher Matthews, Romain Perriot, M.W.D Cooper, Christopher R. Stanek, and David A. Andersson. «Cluster dynamics simulation of xenon diffusion during irradiation in UO2». In: *Journal of Nuclear Materials* 540 (2020), p. 152326. ISSN: 0022-3115. DOI: https://doi.org/10.1016/j.jnucmat.2020.152326. URL: https://www.sciencedirect.com/science/article/pii/S0022311520301884 (cit. on p. 7).

[27] Michael Tonks et al. «Unit mechanisms of fission gas release: Current understanding and future needs». In: *Journal of Nuclear Materials* 504 (2018), pp. 300–317. ISSN: 0022-3115. DOI: https://doi.org/10.1016/j.jnucmat.2018.03.016 (cit. on pp. 7, 9–11).

[28] A.Woolsey. «An Investigation into the Present and Future Dose Rate of the United Kingdom's Radioactive Waste Inventory». In: (Oct. 2018). DOI: 10.13140/RG.2.2.20804.48000 (cit. on p. 9).

[29] I. Zacharie, S. Lansiart, P. Combette, M. Trotabas, M. Coster, and M. Groos. «Microstructural analysis and modelling of intergranular swelling of an irradiated UO2 fuel treated at high temperature». In: *Journal of Nuclear Materials* 255.2 (1998), pp. 92–104. ISSN: 0022-3115. DOI: https://doi.org/10.1016/S0022-3115(98)00040-3. URL: https://www.sciencedirect.com/science/article/pii/S0022311598000403 (cit. on p. 11).

[30] R. M. Cornell. «An electron microscope examination of matrix fission-gas bubbles in irradiated uranium dioxide». In: *Journal of Nuclear Materials* 38, no. 3 (Mar. 1971), pp. 319–328. DOI: 10.1016/0022-3115(71)90061-4 (cit. on pp. 11, 13–15).

[31] K. Nogita and K. Une. «Irradiation-induced recrystallization in high burnup UO2 fuel». In: *Journal of Nuclear Materials* 226, no. 3 (1995), pp. 302–310. DOI: 10.1016/0022-3115(95)00123-9 (cit. on pp. 11, 14–16).

[32] K. Nogita and K. Une. «High resolution TEM observation and density estimation of Xe bubbles in high burnup UO2 fuels». In: *Nuclear Instruments and Methods in Physics Research Section B: Beam Interactions with Materials and Atoms* 141, no. 1 (May 1998), pp. 481–486. DOI: 10.1016/S0168-583X(98)00040-8 (cit. on pp. 11, 14, 15).

[33] S. Kashibe, K. Une, and K. Nogita. «Formation and growth of intragranular fission gas bubbles in UO2 fuels with burnup of 6-83 GWd/t». In: *Journal of Nuclear Materials* 206, no. 1 (Nov. 1993), pp. 22–34. DOI: 10.1016/0022-3115(93)90229-R (cit. on pp. 11, 14, 15).

[34] J. H. Evans, A. van Veen, and K. T. Westerduin. «A TEM and TDS study of gas release from bubbles in krypton-implanted uranium dioxide». In: *Journal of Nuclear Materials* 195, no. 3 (Nov. 1992), pp. 250–259. DOI: 10.1016/0022-3115(92)90516-N (cit. on p. 12).

[35] P. Martin et al. «XAS characterisation of xenon bubbles in uranium dioxide». In: *Nuclear Instruments and Methods in Physics Research Section B: Beam Interactions with Materials and Atoms* 266, no. 12 (June 2008), pp. 2887–2891. DOI: 10.1016/j.nimb.2008.03.180 (cit. on pp. 12, 18).

[36] P. Garcia et al. «A study of xenon aggregates in uranium dioxide using X-ray absorption spectroscopy». In: *Journal of Nuclear Materials* 352, no. 1 (June 2006), pp. 136–143. DOI: 10.1016/j.jnucmat.2006.02.047 (cit. on pp. 12, 18).

[37] C. Sabathier et al. «In situ TEM study of temperature-induced fission product precipitation in UO2». In: *Nuclear Instruments and Methods in Physics Research Section B: Beam Interactions with Materials and Atoms* 266, no. 12 (June 2008), pp. 3027–3032. DOI: 10.1016/j.nimb.2008.03.158 (cit. on p. 12).

[38] B. Ye et al. «TEM investigation of irradiation damage in single crystal CeO2». In: *Journal of Nuclear Materials* 414, no. 2 (July 2011), pp. 251–256. DOI: 10.1016/j.jnucmat.2011.03.052 (cit. on p. 12).

[39] M. H. Wood. «An analysis of observations of fission gas bubble distributions in fuel». In: *Journal of Nuclear Materials* 82, no. 2 (July 1979), pp. 257–263. DOI: 10.1016/0022-3115(79)90008-4 (cit. on pp. 12, 16).

[40] P. V. Nerikar, D. C. Parfitt, L. A. Casillas Trujillo, D. A. Andersson, C. Unal, S. B. Sinnott, R. W. Grimes, B. P. Uberuaga, and C. R. Stanek. «Segregation of xenon to dislocations and grain boundaries in uranium dioxide». In: *Phys. Rev. B* 84 (17 Nov. 2011), p. 174105. DOI: 10.1103/PhysRevB.84.174105. URL: https://link.aps.org/doi/10.1103/PhysRevB.84.174105 (cit. on p. 12).

[41] David A. Andersson, Michael R. Tonks, Luis Casillas, Shyam Vyas, Pankaj Nerikar, Blas P. Uberuaga, and Christopher R. Stanek. «Multiscale simulation of xenon diffusion and grain boundary segregation in UO2». In: *Journal of Nuclear Materials* 462 (2015), pp. 15–25. ISSN: 0022-3115. DOI: https://doi.org/10.1016/j.jnucmat.2015.03.019. URL: https://www.

sciencedirect.com/science/article/pii/S0022311515001658 (cit. on p. 12).

[42] C. O. T. Galvin, M. J. D. Rushton, M. W. D. Cooper, D. A. Andersson, P. A. Burr, and R. W. Grimes. «The predicted shapes of voids and Xe bubbles in UO2». In: *Journal of Nuclear Materials* 543 (Jan. 2021), p. 152622. DOI: 10.1016/j.jnucmat.2020.152622 (cit. on pp. 13, 15).

[43] L. Yang and B.D. Wirth. «Evolution of pressurized xenon bubble and response of uranium dioxide matrix: A molecular dynamics study». In: *Journal of Nuclear Materials* 544 (2021), p. 152730. ISSN: 0022-3115. DOI: https://doi.org/10.1016/j.jnucmat.2020.152730. URL: https://www.sciencedirect.com/science/article/pii/S0022311520313386 (cit. on pp. 18, 29).

[44] L. Yang and B.D. Wirth. «An improved xenon equation of state for nanobubbles in UO2». In: *Journal of Nuclear Materials* 572 (2022). DOI: 10.1016/j.jnucmat.2022.154089 (cit. on p. 18).

[45] A. Shadrin, Yu. Mochalov, K. Dvoeglazov, and V. Kascheev. «Reprocessing of Fast Reactors Mixed U-Pu Used Nuclear Fuel in Russian Federation: Studies and Industrial Test». In: *International Conference on Fast Reactors and Related Fuel Cycles: Next Generation Nuclear Systems for Sustainable Development (FR17)* (2017). URL: https://inis.iaea.org/search/search.aspx?orig_q=RN:49085705 (cit. on p. 19).

[46] M. Tiphine, C. Coquelet, R. Girieud, R. Eschbach, C. Chabert-Koralews, and R. Grosman. «Sodium Fast Reactor: an Asset for a PWR UOX/MOX Fleet». In: *GLOBAL 2015 - 21st International Conference and Exhibition " Nuclear Fuel Cycle for a Low-Carbon Future"*. Vol. Global 2015 proceedings. Paris, France, Sept. 2015. URL: https://hal-cea.archives-ouvertes.fr/cea-02509683 (cit. on p. 19).

[47] D. Bathellier, M. Lainet, M. Freyss, P. Olsson, and E. Bourasseau. «A new heat capacity law for UO2, PuO2 and (U,Pu)O2 derived from molecular dynamics simulations and useable in fuel performance codes». In: *Journal of Nuclear Materials* 549 (2021). DOI: 10.1016/j.jnucmat.2021.152877 (cit. on pp. 19, 34, 42, 48, 49).

[48] Charles Kittel. «Introduction to Solid State Physics». In: *Wiley series on the science and technology of materials* (1953) (cit. on pp. 24, 25).

[49] M. W. D. Cooper, M. J. D. Rushton, and R. W. Grimes. «A many-body potential approach to modelling the thermomechanical properties of actinide oxides». In: *Journal of Physics: Condensed Matter* 26 (10 2014). DOI: 10.1088/0953-8984/26/10/105401 (cit. on pp. 26, 69).

[50] M. W. D. Cooper, N. Kuganathan, P. A. Burr M. J. D. Rushton, R. W. Grimes, C. R. Stanek, and D. A. Andersson. «Development of Xe and Kr empirical potentials for CeO2 , ThO2 , UO2 and PuO2 , combining DFT with high temperature MDs». In: *Journal of Physics: Condensed Matter* 28 (40 2016). DOI: 10.1088/0953-8984/28/40/405401 (cit. on p. 26).

[51] Pascal Viot. «Simulation numérique en physique statistique». DEA. Lecture. Sept. 2006. URL: https://cel.hal.science/cel-00092945 (cit. on p. 27).

[52] G. Ciccotti, M. Ferrario, and C. Schuette. *Molecular Dynamics Simulation*. MDPI AG, 2018. ISBN: 9783906980652. URL: https://books.google.fr/books?id=RodxDwAAQBAJ (cit. on p. 27).

[53] William G. Hoover. «Canonical dynamics: Equilibrium phase-space distributions». In: *Phys. Rev. A* 31 (3 Mar. 1985), pp. 1695–1697. DOI: 10.1103/PhysRevA.31.1695. URL: https://link.aps.org/doi/10.1103/PhysRevA.31.1695 (cit. on p. 27).

[54] Glenn J. Martyna, Douglas J. Tobias, and Michael L. Klein. «Constant pressure molecular dynamics algorithms». In: *The Journal of Chemical Physics* 101.5 (Sept. 1994), pp. 4177–4189. ISSN: 0021-9606. DOI: 10.1063/1.467468. URL: https://doi.org/10.1063/1.467468 (cit. on p. 28).

[55] Xueyan Zhu, Hengfeng Gong, Ya-Fan Zhao, De-Ye Lin, Guomin Han, Tong Liu, and Haifeng Song. «Effect of Xe bubbles on the thermal conductivity of UO2: Mechanisms and model establishment». In: *Journal of Nuclear Materials* 533 (2020), p. 152080. ISSN: 0022-3115. DOI: https://doi.org/10.1016/j.jnucmat.2020.152080. URL: https://www.sciencedirect.com/science/article/pii/S0022311519312863 (cit. on pp. 29, 64).

[56] R Hill. «The Elastic Behaviour of a Crystalline Aggregate». In: *Proceedings of the Physical Society. Section A* 65.5 (May 1952), p. 349. DOI: 10.1088/0370-1298/65/5/307. URL: https://dx.doi.org/10.1088/0370-1298/65/5/307 (cit. on p. 37).

[57] Kazuhiro Yamada, Ken Kurosaki, Msayoshi Uno, and Shinsuke Yamanaka. «Evaluation of thermal properties of uranium dioxide by molecular dynamics». In: *Journal of Alloys and Compounds* 307.1 (2000), pp. 10–16. ISSN: 0925-8388. DOI: https://doi.org/10.1016/S0925-8388(00)00806-9. URL: https://www.sciencedirect.com/science/article/pii/S0925838800008069 (cit. on p. 38).

[58] Tatsumi Arima, Sho Yamasaki, Kazuya Idemitsu, and Yaohiro Inagaki. «Equilibrium and nonequilibrium molecular dynamics simulations of heat conduction in uranium oxide and mixed uranium-plutonium oxide». In: *Journal of Nuclear Materials* 376.2 (2008), pp. 139–145. ISSN: 0022-3115. DOI: https://doi.org/10.1016/j.jnucmat.2008.02.067. URL: https:

//www.sciencedirect.com/science/article/pii/S0022311508001608 (cit. on p. 38).

[59] Jackson R. Harter, Laura de Sousa Oliveira, Agnieszka Truszkowska, Todd S. Palmer, and P. Alex Greaney. «Deterministic Phonon Transport Predictions of Thermal Conductivity in Uranium Dioxide With Xenon Impurities». In: *Journal of Heat Transfer* 140.5 (Jan. 2018), p. 051301. ISSN: 0022-1481. DOI: 10.1115/1.4038554. eprint: https://asmedigitalcollection.asme.org/heattransfer/article-pdf/140/5/051301/6372736/ht_140_05_051301.pdf. URL: https://doi.org/10.1115/1.4038554 (cit. on p. 38).

[60] Florian Müller-Plathe and Patrice Bordat. «Reverse Non-equilibrium Molecular Dynamics». In: *Novel Methods in Soft Matter Simulations*. Ed. by Mikko Karttunen, Ari Lukkarinen, and Ilpo Vattulainen. Berlin, Heidelberg: Springer Berlin Heidelberg, 2004, pp. 310–326. ISBN: 978-3-540-39895-0. DOI: 10.1007/978-3-540-39895-0_10. URL: https://doi.org/10.1007/978-3-540-39895-0_10 (cit. on pp. 38, 39, 65).

[61] B Dongre, T Wang, and G K H Madsen. «Comparison of the Green-Kubo and homogeneous non-equilibrium molecular dynamics methods for calculating thermal conductivity». In: *Modelling and Simulation in Materials Science and Engineering* 25.5 (May 2017), p. 054001. DOI: 10.1088/1361-651X/aa6f57. URL: https://dx.doi.org/10.1088/1361-651X/aa6f57 (cit. on p. 38).

[62] M. Kato and T. Matsumoto. *Thermal and Mechanical Properties of UO_2 and PuO_2*. Tech. rep. NUCLEAR FUEL CYCLE AND FUEL MATERIALS. Nuclear Energy Agency of the OECD (NEA), 2015, pp. 172–177. URL: http://inis.iaea.org/search/search.aspx?orig_q=RN:47093736 (cit. on p. 40).

[63] J.K. Fink. «Thermophysical properties of uranium dioxide». In: *Journal of Nuclear Materials* 279.1 (2000), pp. 1–18. ISSN: 0022-3115. DOI: https://doi.org/10.1016/S0022-3115(99)00273-1. URL: https://www.sciencedirect.com/science/article/pii/S0022311599002731 (cit. on pp. 40, 41).

[64] M.W.D. Cooper, R.W. Grimes, M.E. Fitzpatrick, and A. Chroneos. «Modeling oxygen self-diffusion in UO2 under pressure». In: *Solid State Ionics* 282 (2015), pp. 26–30. ISSN: 0167-2738. DOI: https://doi.org/10.1016/j.ssi.2015.09.006. URL: https://www.sciencedirect.com/science/article/pii/S016727381500346X (cit. on p. 44).

[65] M.W.D. Cooper, S.C. Middleburgh, and R.W. Grimes. «Modelling the thermal conductivity of (UxTh1-x)O2 and (UxPu1-x)O2». In: *Journal of Nuclear Materials* 466 (2015), pp. 29–35. ISSN: 0022-3115. DOI: https://doi.org/10.

1016/j.jnucmat.2015.07.022. URL: https://www.sciencedirect.com/science/article/pii/S0022311515301082 (cit. on pp. 64, 65).

[66] Christopher I. Maxwell and Jeremy Pencer. «Molecular dynamics modelling of the thermal conductivity of off-stoichiometric UO2±x and (UyPu1-y)O2±x using equilibrium molecular dynamics». In: *Annals of Nuclear Energy* 131 (2019), pp. 317–324. ISSN: 0306-4549. DOI: https://doi.org/10.1016/j.anucene.2019.03.029. URL: https://www.sciencedirect.com/science/article/pii/S0306454919301616 (cit. on pp. 64, 65).

[67] Kyoichi Morimoto, Masato Kato, Masahiro Ogasawara, Motoaki Kashimura, and Tomoyuki Abe. «Thermal conductivities of (U, Pu, Am)O2 solid solutions». In: *Journal of Alloys and Compounds* 452.1 (2008). Proceedings of the 12th International IUPAC Conference on High Temperature Materials Chemistry-HTMC XII, pp. 54–60. ISSN: 0925-8388. DOI: https://doi.org/10.1016/j.jallcom.2006.12.159. URL: https://www.sciencedirect.com/science/article/pii/S092583880700446X (cit. on p. 64).

[68] Judy W. L. Pang, William J. L. Buyers, Aleksandr Chernatynskiy, Mark D. Lumsden, Bennett C. Larson, and Simon R. Phillpot. «Phonon Lifetime Investigation of Anharmonicity and Thermal Conductivity of UO_2 by Neutron Scattering and Theory». In: *Phys. Rev. Lett.* 110 (15 Apr. 2013), p. 157401. DOI: 10.1103/PhysRevLett.110.157401. URL: https://link.aps.org/doi/10.1103/PhysRevLett.110.157401 (cit. on p. 64).

[69] C. Cozzo, D. Staicu, J. Somers, A. Fernandez, and R.J.M. Konings. «Thermal diffusivity and conductivity of thorium-plutonium mixed oxides». In: *Journal of Nuclear Materials* 416.1 (2011). Nuclear Materials IV, pp. 135–141. ISSN: 0022-3115. DOI: https://doi.org/10.1016/j.jnucmat.2011.01.109. URL: https://www.sciencedirect.com/science/article/pii/S0022311511001577 (cit. on p. 64).

[70] Taku Matsumoto, Tatsumi Arima, Yaohiro Inagaki, Kazuya Idemitsu, Masato Kato, and Teppei Uchida. «Investigation of O/M ratio effect on thermal conductivity of oxide nuclear fuels by non-equilibrium molecular dynamics calculation». In: *Journal of Nuclear Materials* 440.1 (2013), pp. 580–585. ISSN: 0022-3115. DOI: https://doi.org/10.1016/j.jnucmat.2013.04.019. URL: https://www.sciencedirect.com/science/article/pii/S0022311513006193 (cit. on p. 64).

[71] S. Nichenko and D. Staicu. «Thermal conductivity of porous UO2: Molecular Dynamics study». In: *Journal of Nuclear Materials* 454.1 (2014), pp. 315–322. ISSN: 0022-3115. DOI: https://doi.org/10.1016/j.jnucmat.2014.08.009. URL: https://www.sciencedirect.com/science/article/pii/S0022311514005261 (cit. on p. 64).

[72] Masaki Amaya, Jinichi Nakamura, Fumihisa Nagase, and Toyoshi Fuketa. «Thermal conductivity evaluation of high burnup mixed-oxide (MOX) fuel pellet». In: *Journal of Nuclear Materials* 414.2 (2011), pp. 303–308. ISSN: 0022-3115. DOI: https://doi.org/10.1016/j.jnucmat.2011.04.020. URL: https://www.sciencedirect.com/science/article/pii/S0022311511003710 (cit. on p. 65).

[73] M.W.D. Cooper, S.T. Murphy, M.J.D. Rushton, and R.W. Grimes. «Thermophysical properties and oxygen transport in the (Ux,Pu1x)O2 lattice». In: *Journal of Nuclear Materials* 461 (2015), pp. 206–214. ISSN: 0022-3115. URL: https://doi.org/10.1016/j.jnucmat.2015.03.024 (cit. on p. 69).

[74] David A. Keen. «A comparison of various commonly used correlation functions for describing total scattering». In: *Journal of Applied Crystallography* 34.2 (Apr. 2001), pp. 172–177. DOI: 10.1107/S0021889800019993. URL: https://doi.org/10.1107/S0021889800019993 (cit. on p. 71).

Acronyms

CRG
Cooper-Rushton-Grimes

DFT
density functional theory

FGP
fission gas product

FGR
fission gas release

FNR
fast neutron reactor

HBS
high burn-up structure

HPC
high-performance computing

LAMMPS
Large-scale Atomic/Molecular Massively Parallel Simulator

LJ
Lennard-Jones

LTEC
linear thermal expansion coefficient

LWR

light water reactor

MD

molecular dynamic

MOX

mixed oxide

P3M

particle–particle-particle–mesh

RDF

radial distribution function

rNEMD

reverse non-equilibrium molecular dynamics

SD

Schottky defect

sko

single knock-on

TEC

thermal expansion coefficient

OVITO

Open Visualisation Tool